Manipulation of Proteins, Cells, & Endoscopy Optics with Piezoelectric Devices

A Dissertation

Presented to the Faculty of the Graduate School

of Cornell University

In Partial Fulfillment of the Requirements for the Degree of

Doctor of Philosophy

by

Grant David Meyer

May 2008

Manipulation of Proteins, Cells, & Endoscopy Optics with Piezoelectric Devices

Grant David Meyer, Ph.D.

Cornell University 2008

Piezoelectric devices convert electrical energy into mechanical energy yielding static deflection or oscillatory motion. With quartz crystal resonators, surface acoustic wave devices, and lead zirconate titanate actuators, proteins, cells, and endoscope optics were manipulated. Chapters two through five detail accelerated protein and cell release from planar substrates with quartz crystal resonators and surface acoustic wave devices. Targeted applications include immunoassays, cell separation, and cell membrane permeation. Results demonstrate acoustic wave dissipation into the fluid resting upon the oscillating surface accelerated nonspecific binding removal, while minimally removing bound antigen from antibodies, a common immunoassay challenge. An optimal difference in specific *vs.* nonspecific protein release rates was found at 100 mW using 5 MHz quartz crystal resonators. Because surface acoustic wave devices produce higher peak fluid velocities, approximately 10-fold relative to quartz crystal resonators, nonspecific protein and cell release experiments were extended to surface acoustic wave devices. Surface acoustic wave induced protein desorption, nonspecific cell release, and spatially dependent cell membrane permeation results are presented. In chapter six we detail a miniature two-dimensional fiber optic scanner design, fabrication, and fiber characterization methods for a real-time *in vivo* multi-photon endoscope.

BIOGRAPHICAL SKETCH

Family, friends, and fine professors have all contributed to Grant's current state. It is with warmest regards and sincere gratitude that he thanks each group for their time, thoughts, opinions, patience, and intellectual contributions.

He is particularly thankful to have had parents, Richard and Debbie who required dedication to academics, yet encouraged participation in, and attended, myriad sporting events, ranging from baseball to racquetball. He truly benefited from this balanced approach. Raised with "in-house" tutors possessing satellite and medical research expertise, it is no surprise his interests reside at the physical/biological interface.

His sisters, Lindsay and Lauren, taught him much about the other half of society, of which, admittedly, he has primitive understanding. Having narrowly escaped his early, unrefined club swinging years, each can attest to his failure to progress from barbaric beginnings.

Raised in the shadow of the Atomic Age, surrounded by academic excellence diffusing from nuclear power, he was exposed to many physicists, chemists, and mathematicians. Notable individuals include Professors James Brozik and Robert Duncan who are extraordinary role models and fine men.

Influenced by this environment, Grant pursued physics, chemistry, and pure mathematics at the University of New Mexico. He then traveled east to pursue biosensor and molecular diagnostics R&D with alacrity. In the East he was influenced by the many notable individuals listed in the Acknowledgment section.

ACKNOWLEDGMENT

Professor Harold Craighead most significantly influenced this work. His analytical rigor and quest for meaningful results are core values often uttered, but rarely found.

Professors Barbara Baird and Mike Shuler both provided constructive encouragement, which caused me to pursue a better understanding of proteins at the molecular level and better quantitative methods.

Chris Schaffer, Larry Walker, & Dr. Shivaun Archer each provided opportunities for growth and much needed constructive re-direction. Each has significantly contributed to solid students.

The nocturnal Rob Ilic was an interesting clean-room tutor and extraordinary character. His inexhaustible energy and extensive fabrication knowledge are rare assets.

Numerous lab members fielded myriad questions, which contributed to a better of understanding of my experiments. I thank you all for your time and help.

Working with the Professors Watt Webb, Chris Xu, and Dr. Hyungsik Lim to develop a real-time *in vivo* tissue imaging endoscope was a particularly rewarding conclusion to my time at Cornell. I thank each of you for the opportunity to pursue this novel surgical device. Future patients and taxpayers will undoubtedly benefit from your hard work.

Behind the scenes there were many individuals coordinating meetings, re-orienting confused graduate students, and diligently ensuring system components engage. I am thankful to Lorraine Capogrossi, Vicki Dann, and Mark Williams for their support.

John Jaquette always pushed me to differentiate my skills. His keen grasp of reality and social awareness are remarkable.

Gene Fitzgerald, Abe Stroock, & Andreas Wankerl were strong sources of

positivity and indomitable spirits. I thank each of you for your unrelenting optimism genuine dedication to the innovation process.

Professor McAdams, my favorite irascible economics professor, significantly improved my ability to understand the “big” picture. His ability to keep his eye on the ball is remarkable.

John Mannion, Andrew Chadeayne, Andrew Holmberg, Dave Manke, Bryan Ricchetti, Daniel Freedman, Mike Goulet, José Morán-Mirabal, Don Aubrecht, Felix Zamora, Peter Merkx & the Men of Mystery were boundless sources of energy, creativity, and interesting conversation—a truly unique cast of characters.

CONTENTS

CHAPTER ONE

Introduction

I. GENERAL DISSERTATION OVERVIEW

This work concerns two distinct applications: (1) Acoustic wave devices employed in *ex vivo* bioassay (lab chip) applications, and (2) A two-dimensional raster scanning piezoelectric device designed to integrate a single mode optical fiber into an endoscope probe for *in vivo* multiphoton microscopy. Chapters two through five address application one, and chapter six addresses application two.

II. QUARTZ CRYSTSAL RESONATORS & SURFACE ACOUSTIC WAVE DEVICES

Quartz crystal resonators and surface acoustic waves driven at milliwatt power levels dissipate mechanical energy into fluid confined near the oscillating surface. Oscillations impart kinetic energy to the fluid and biological constituents present in the sample volume. Chapters two through five present results detailing acoustic wave induced protein desorption, the fluid mechanics near the surface, nonspecifically bound cell release, and cell membrane permeation.

Initial experiments targeted protein microarrays because the success of this technology hinges upon a strong signal relative to background. Protein microarrays are high information density bioassays that, if accurate, provide information valuable in early disease diagnosis. While elegant patterning methods exist, diagnostic validity is crippled by nonspecific binding and device fouling. Nonspecifically bound biomolecules create false signal, block sensor receptors, and foul detectors. As

biomarker detection (electrochemical, gravimetric or optical) is pushed to lower levels, nonspecific binding becomes increasingly problematic.

Commonly, nonspecific binding is mitigated by surfactant addition or extensive washing. Additional steps and chemicals add complexity to devices promised to be portable, robust, simple and accurate. Using quartz crystal resonators and surface acoustic wave devices, low affinity proteins and cells were removed from protein microarrays, improving protein spot uniformity, signal reproducibility, and signal-to-background levels.

While potentially powerful, protein microarrays (i.e. multiplexed immunoassays) often yield false positives and negatives, a significant barrier to broad research and clinical implementation [1]. Nonspecific binding creates false positives/negatives and limits sensitivity and specificity. Low sensitivity can make biomarkers undetectable at physiologic concentrations, but more importantly, poor specificity can lead to false signal. Blocking non-sensing control areas is routine, but frustratingly, crucial sensing areas cannot be blocked. Strict standards for diagnostic repeatability, reproducibility, and validity require that nonspecific binding be limited.

We demonstrate nonspecific binding removal from protein microarrays with quartz crystal resonators (QCR) in chapters two and three, nonspecifically bound protein removal from a microchannel in chapter four, and nonspecifically bound cell removal with surface acoustic wave devices (SAW) in chapter five. QCR and SAW devices, routinely employed as gravimetric transducers in chemical and biological sensing, were used to remove nonspecifically bound protein and cells by driving resonators at power levels above typical sensing RF-input powers. We hypothesized, as did Nyborg in 1958, that shear stress “should be significant in continuous removal of loosely adhering surface layers” [2]. The data presented in chapters two through five confirm and chronicle results arising from this statement.

III. COMPARING QUARTZ CRYSTAL RESONATORS & SURFACE ACOUSTIC WAVE DEVICES

A quartz crystal resonator (QCR) and surface acoustic wave (SAW) device are pictured in *Figure 1*. The QCR operates at 5 MHz, while the SAW operates at 100 MHz. Results indicate SAW devices generate acoustic velocities approximately 10-fold larger than QCR devices (2 mm/s (QCR) *vs.* 2 cm/s (SAW)) at a given input power. The lower quartz crystal velocity arises from the gold electrode evaporated upon the quartz and lower operating frequency.

In addition to higher fluid velocities, SAW devices can be individually patterned to localize and excite specific chip areas (i.e. acoustic wave energy input can be directional and localized). Further, proper device placement and SAW design yield active areas with both mixing and sensing capabilities.

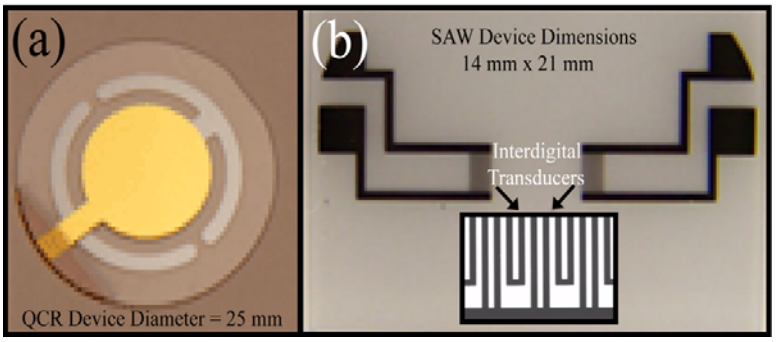

Figure 1.1. (a) Quartz crystal resonator photograph. (b) Surface acoustic wave device photographs (interdigital transducers are depicted in the inset).

IV. MULTIPHOTON MICROSCOPY FOR MEDICAL ENDOSCOPY: A TWO-DIMENSIONAL PIEZOELECTRIC RASTER SCANNER

Localized tissue excitation and the resulting localized photon emission make multi-photon microscopy well-suited for biomedical imaging. Extending multiphoton microscopy into the medical clinic requires femtosecond pulse delivery *in vivo*. Often interesting tissue lies in areas difficult to image (e.g. intestines, bladders, colons, and

other cavities). Hence, a small endoscope probe meeting surgical demands is imperative.

In addition to size and maneuverability constraints, single mode fiber optic cables delivering femtosecond pulses to the tissue must be scanned to obtain an acceptable field-of-view large enough to image hundreds of cells.

To this end, integrating multiphoton microscopy into existing clinical endoscope form factors, a two-dimensional piezoelectric raster scanner was designed, fabricated and tested to determine *x*, *y* fiber deflection values. Suggested design modifications are listed in the conclusion.

REFERENCES

[1] M. May, “A Quest for Specificity with Antibody Microarrays”, Genomics & Proteomics, Mar 2004, vol. 4 no. 2, 39-42.

[2] W. Nyborg, “Acoustic Streaming”, Physical Acoustics, vol II - part B, Ed. Mason: Academic Press, 1965, 265-331.

CHAPTER TWO

Nonspecific Binding Removal from Protein Microarrays Using Thickness Shear Mode Resonators

Grant D. Meyer, José M. Morán-Mirabal, Darren W. Branch, and Harold G. Craighead, *Member, IEEE*

ABSTRACT

Nonspecific binding is a universal problem that reduces bioassay sensitivity and specificity. We demonstrate that ultrasonic waves, generated by 5-MHz quartz crystal resonators, accelerate nonspecifically bound protein desorption from sensing and non-sensing areas of micropatterned protein arrays, controllably and nondestructively cleaning the micropatterns. Non-sensing area fluorescent intensity values dropped by more than 85% and sensing area fluorescent intensity dropped 77% due to nonspecific binding removal at an input power of 14W. After patterning, antibody films were many layers thick with nonspecifically bound protein, and protein aggregates obscured patterns. Quartz crystal resonators removed excess antibody layers and aggregates leaving highly uniform films, as evidenced by smaller spatial variations in fluorescent intensity and atomic force microscope surface roughness values. Fluorescent intensity values obtained after 14-W QCR operation were more repeatable and uniform.

Index Terms—Nonspecific binding, protein microarray, quartz crystal resonator, ultrasonic.

I. INTRODUCTION

Nonspecific binding decreases bioassay sensitivity, specificity, and reproducibility, which limit optical, electrochemical, and gravimetric biosensors, and can alter statistical analyses performed on microarrays [1], [2]. While appropriate surface chemistry may reduce nonspecific binding on non-sensing areas, this chemistry cannot be applied to sensing areas where specific binding occurs. These areas can nonspecifically bind solution components leading to inflated, falsely positive signal. Alternatively, nonspecific binding to non-sensing control areas reduces sensitivity, leading to false negatives.

Antibody aggregates also create experimental difficulties in microarray processing. Producing aggregation resistant antibodies may reduce aggregate formation [3], but requires additional time and cost. Nondestructive nonspecific binding removal improves data quality, simplifies analysis, and increases assay fidelity.

Quartz crystal resonators (QCRs) are commercially available and commonly used in the microelectronics industry. Routinely, resonators have been used as ultra-sensitive mass detectors, and are typically referred to as quartz crystal microbalances [4]. We demonstrate the ability of compact, reliable quartz crystal resonators to remove nonspecific binding, and improve fluorescent biosensor signal accuracy.

To create model micropatterned surfaces having both specifically and nonspecifically bound protein, QCRs were coated with parylene-C, photolithographically patterned, and etched [5]. Protein G was then covalently linked to lithographically defined gold areas, and parylene-C was removed, leaving patterned protein G squares. Patterned protein G squares measuring 20 x 20 μm defined sensing

areas. The surrounding area defined the non-sensing control area [see Figure 1(a)]. Fluorescently tagged antibody (IgG goat anti-mouse) and antigen (IgG mouse anti-rabbit) were added in succession to yield the model system. Experiments were carried out to test the hypothesis that shear stress could selectively remove nonspecifically bound protein G and immunoglobulins, while maintaining specifically bound antibody activity.

Shear wave penetration generates mechanical stress on proteins to reduce the activation energy of desorption, which expedites nonspecifically bound protein removal. To calculate the wave penetration decay length, the following equation was used

$$\delta = \left(\frac{\eta_L}{\pi f_0 \rho_L} \right)^{1/2}$$

where η_L is the fluid viscosity, ρ_L is the fluid density, and f_0 is the fundamental frequency [4]. For a 5-MHz resonator operated in buffer, δ = 250 nm. In the model covalent linking system used, the Stokes' radius for protein G is 3 nm, 5.5 nm for an IgG, and the covalent thiol linker is 1 nm long. The film thickness for a system with covalently bound protein G, antibody, and antigen should be about 29 nm [6], well within one decay length. Hence, the entire protein system becomes entrained, and a similar shear stress is present throughout the multilayer system.

II. EXPERIMENTAL

A. Parylene-C Micropatterning

QCRs operating at 5 MHz were purchased from Maxtek, Inc. Resonators were washed with acetone, isopropanol, and dried under nitrogen. Polyethylene oxide (0.1% by weight dilution in DI water, 900 000 MW, Sigma) was spun on devices prior to Parylene-C deposition at 2000 rpm (Laurell Technologies, WS-400A spinner).

Parylene-C was deposited to a thickness of 1.5 μm +/- 0.1 μm (SCS-Cookson). Positive tone Shipley photoresist (1827) was spun over the parylene-C film at 2000 rpm, and soft baked at 90 °C for 60 s. A contact mask with 20 μm squares was used to define features in the photoresist. AZ 300 MIF developer defined squares, which were then etched in an oxygen plasma. Care was taken to ensure all parylene in etched regions was removed, but little gold was sputtered. After micropatterning, photoresist was removed using acetone, isopropanol, and dried under nitrogen.

B. Surface Modification and Biological Tethering

Dithiobis[succinimidylpropionate] (DSP—Pierce Biotechnology, Inc.) was used to covalently link amines of protein G to open gold areas. Instructions were followed according to manufacturer specification with a 5-min sonication step and 20-s centrifugation at 2000 rpm being the only additions to the protocol. The sonication step was added to ensure maximum solvation. The centrifugation step was included to precipitate undissolved DSP. Only the supernatant was used in device preparation. These steps were added to ensure saturation and excess DSP pellet formation, respectively. Protein G was necessary to properly orient the F_c region of IgG toward the gold surface leaving the F_{ab} regions to bind antigen. Protein G was incubated at a concentration of 1 mg/mL for 2–4 h prior to washing.

After covalent protein G linkage to the resonator surface, the parylene-C layer was peeled from the resonator leaving the patterned protein G surrounded by the original gold electrode. Antibodies were labeled with Alexa Fluor 488 and Alexa Fluor 594, respectively, following the Molecular Probes protocol. Antibodies [polyclonal IgG goat anti-mouse (H + L) and antigen [polyclonal IgG mouse anti-rabbit (H + L)] were then added in successive 2–4 h incubation steps at 200 μg/mL. All proteins were obtained from Pierce Biotechnology, Inc.

Typically, rigorous repetitive substrate washing steps are required to remove nonspecific binding. Nonspecific binding removal results presented are in addition to rigorous washing. Each resonator was washed three times after each incubation step. Initial fluorescent intensity images were obtained after rigorous washing.

C. Resonator Fixture

The flow cell was machined out of two polycarbonate pieces (lid and base). A silicone seal was cast into the machined lid, and silicone tubing was cured into the silicone seal of the lid. The bottom half was machined to accept pogo pins for electrical contact. A photograph of the assembled fixture is shown in Figure 1.

Resonators were kept wet at all times prior to insertion into the flow cell. The flow cell was optimized for convenient electrical and fluidic connection to each resonator, as well as in situ observation, while still allowing repeated removal for quantitative imaging. The flow cell volume was 250 μL.

D. Electronic Equipment

The resonator input was generated by an Agilent (SA4402B) spectrum analyzer and amplified with an ENI 325LA broadband power amplifier. After liquid loading, each resonator was scanned over a large span to find the resonant frequency near 5 MHz.

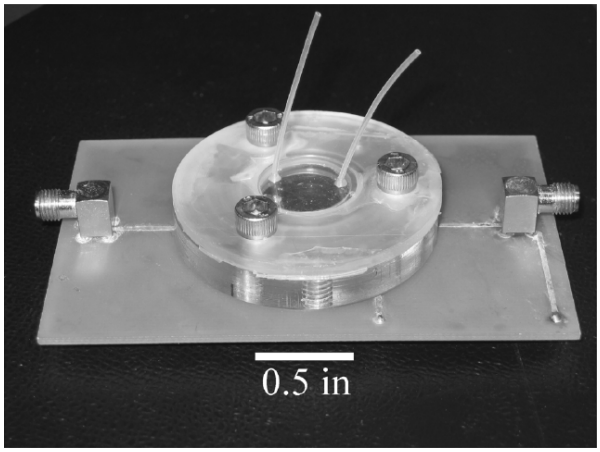

Figure 2.1. QCR flow cell with integrated fluidics and electrical connections.

The span about the center frequency was reduced to provide a relatively constant drive amplitude near resonance. Note that the span was not set to zero because mass desorption and temperature fluctuations shift the resonant peak. To account for shifts the analyzer was set to auto-track the resonant peak. Power delivered to a QCR was determined by measuring the return loss of the resonators and subtracting from the amplified output power.

Amplifier output powers reported within this chapter are significantly larger than the power reaching the transducer. Reported power is the peak amplifier output power reached during a frequency sweep. Input power levels reported in chapter three are adjusted to report the power dissipated into the fluid volume. Calorimetry measurements indicate only 1% of the amplifier power is transmitted into the fluid volume resting upon the resonator.

E. Imaging

Prepared resonators were imaged with a 20X NA 0.7 water immersion objective prior to placement in the flow cell. Images were taken near the center (active area) of each resonator, and all images were taken after removal from the flow cell. Photobleaching was observed during prolonged exposure; for accurate quantitation, the number of exposures was minimized. Quantitated images were taken in RGB mode with gain 8 and exposure times of 400 ms (488 nm) and 200 ms (594 nm) with an Olympus AX70 microscope and SPOT RT CCD. A filter cube transmitting fluorescence at both wavelengths (488 and 594 nm) was used to capture images without excessive photobleaching. Images used for quantitative analysis, therefore, result from photons emitted at both wavelengths. Critical to accurate background quantitation, gamma was always defined to be one, so as not to bias the image toward high intensity or low intensity pixels. Each image shown is unaltered beyond simple rotation and cropping. Images were taken at 1520 x 1080 pixel resolution, rotated, and

cropped to approximately 600 x 900 pixels. Image cropping was necessary to reduce systematic non-uniform illumination error. Rotation was performed prior to analysis to ensure algorithm fidelity.

F. Image Analysis

Image analysis code was written to discriminate between signal and background pixels. Complicating matters in intensity thresholding was nonspecific protein binding and protein aggregation [7]. Aggregates, ranging from nanometers to microns, bind strongly to both nonpatterned and patterned areas. Since a thresholding method based solely on intensity associates these bright particles as signal, the signal is improperly inflated and background deflated. *Figure 2* demonstrates the algorithm result after intensity thresholding *Figure 2(a)* and areal thresholding *Figure 2(b).* Arrays were used to compute the average signal, background, signal-to-background and standard deviation values. Statistics were generated from 540,000 pixel populations.

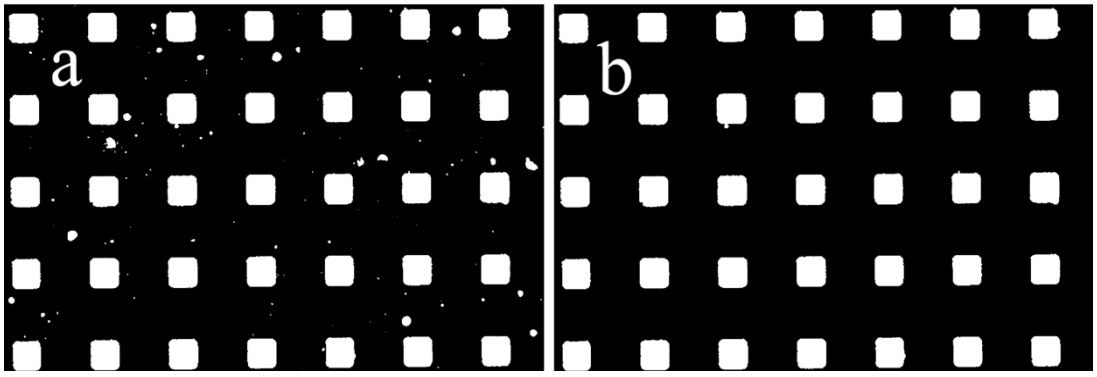

Figure 2.2. Digital image thresholding based on intensity and areal discrimination. (a) Fluorescent intensity image after pixel intensity discrimination and conversion to logical array. (b) Fluorescent intensity image after pixel intensity discrimination, areal discrimination, and conversion to logical array.

G. Atomic Force Microscopy Images

Atomic force microscope (AFM) measurements were made in tapping mode (Digital Instruments 3100 AFM). Devices were dried under nitrogen, and scanned with TESP cantilevers (Veeco).

III. RESULTS

A. Fluorescence Confirming Nonspecific Binding to Patterned Sensing Areas

Micropatterns clearly defined sensing and non-sensing areas. The non-sensing area acted as a control for both fluorescence and AFM experiments. *Figure 3(a)* and *(c)* shows the sensing and non-sensing regions. Digital image segregation of sensing and non-sensing areas was only achievable with a clearly defined pattern *(see Section II-F)*. Signal was defined as fluorescent intensity from the sensing squares. Background was defined as fluorescent intensity from the non-sensing area.

The optimal pH value of four maintained specific antibody/protein G interactions and removed the most nonspecific binding during resonator operation. Work from Åkerström *et al.* indicated that the region of IgG has the highest affinity for protein G at pH 4. Results at this pH follow in *Figure 3*. Fluorescent intensity values from *Figure 3(a)* and *(c)* were normalized after 3 mL of pH 4 PBS buffer was washed through the flow cell at 1 mL/min to remove fluid flow effects from data. *Figure 3(a)* was captured at experiment start and *Figure 3(c)* was captured after 20 min at 3.5 W input power.

Images analyzed throughout experiments demonstrated significant removal of nonspecifically bound protein adsorbed to both the micropatterned protein sensing array and non-sensing surface. Average signal and background values from *Figure 3(a)* and *(c)* are plotted in Figure *3(e)* and *(f)*. Intermediate data points were extracted from images not shown. Removal significantly improved sensing and non-sensing area fluorescent intensity uniformity. This result is evident in *Figure 3(e)* and *(f)*. With resonator operation, fluorescent intensity standard deviation values became progressively smaller compared to the control.

At low power levels (i.e., 3.5 W), nonspecific binding was removed primarily from non-sensing areas. Hence, the signal-to-background ratio value increased markedly. In

contrast, such significant nonspecifically bound protein removal from sensing areas occurred at 14 W that signal-to-background values increased only marginally [*see Figure 3(g)*]. It is crucial to observe that at 14 W, the signal-to-background ratio remained constant after high power operation. This indicates that QCR operation sets an affinity threshold. Above this threshold, specifically bound antibodies with affinities greater than the removal stress exerted by the QCR were retained, while nonspecifically bound antibodies were removed.

A constant signal-to-background ratio also indicates that the F_c–protein G and antibody-antigen binding interactions were maintained. Hence, after QCR operation, fluorescent intensity values resulting from specifically bound protein left after resonator operation accurately define the true signal. Pattern uniformity markedly improved, as demonstrated in *Figure 3(h)* and *(i)*, further validating the presence of only specifically bound species.

Fluorescent intensity from nonspecifically bound protein on non-sensing areas dropped by more than 85% and by 77% on sensing squares after resonator operation at 14 W, corresponding well with the AFM film thickness reduction demonstrated in the following AFM data section. Fluorescent intensity drops reported include nonspecific binding removal with fluid flow.

Figure 2.3. Qualitative and quantitative results demonstrating effects of QCR operation. (a) Initial fluorescent intensity image demonstrating nonspecifically bound protein and protein aggregation after pH 4 buffer pumped through flow cell at 1 mL/min for 3 min (IgG goat anti-mouse labeled with 488, IgG mouse anti-rabbit labeled with 594). (b) Initial surface chemistry illustration for Figure 3(a). (c) Image fluorescent intensity after driving QCR 20 min (3.5 W, pH 4). (d) Surface chemistry schematic after resonator activation for Figure 3(c). (e) Fluorescent intensity from sensing squares versus time at three power levels. Fluorescent intensity is from both 488 and 594 probes. Lines added to guide the eye, and fluorescent intensity standard deviation bars demonstrate fluorescence intensity nonuniformity in captured images. (f) Fluorescent intensity from non-sensing area versus time. (g) Average fluorescent square intensity divided by non-sensing area average intensity versus time plot at 3.5 and 14 W power levels. (h) Three-dimensional fluorescent intensity plot demonstrating aggregate intensity compared to pattern intensity before QCR operation. (i) Three-dimensional fluorescent intensity plot demonstrating uniform pattern fluorescent intensity after QCR operation (3.5 W, 20 min, pH 4).

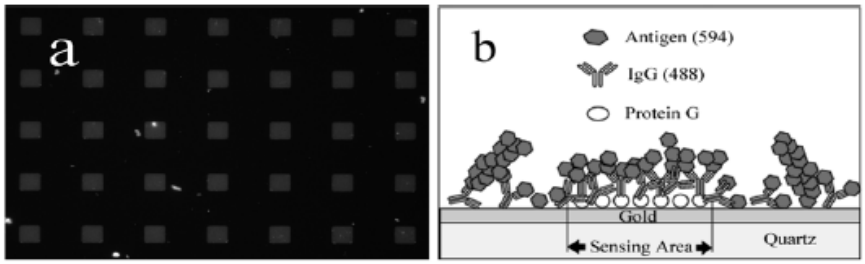
a
b
Antigen (594)
IgG (488)
Protein G
Gold
Sensing Area
Quartz

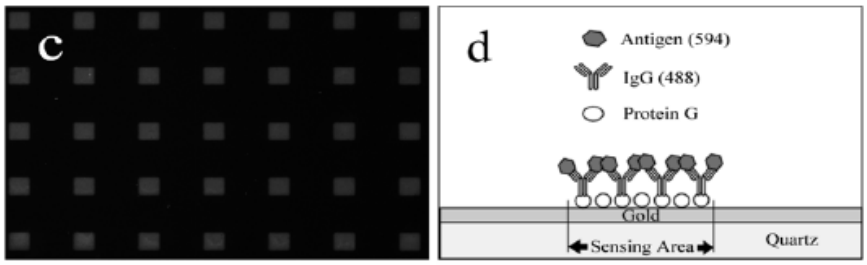
c
d
Antigen (594)
IgG (488)
Protein G
Gold
Sensing Area
Quartz

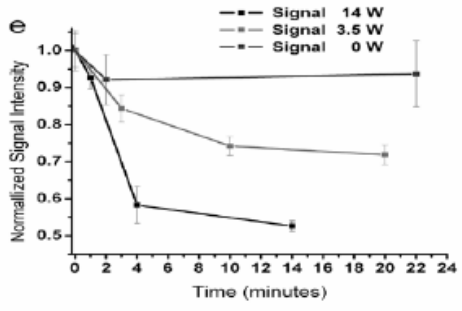
e
Signal 14 W
Signal 3.5 W
Signal 0 W
Normalized Signal Intensity
Time (minutes)

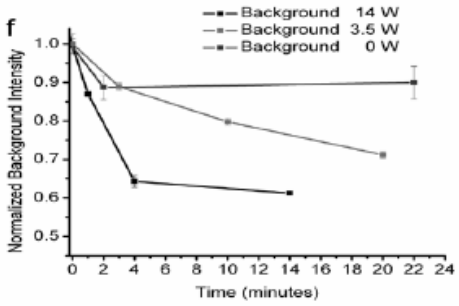
f
Background 14 W
Background 3.5 W
Background 0 W
Normalized Background Intensity
Time (minutes)

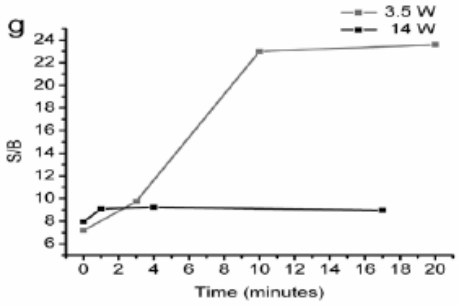
g
3.5 W
14 W
S/B
Time (minutes)

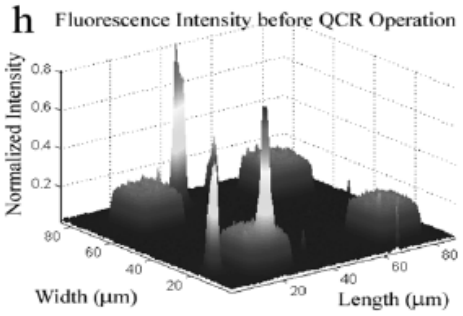
h
Fluorescence Intensity before QCR Operation
Normalized Intensity
Width (μm)
Length (μm)

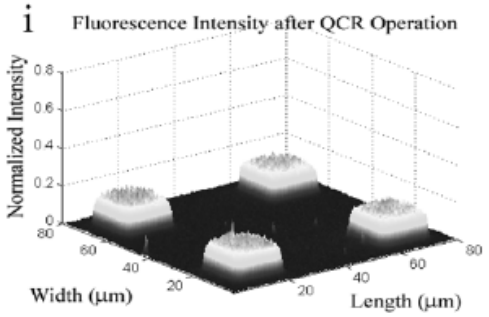
i
Fluorescence Intensity after QCR Operation
Normalized Intensity
Width (μm)
Length (μm)

To further confirm nonspecifically bound protein removal from patterned sensing areas, a resonator was patterned with nonfluorescent covalently bound protein G, followed by washing, parylene-C film removal, and incubation with nonfluorescent IgG goat anti-mouse. The resonator was then incubated for 4 h with Alexa 594 labeled protein G and washed. If protein G regions where antibodies are attached has only protein G—F_c region interactions, fluorescently tagged protein G should not bind to patterned areas to a greater degree than the non-sensing control area.

However, in *Figure 4(a)*, the pattern is highly visible and brighter than the background. Protein G must have bound to nonspecifically bound IgG goat anti-mouse. After resonator operation at 24.7 W, nonspecifically bound IgG goat anti-mouse bound to 594 labeled protein G were removed [*see Figure 4(c)*].

The maximum input power of 24.7 W was used in later experiments to verify that antibody film integrity was maintained at maximum power and to ensure that fluorescent intensity values after QCR operation at 14 W matched higher power operation fluorescent intensity values. Comparable fluorescent intensity signal values were obtained after QCR operation at both 14 and 24.7 W, which indicated that equivalent nonspecific binding protein quantities were removed at both 14 and 24.7 W. This experiment demonstrates a crucial point: Patterned IgG present after immobilization may not be covalently/specifically attached. Pattern heterogeneity has been demonstrated to reduce result repeatability and alters adsorption kinetics [8].

To eliminate the possibility that specifically bound IgG goat anti-mouse was removed and the antigen bound directly to the covalently bound protein G, a resonator was prepared with IgG goat anti-mouse labeled with Alexa 488. After operation (24.7 W, 2 min, pH = 4), Figure 4(d) was captured with an 100X objective. At this magnification, it is evident that the pattern was uniform and the IgG goat anti-mouse capture layer was still present.

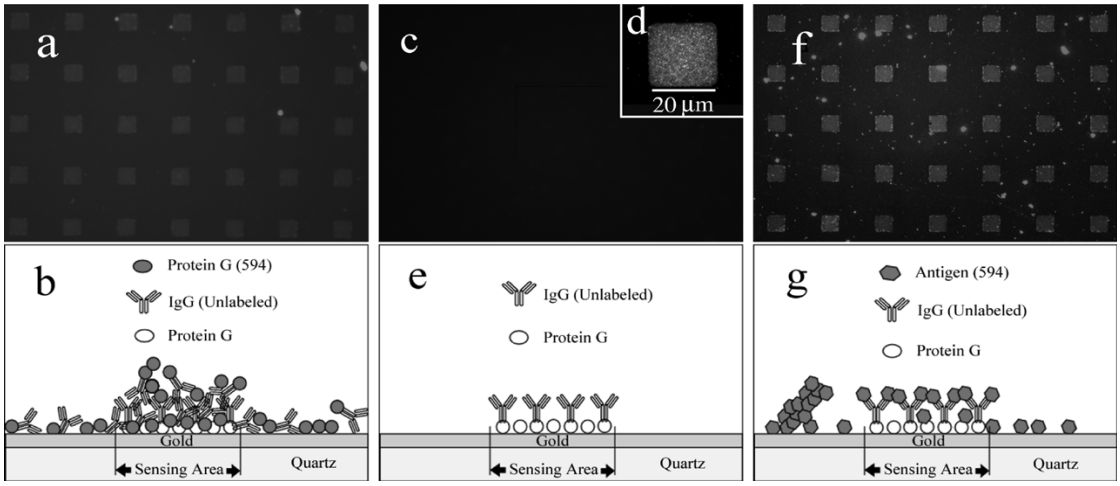

Figure 2.4. Fluorescence data confirming nonspecific protein binding to sensing area and maintained antibody activity after QCR operation. (a) Initial fluorescent intensity image demonstrating protein G binding to F_c region of nonspecifically bound IgG goat anti-mouse on sensing and non-sensing areas. Nonspecifically bound IgG goat anti-mouse (unlabeled) causes fluorescently labeled protein G to bind. (b) Initial surface chemistry illustration for Figure 4(a). (c) Fluorescent protein G and nonspecifically bound (unlabeled) IgG goat anti-mouse removed with QCR operation (24.7 W, 2 min, pH 4). (d) Additional fluorescent intensity image from different resonator prepared with unlabeled protein G and only Alexa 488 labeled IgG goat anti-mouse and driven (24.7W, 2 min, pH 4). High magnification demonstrates single square uniformity and antibody capture layer presence. (e) Surface chemistry illustration for Figure 4(c). Antibody (IgG goat anti-mouse) was Alexa 488 labeled for inset 4(d). (f) Fluorescent intensity image captured after Antigen (Alexa Fluor 594 labeled IgG mouse anti-rabbit) was added to demonstrate antibody activity after high-power QCR operation. (g) Surface chemistry after antigen addition for Figure 4(f). Note that the resonator could be cleaned again with activation.

Adding Alexa 594 labeled antigen (IgG mouse anti-rabbit) demonstrated that the specifically bound IgG goat anti-mouse (unlabeled), bound to the patterned protein G squares, was still active after high shear [*see Figure 4(f)*].

To illustrate the fluorescent labeling in each fluorescent image, corresponding surface chemistry schematics are shown following the respective fluorescent intensity image [*see Figure 4(b), (e), and (g)*], which is paired with *Figure 4(a), (c),* and *(f),* respectively. *Figure 4(d)* has identical surface chemistry to *Figure 4(c)*, but with Alexa 488 labeled IgG goat anti-mouse on a separately prepared device.

After QCR operation more reproducible values were obtained. Three images were taken from different areas on each of two separate resonator surfaces on two identically prepared devices driven for 20 min at 3.5 W. Results from each device are shown in *Figure 5*. Both inter and intra-device fluorescent intensity signal values varied significantly before operation. Intra-device signal variability was as high as 37% from area to area, while inter-device signal variability was as high as 24% in two identical device preparations. After QCR operation, intra-device fluorescent intensity signal values varied by only 9%, and inter-device fluorescent intensity signal values varied by 14% in the worst case scenarios.

B. AFM Data Confirming Nonspecific Binding on Patterned Sensing Areas and Subsequent Removal with QCR

Resonator operation removed nonspecifically bound protein and aggregates on all areas. To ensure that only nonspecifically bound protein removal occurred, AFM images were obtained using dried resonators. No resonator was operated after drying.

Three separate resonators were imaged, two before, and one after operation. The first image was taken with a resonator prepared with patterned protein G, IgG goat anti-mouse, and antigen. Parylene was removed prior to IgG and antigen incubation steps. The pattern is visible, but is blanketed by nonspecifically bound protein layers, and large protein aggregates [*see Figure 6(a) and (b)*].

To determine the absolute pattern height, the entire protocol (linker, protein G, IgG goat anti-mouse, and antigen) was repeated without removing parylene until the end. Washing steps were performed after each incubation step and after parylene removal. The film thickness was much greater than the expected 29 nm, indicating that multiple layers existed on the patterned sensing areas [*see Figure 6(c) and (d)*].

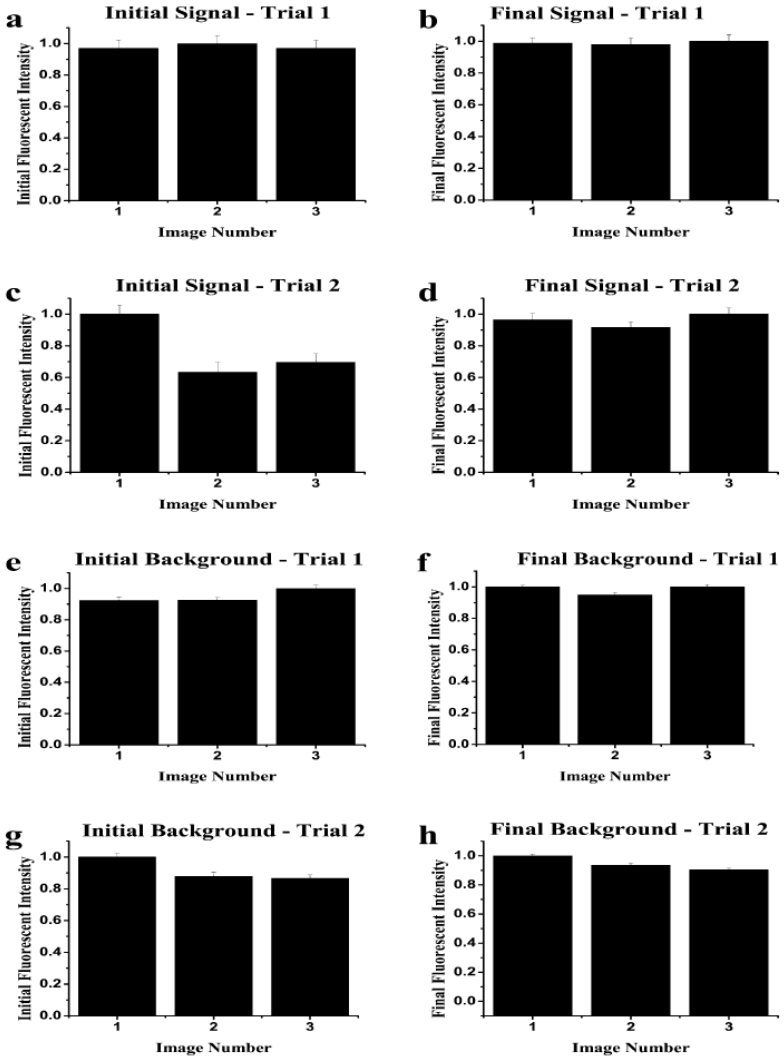

Figure 2.5. Fluorescent intensity signal and background data before and after 3.5 W QCR operation for 20 min. Three unique areas imaged on each of two separate identically prepared QCRs. (a), (b) Trial 1: Initial/final fluorescent intensity signal values from three areas on the first QCR surface. (c), (d) Trial 2: Initial/final fluorescent intensity signal values from three areas on the second QCR surface. (e), (f) Trial 1: Initial/final fluorescent intensity background values from three areas on the first QCR surface. (g), (h) Trial 2: Initial/final fluorescent intensity background values from three areas on the second QCR surface.

Another resonator was prepared as described in the introduction and operated at high power (24.7 W, 2 min, pH = 4). This power level significantly reduced pattern intensity. Contrary to what might be expected, the film was not sheared from the surface, but, in fact, a film thickness much closer to 29 nm was found [*see Figure 6(e) and (f)*]. Intensity data combined with AFM results indicated that film uniformity was significantly improved after QCR operation. At this power, sensing area chemistry accurately matched the intended chemistry, not a mixture of specifically and nonspecifically bound antibody.

C. Antibody Capture Layer Removal

At pH 2.8 protein G/IgG interactions are disrupted. To explore additional purification and preconcentration applications, buffer was switched from the incubation buffer (pH 7.4) to pH 2.8 with the resonator operating at 1.8 W. Rapid antibody elution resulted. After 5 min, the resonator was removed and imaged. Both nonspecifically and specifically bound protein were removed with 94% efficiency. Hence, QCRs could be used to purify antigen and later release it for downstream analysis. Adding a new antibody as a capture layer may yield a regenerated surface. This process was not explored beyond IgG release.

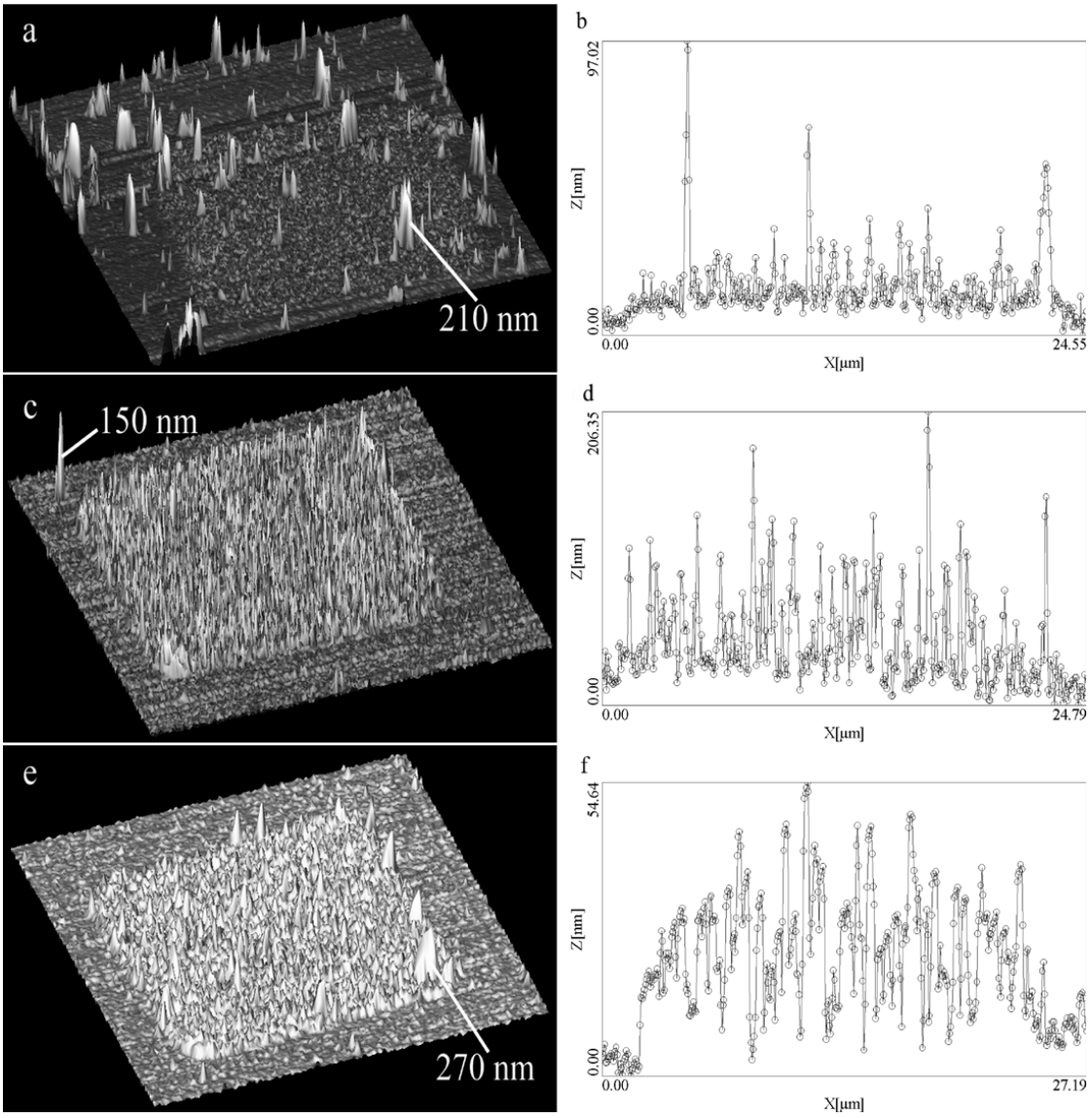

Figure 2.6. AFM data confirming nonspecific protein binding on patterned sensing areas and subsequent removal with QCR. (a) Initial AFM image demonstrating nonspecifically bound IgG blanketing patterned area and protein aggregate size. (b) Line scan across AFM image 6(a). (c) AFM image after parylene removal (linker, protein G, IgG goat anti-mouse, antigen all incubated prior to parylene removal). Baseline was gold surface. (d) Line scan across AFM image 6(c). (e) Pattern after QCR operation at 24.7 W. (f) Line scan across AFM image 6(e). Note significant thickness drop compared to Figure 6(d).

IV. CONCLUSION

Biosensors and bioassays should ideally be fast, simple, and accurate. Most importantly, neither false positives nor false negatives should result. Nonspecific binding can create false signal, or mask true signal. It also increases assay variability and decreases assay accuracy. We have demonstrated an approach to remove nonspecific binding and improve assay reproducibility and signal validity. Our results confirm quartz crystal resonator operation increases pattern uniformity and simplifies data analysis. This problem is chemically intractable on areas with sensing molecules, and, hence, this mechanical approach should prove valuable for high sensitivity/specificity bioassays, protein-protein interaction studies, library screening, purification, and biosensors. This method may be extended using alternative mechanisms to generate shear stress at a substrate surface.

ACKNOWLEDGMENT

The authors would like to thank M. Zalalutdinov, K. Aubin, R. Reichenbach, and R. Ilic for electrical engineering and fabrication help.

REFERENCES

[1] A. W. Liew, H. Yan, and M. Yang, “Robust adaptive spot segmentation of DNA microarray images,” *Pattern Recognit.*, vol. 36, pp. 1251–1254, 2003.

[2] Y. Chen *et al.*, “Ratio statistics of gene expression levels and applications to microarray data analysis,” *Bioinformatics*, vol. 18, no. 9, pp. 1207–1215, 2002.

[3] L. Jespers, O. Schon, K. Famm, and G. Winter, “Aggregation resistant domain antibodies selected on phage by heat denaturation,” *Nature Biotechnol.*, vol. 22, no. 9, pp. 1161–1165, Sep. 2004.

[4] L. McKenna, MI. Newton, G. McHale, R. Lockland, and J. Schroeder, “Compressional acoustic wave generation in microdroplets of water in contact with quartz crystal resonators,” *J. Appl. Phys.*, vol. 89, no. 1, pp. 676–680.

[5] B. Ilic and H. G. Craighead, “Topographical patterning of chemically sensitive biological materials using a polymer based dry lift off,” *Biomed. Microdevices*, vol. 2, no. 4, pp. 317–322, 2000.

[6] B. Åkerström and L. Björck, “A physicochemical study of protein G, a molecule with unique immunoglobulin G-binding properties,” *J. Biol. Chem.*, vol. 261, no. 22, pp. 10 240–10 247, Aug. 1986.

[7] N. Otsu, “A threshold selection method from gray level histograms,” *IEEE Trans. Syst., Man, Cybern.*, vol. SMC-9, no. 1, pp. 62–66, Jan. 1979.

[8] R. Vijayendran and D. Leckband, “A quantitative assessment of heterogeneity for surface-immobilized proteins,” *Anal. Chem.*, vol. 73, pp. 471–480, 2001.

CHAPTER THREE

Modulating Protein Release Kinetics with Nanoscale Oscillations

*Grant Meyer & Harold G. Craighead**

Cornell University, School of Applied Physics, Clark Hall, Ithaca, New York 14853

E-mail: gdm24@cornell.edu, *hgc1@cornell.edu

ABSTRACT

Proteins are folded amino-acid strands with nanoscale dimension. Within and between proteins, nanoscale fluctuations influence protein-protein interaction kinetics. We demonstrate improved mass transport and modulate protein kinetics with nanoscale oscillations introduced by quartz crystal resonators. Nanoscale oscillations dissipate in fluid resting upon the resonator causing time-varying, localized changes in pressure, velocity, and temperature, altering molecular energy-level distributions. Energy-level redistribution changes system equilibrium, routinely characterized with rate constants (k_{on} and k_{off}). When applied to immunoassays, the kinetic release constant (k_{off}) for antigen release was increased by up to one order of magnitude, while the kinetic constant for nonspecifically bound bovine serum albumin release was increased by two orders of magnitude. Quantitative analysis yielded an optimal power of 100 mW for nonspecific binding release. Choosing the optimal power rapidly removed nonspecifically bound protein with minimal antigen loss in seconds. Kinetic data are presented to quantify the increase in the bound-to-free transition probabilities

for high-affinity, specific, antigen release from an antibody, and low-affinity, nonspecific, protein elution resulting from nanoscale quartz crystal resonator oscillations. Affinity probes are indispensable in molecular diagnostic, biosensor, and biotherapeutic applications, and, hence, this method has potential immunoassay, affinity probe screening, and rapid sensor surface regeneration utility.

I. INTRODUCTION

Clinical immunoassay manuscripts were first published in the 1960s [1]. Nearly fifty years later, rapid, reliable bioassays often prove cumbersome, requiring extensive automation, routine calibration, and rigorous field testing. Often, complex protein engineering is required to improve probe affinity and specificity. Alternatively, expensive monoclonal antibodies are raised and screened for high affinity/ specificity. Because significant effort is required to yield one affinity/specificity matured recombinant protein, it is not surprising multiplexed arrays remain largely in the research phase. Detailed immunoassay history is discussed by Ekins [2].

While large array feasibility is debatable [3], the problem nonspecific binding presents is not. Articles suggest protein cross-reactivity and nonspecific binding may prove “insurmountable” when addressing multiplexed immunoassays or microarrays [4]. Rather than accept this argument, we sought to better understand the statistical mechanics behind protein-protein interactions and employ this knowledge to accelerate immunoassays. Leveraging this knowledge, we produce results demonstrating an increase in the rate constant disparity between strongly and weakly bound protein yielding optimal nonspecific binding removal.

Nearly all immunoassays rely on a solid support and affinity probes to separate bound and free sample constituents (*see Figure 1*). However, when performing affinity-based separation in a microfluidic or on-chip system, “it is not practical to

provide vigorous washing of the type advocated to achieve >99.99% separation efficiency" [5]. Such separation steps are termed *washing steps*. Inefficient washing increases assay time requirements. Incomplete washing leaves nonspecific signal, while excessive washing elutes true signal, potentially causing a falsely negative or positive result.

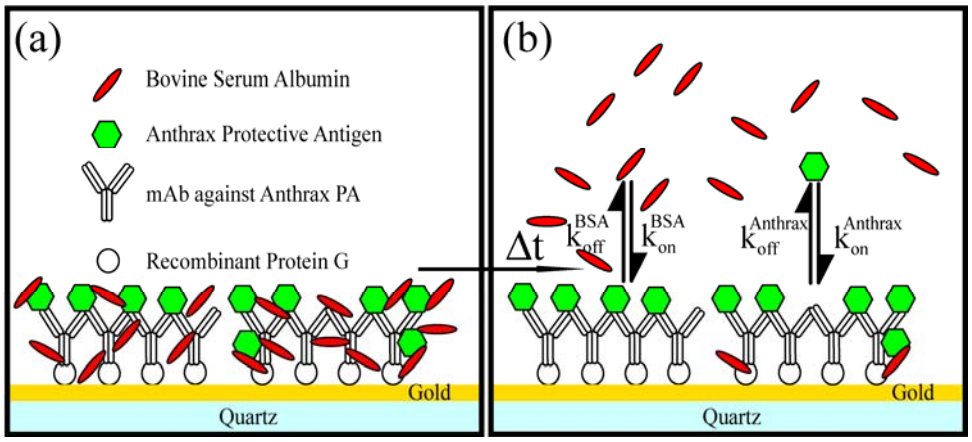

Figure 3.1. The standard solid-support immunoassay and chemical kinetics of strongly and weakly binding proteins. (a) Surface chemistry for fluorescence microscopy experiments. Protein spatial orientation at elution experiment initiation. **(b)** Protein spatial orientation as experiment progresses. Protein elutes as buffer is exchanged. Release is dependent upon temperature and protein amino-acid structure/dynamics (i.e. affinity). Antibodies bind antigen with high affinity. Background proteins bind nonspecifically, commonly, with lower affinity

While ubiquitous, solid supports alter the physical forces exerted on immobilized biomolecules. Extensive literature details surface chemistries and alterations in protein properties [6-10]. Importantly, Fang *et al.* indicate protein adsorption can be mitigated, yet not prevented, with improved surface chemistry.

Technologies routinely used to determine ligand-receptor kinetic parameters include surface plasmon resonance (SPR), fluorescence-based measurements, and force-based measurements [11-18]. Although tremendous economic and human resources fuel improvement and validation, assays still prove challenging. Perennial concerns include nonspecific binding, promiscuous binding, and cross-reactivity [14, 15]. To

our knowledge nonspecific binding, promiscuous binding, and cross-reactivity all refer to low-affinity binding to immobilized capture molecules. For our purposes we term low-affinity binding to be non-specific binding because no catalytic component is involved (i.e. we are concerned only with protein—protein interaction rather than enzyme catalysis). Further, in developing rapid kinetic-based screening of human F_{ab} fragments, Steukers *et al.* discuss challenges in identifying and screening high-affinity F_{ab} fragments.

In addition to nonspecific binding, avidity, mass transport, steric hindrance, and aggregation may also affect assay results [19, 20]. In this work, we detail how phonon attenuation at the solid-support reduces nonspecific binding and improves mass transport. Our previous work details nonspecific binding, protein aggregate removal, and the experimental setup [21].

Quartz crystal resonators are commercially available, robust, and easily excited with proper electrical equipment. Devices are well-suited for multiplexing, standard fabrication processes, and existing immunoassay surface chemistries. Resonators operate with a 5 MHz fundamental frequency. Excitation generates nanoscale surface deformation, which couples into liquid resting on the resonator surface. The resonator surface acts as a solid-support for protein/antibody immobilization.

Kessler & Dunn discuss acoustic wave propagation creating time-varying, localized changes in pressure, density, and temperature. Acoustic wave energy absorption by proteins alters molecular energy level populations. Through this mechanism, wave motion perturbs molecular equilibria at rates which depend on the sound frequency [22]. We hypothesized nanoscale oscillations generated by quartz crystal resonators could increase the bound-to-free transition probability for weakly and strongly adsorbed protein without markedly increasing temperature or altering reagent pH.

II. EXPERIMENTAL METHODS & MATERIALS

All quartz crystal resonators were obtained from Maxtek. Operating frequency, controlled by crystal thickness, was 5 MHz for all devices. AT-cut Quartz crystals were coated with chrome/gold.

Devices were cleaned with acetone, methanol, ethanol, isopropyl alcohol, and dried with nitrogen. The covalent linkage protocol is detailed in *Reference 21*. Protein G was incubated on dithiobis[succinimidylpropionate] devices for 2-3 hours followed by extensive washing and buffer immersion for 30 minutes. Antibody was added and incubated for 30 minutes followed by extensive washing. BSA labeled with AlexaFluor 594 (0.5 mg/mL) and Anthrax PA labeled with AlexaFluor 488 (20 micrograms/mL) were incubated on devices for 30 minutes simultaneously for nonspecific release kinetics. Two 30 second immersions in 5 mL IgG binding buffer were performed prior to fixture insertion.

Protein G and BSA were obtained from Pierce Biotechnology, Inc. The monoclonal antibody was obtained from List Laboratories, Inc. Anthrax protective antigen was obtained from Biodesign International, Inc.

Devices were excited using an Agilent spectrum analyzer (1 sec sweep, span 20 kHz about the device center frequency at ~5 MHz, SA4402B). AC-Voltage output was amplified by a ENI 325LA broad-band power amplifier.

The buffer used for all experiments was IgG binding buffer obtained from Pierce Biotechnology, Inc. Buffer pH was 8.0. This buffer was used given manufacturer documentation indicating product optimization for the Protein G/ Antibody F_c region interaction. Flow rate through the QCR fixture was 1 mL/min.

The fixture holding the resonator in place was machined from Lexan. A coverglass was used to create a window over the QCR active area. To minimize protein binding

to the coverglass, the coverglass was coated with PEG-silane obtained from Gelest, Inc. A photograph depicting the device fixture is pictured in *Reference 21*. Buffer temperature measurements were made using a Lake Shore thermocouple system.

III. RECEPTOR—LIGAND BINDING KINETICS

Protein—protein interaction kinetics are modeled in the literature as receptor—ligand interactions. Written chemically,

$$R + L \underset{k_{off}}{\overset{k_{on}}{\rightleftharpoons}} C \quad \textbf{(1)}$$

Antigen (ligand—L) binds to surface bound antibodies (receptor—R) with characteristic rate constants k_{on} and k_{off}, which characterize protein adsorption and desorption rates. Written in differential form, *Equation 1* becomes,

$$\frac{dC}{dt} = k_{on}RL - k_{off}C \quad \textbf{(2)}$$

In this work we characterize,

$$C \xrightarrow{k_{off}} R + L \quad \textbf{(3)}$$

This equation holds if $k_{on}RL = 0$. This assumption is valid if rapid transport away from the surface upon release makes L, the free solution ligand concentration, zero. Given the high fluid velocities generated by QCRs and constant pure buffer infusion, this assumption is reasonable.

In differential form, *Equation 3* becomes,

$$\frac{dC}{dt} = -k_{off} C \quad \textbf{(4)}$$

Increasing QCR input power increases fluctuation amplitude and average buffer—protein collision frequency. Acoustic oscillations alter system equilibria (i.e. QCR introduced oscillations shift k_{on} and k_{off}) [22, 23]. We quantify the power-dependent change in $k_{off} = k_{off}(P)$, where P is the power input by the QCR.

$$C(t=0) = C_0 + C_1 \quad \textbf{(5)}$$

In *Equation 5*, *C*, the total protein—substrate complex number is fragmented to explicitly account for multiple binding affinities (i.e. multiple k_{off} values). Solving *Equation 4*, where $k_{0,1}$ are the release rate constants with the initial condition given in *Equation 5* yields,

$$C(t) = C_0 \exp(-k_0 t) + C_1 \exp(-k_1 t) \quad \textbf{(7)}$$

In our experiments, *C* is proportional to the fluorescent signal intensity, and, therefore, we write,

$$I(t) = I_0 \exp(-t/\tau_0) + I_1 \exp(-t/\tau_1) \quad \textbf{(8)}$$

Where

$$k_{0,1} = \frac{1}{\tau_{0,1}} \quad \textbf{(9)}$$

In instances where a protein sub-population has a slow kinetic release constant (relative to the experimental time-scale) we can treat the system as an exponential decay with an additional constant quantifying the strongly bound sub-population quantity. Experimental data fit well with a first order exponential decay. In the respective limit,

$$\tau_1 \longrightarrow \infty \quad \textbf{(10)}$$

$$I(t) = I_0 \exp(-t / \tau_0) + I_1 \quad \textbf{(11)}$$

Equation 11 was used to fit intensity data in *Figure 2*. Decay time and rate constant (τ_0 and k_{off}) values for nonspecifically (BSA) and specifically (PA) bound protein are listed in *Tables 1 and 2*. Fitting data to *Equation 11* provides information about protein—substrate release time constants and strongly bound population proportions. By incrementally increasing the input power reaching the QCR, we can quantify the influence QCR input power has on protein desorption kinetics.

Protein binding and release kinetics under physiological conditions are excited solely by thermal fluctuations. We introduce periodic nanoscale oscillations with a period of ~200 nanoseconds into a system containing buffer and proteins. The oscillations introduced by quartz crystal resonators increase the translational kinetic energy of free buffer/protein molecules, modulate solvation kinetics, and induce conformational transitions for bound buffer/protein molecules as detailed in *References 24-27*. Protein release rates increase with oscillation amplitude. A

power-dependent rate constant increase is demonstrated for both high and low-affinity interactions.

Proteins immobilized on the resonator surface, the solid-support, include Anthrax protective antigen (PA) bound to a monoclonal antibody against an epitope on PA, and bovine serum albumin (BSA) bound nonspecifically. The antibody-antigen interaction is a high-affinity interaction, while the BSA binds with low-affinity (i.e. nonspecifically).

Oscillations generated by quartz crystal resonators increase mass transport at the solid-liquid interface *via* forced-convection, apply a hydrodynamic drag force to bound biomolecules, influence solvation, and dissipate energy into conformational transitions.

At the low input powers chosen, chemical kinetics are influenced without significant temperature changes. The average temperature range was between 24.0 at ambient temperature and 32.0 +/- 0.5 °C depending upon resonator input power. Hence, this method should prove valuable in biotechnology, lab-chip, multiplexed assays, and high-throughput affinity screening applications. We acknowledge temperature is a critical factor influencing kinetics, perhaps significantly. Temperature values indicate the power delivered to the fluid did not exceed physiological temperature (i.e. 37 °C).

IV. RESULTS

To test our hypothesis, rate constant increase for a weak, nonspecific interaction, generating rapid release while minimally altering a strong, specific interaction, we analyzed two interactions: (1) The strong interaction between monoclonal antibody against Anthrax protective antigen and Anthrax protective antigen (PA), and (2) The weak interaction between bovine serum albumin (BSA) and immobilized antibody/antigen. PA was fluorescently tagged to emit green photons and BSA was

fluorescently tagged to emit red photons. Protein orientations and kinetic release curves are shown in *Figure 2*.

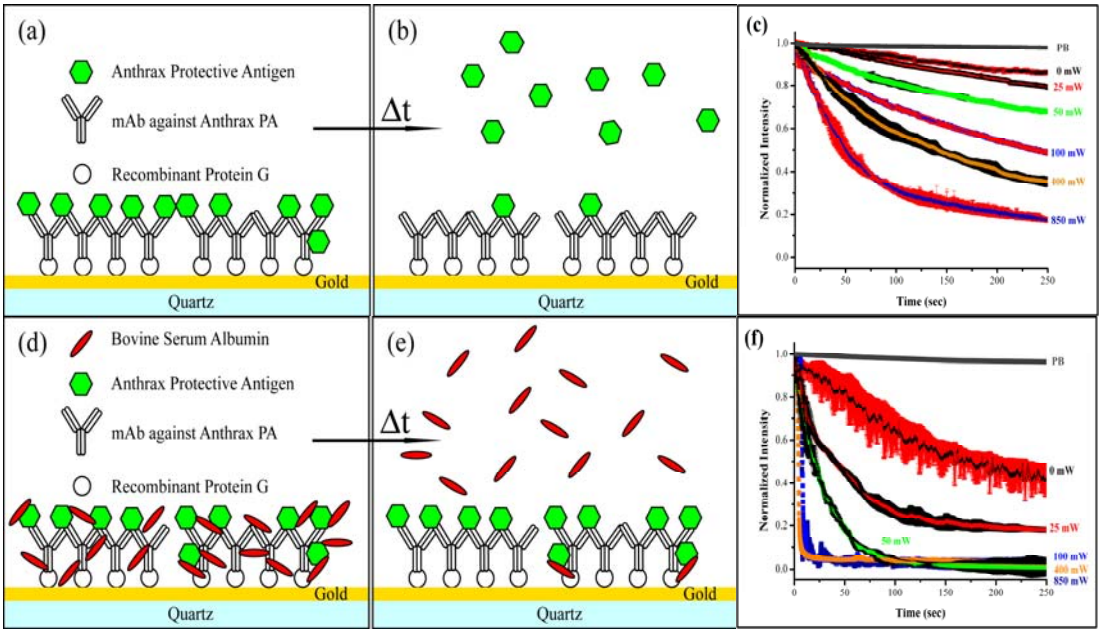

Figure 3.2. (a,b,c) PA surface chemistry and desorption curves for incrementally increasing resonator power levels. (d,e,f) BSA surface chemistry and desorption curves for incrementally increasing resonator power levels. Error bars represent the deviation from the mean value generated from two elution experiments repeated at each input power.

Table 3.1. Protein desorption fit parameters and rate constants for PA. Reference *Figure 2(c)*. $I(t) = I_0 \exp(-t/\tau_{PA}) + I_1$

Power dissipated into fluid volume	I_0	$\tau_{(PA)}$ (s)	I_1	$k_{off\,(PA)}$ (s^{-1})
0 mW	0.34 +/- 0.01	444 +/- 16	0.66 +/- 0.01	0.0023
25 mW	0.53 +/- 0.01	429 +/- 3	0.47 +/- 0.01	0.0024
50 mW	0.62 +/- 0.03	370 +/- 2	0.35 +/- 0.02	0.0027
100 mW	0.71 +/- 0.01	245 +/- 1	0.23 +/- 0.01	0.0041
400 mW	0.77 +/- 0.01	146 +/- 1	0.20 +/- 0.01	0.0068
850 mW	0.83 +/- 0.01	57 +/- 1	0.17 +/- 0.01	0.0233

Table 3.2. Protein desorption fit parameters and rate constants for BSA. Reference *Figure 2(f)*. $I(t) = I_0 \exp(-t/\tau_{BSA}) + I_1$

Power dissipated into fluid volume	I_0	$\tau_{(BSA)}$ (s)	I_1	$k_{off\ (BSA)}$ (s^{-1})
0 mW	0.86 +/- 0.01	215 +/- 5	0.14 +/- 0.01	0.0047
25 mW	0.75 +/- 0.01	45 +/- 1	0.18 +/- 0.01	0.0222
50 mW	0.96 +/- 0.01	29 +/- 1	0.01 +/- 0.01	0.0345
100 mW	0.96 +/- 0.02	< 5	0.04 +/- 0.02	> 0.2
400 mW	0.96 +/- 0.02	< 5	0.04 +/- 0.02	> 0.2
850 mW	0.96 +/- 0.02	< 5	0.04 +/- 0.02	> 0.2

Intra-frame Error Analysis

Individual kinetic curves were generated by computing the mean image intensity from 1,372,800 pixel populations (1392 x 1080 pixels). A small number of pixels were saturated in experiments. Presumably, pinholes in the gold provide nucleation sites around which protein aggregates, resulting in higher intensity pixels. Aggregate pixel percentages are listed in *Tables 3 & 4*. Pixel population percentages were computed by calculating a mean frame intensity value, the intra-frame standard deviation value, and the number of pixels with intensity three standard deviations above the mean. The last number was divided by the total pixel population size to generate a percentage.

Table 3.3. PA pixel percentage with intensity greater than 3 standard deviations above mean value at experiment beginning & end.

Power dissipated into fluid volume	Pixel Percentage (Before)	Pixel Percentage (After)
0 mW	1.03%	0.95%
25 mW	1.37%	1.15%
50 mW	1.13%	0.83%
100 mW	0.78%	0.54%
400 mW	0.79%	0.35%
850 mW	0.89%	0.36%

Table 3.4. BSA pixel percentage with intensity greater than 3 standard deviations above mean value at experiment beginning & end.

Power dissipated into fluid volume	Pixel Percentage (Before)	Pixel Percentage (After)
0 mW	1.07%	0.78%
25 mW	1.51%	1.09%
50 mW	1.31%	0.64%
100 mW	1.85%	0.72%
400 mW	1.17%	0.79%
850 mW	2.13%	0.35%

Intra-frame standard deviation value analysis indicates the dominant error is inter-experimental rather than intra-experimental. The error bars in *Figure 2* represent the dominant inter-experimental error generated by taking the average of two decay curves and calculating the standard deviation about the mean at each time point.

Note: Producing a standard deviation value, by definition, assumes a Gaussian pixel intensity distribution. The pixel intensity histograms exhibit Gaussian distribution characteristics with slight Lorentzian character, a "fatter" tail shifting the pixel distribution slightly towards higher intensity (<1% mean bias toward higher intensity). Lorentzian character commonly indicates an autocatalytic process is present. Aggregation exhibits self-similar (non-Gaussian) character. Data indicate this deviation from a Gaussian distribution is slight.

Figure 3(a) plots the nonspecific/specific intensity ratio *vs.* time using fit parameters listed in Tables 1 & 2. Figure 3(b) plots the desorption decay constant ratio at each experimental power.

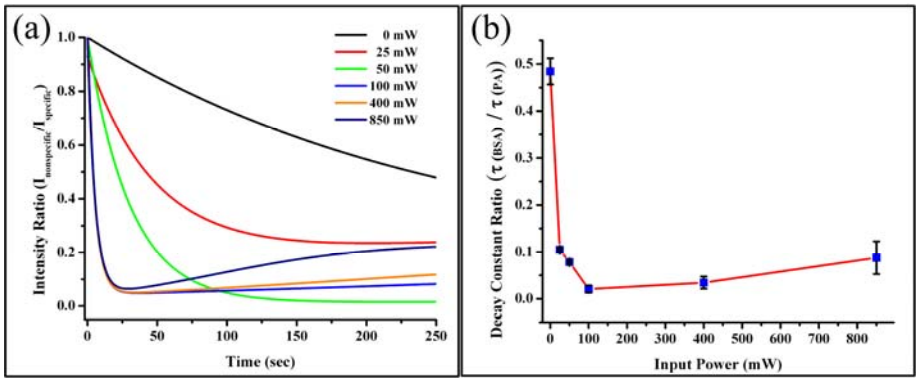

Figure 3.3. (a) Nonspecific/specific intensity ratio *vs.* time. Curves generated using model fit parameters listed in *Tables 1 & 2.* **(b) Desorption rate disparity factor (R_τ) at each power.** Data points generated by dividing τ (BSA) by τ(PA) at each power (line added to guide the eye).

Figure 4 plots the curves in *Figure 3(a)* with confidence bands generated by including the upper and lower bounds resulting from inter-experimental measurement error.

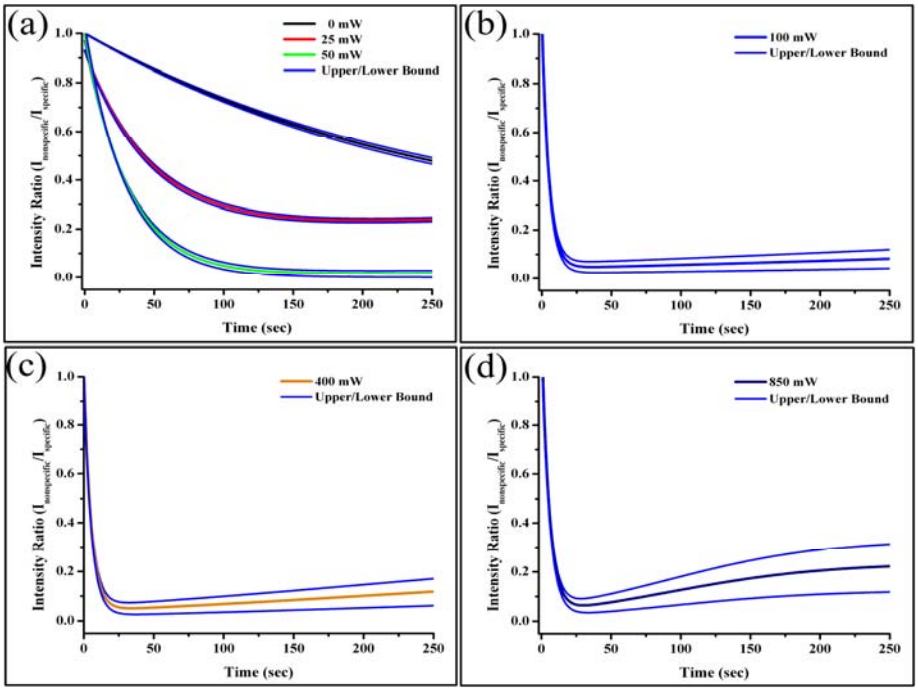

Figure 3.4. Nonspecific/specific intensity ratio plots with standard deviation upper/lower bounds plotted for individual curves (Center curves are identical to those plotted in Figure 3(a)).

Protein interactions are strongly influenced by pH. Changing pH disrupts surface immobilized protein interactions. Changing pH from 8 to 3, in effect, "turns off" specific interactions. Affinity is reduced because protein solvation is changed and protein structure is altered. Measuring elution upon buffer exchange demonstrates the diffusion limitation at the interface. By activating the resonator we clearly observe improved transport and accelerated solvent exchange at the solid support. Mass transport at the interface is slow, and, therefore, commonly problematic for SPR and electrochemical measurements. *Figure 5* depicts the effect schematically in 5(*a,b)* and kinetically in *5(c).*

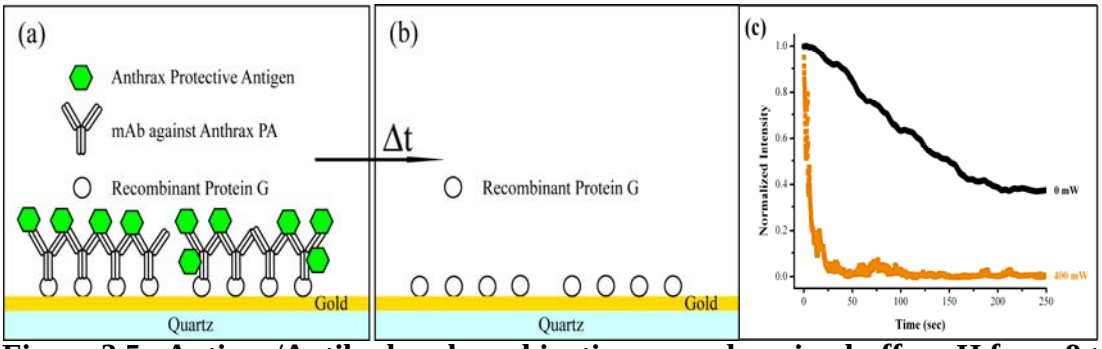

Figure 3.5. Antigen/Antibody release kinetics upon changing buffer pH from 8 to 3. Changing pH alters the solvation, and, hence, non-covalent interactions are disrupted. Resonator activation accelerates solvent exchange and transport away from the diffusion limited region near the solid-support.

Table 3.5. Protein desorption decay constants for Antigen/Antibody release upon changing buffer pH from 8 to 3. Reference *Figure 5(c)*. $I(t) = I_0 \exp(-t/\tau_{PA}) + I_1$

Power dissipated into fluid volume	I_0	$\tau_{(PA)}$ (s)	I_1	$k_{off\ (PA)}$ (s^{-1})
0 mW	0.93 +/- 0.01	163 +/- 2	0.13 +/- 0.01	0.0061
400 mW	0.87 +/- 0.01	7 +/- 1	0.01 +/- 0.01	0.1429

V. DISCUSSION

Although adsorbed protein is bound in a strong potential well, the particle cannot be treated as a solid, but rather, as a biopolymer with subdiffusive behavior interacting with the bath. Energy injected by the resonator alters protein solvation and induces amino acid strand fluctuations, accelerating protein desorption.

A rigorous release rate model for k_{off} developed to understand stochastic release from an energy-well with a saddle-type transition state was developed by Kramer's from Smoluchowski theory. The bound-to-free transition probability is considered a diffusive flux of thermalized states along a specific reaction coordinate. More recently,

manuscripts discuss the complexity of ligand-receptor interactions [28-32]. Evans stresses the importance of loading rate ($\Delta F/\Delta t$) and discusses the following two equations arising from Kramers' theory for the transition probability given an energy-well with a saddle-type transition state. Kramers' result is:

$$\frac{1}{\tau_{off}} = \frac{1}{\tau_A}\exp[\frac{-E_b}{k_B T}] \quad \textbf{(12)}$$

In this equation, $1/\tau_{off}$ is the overdamped attempt frequency, $1/\tau_A$ represents the attempt frequency created by white noise excitation ($k_B T$) neglecting viscous damping (~10^9-10^{10} sec^{-1}), E_b is the energy well depth, k_B is Boltzmann's constant and T is temperature. Given more explicitly by Evans,

$$k_{off} = \frac{D}{l_{bs} l_{ts}}\exp[\frac{-E_b}{k_B T}] \quad \textbf{(13)}$$

Equation 13 details the relationship between a protein's release rate and mass transport (diffusion constant—D), bound state energy-well parameters (l_{bs}, l_{ts}, and E_b), and thermal excitation ($k_B T$). The prefactor in *Equation 13* defines the rate at which an antigen would diffuse from a binding site lacking affinity for the antigen (i.e. without a potential well trapping the antigen in a bound state). Parameters will depend upon temperature, buffer composition, and mixture constituents. QCR introduced oscillations influence mass transport, bound-state parameters, and the average thermal fluctuation magnitude. Hence, we report only k_{off} values (note that $k_{off} = 1/\tau_{off}$). When the fluid velocity generated by the resonator exceeds the diffusive velocity, protein is no longer diffusing, but rather transported by forced convection. Hence, transport from a binding site is no longer diffusion limited.

Convection—Diffusion & Surface Volume Reactions

In addressing the fluid mechanics and chemical kinetics present for the surface—volume reaction represented in *Figures 2 & 5*, Edwards discusses four distinct timescales (convection, diffusion near the wall, diffusion into the binding surface, and reaction at the binding surface). Shear flow generated by the resonator alters each timescale by moving protein and fluid with an average velocity higher than the root-mean-squared diffusive velocity, increasing transport in the binding region, and shifting equilibria for receptor-ligand interactions (*see Table 6 for average protein and water diffusion rates and Table 7 for peak instantaneous velocities, peak surface deformation amplitudes, and peak loading rates generated by quartz crystal resonators*).

In *Figures 2(f) & 5(c)*, the 0 W data for BSA release and IgG/PA release upon pH change, respectively, are not fit perfectly by an exponential decay in the initial few seconds. This occurs because the assumption of small Damköhler (Da) number breaks down (*See Edwards for a detailed discussion [33]*). Qualitatively, the flow velocity near the wall is slow, yet the release kinetics are fast. Hence, for the first few seconds, while the fluorescently tagged protein is diffusing from the diffusion-limited solid-liquid interface, the intensity does not decay exponentially. Fortunately, resonator activation improves mass transport in the diffusion-limited boundary layer, and, hence, curves with resonator power input are fit well by a single exponential decay.

VI. CONCLUSION

Our hypothesis, desorption rate could be optimized to yield improved specific and nonspecific species separation, is supported by data in *Figures 2 & 5*. With immunoassay miniaturization and fluid-based microsystem development having clear

benefit from a sample size, speed, and reagent consumption perspective, yet troubling from a separation perspective, as noted by Kricka & Wild [5], we anticipate this method will find utility in immunoassay, molecular diagnostic, and lab chip applications.

The diffusion-limited boundary layer routinely complicates surface plasmon resonance assays and electrochemical measurements. Integrating ultrasonic transducers with such systems may prove useful in molecular screening and diffusion limited fuel-cell applications [34]. Additionally, nanoscale oscillations altering system equilibrium may prove useful for separations such as HPLC, or affinity chromatography applications.

APPENDIX

Table 3.6. RMS average diffusive displacement per second for protein in water and the self-diffusion of water molecules at 25 °C (*Reference 35 & 36 respectively*). Root-mean-square velocity computed using solution in *Reference 37*.

	RMS average diffusive displacement (μm/sec)
Protein (IgG – MW = 155,000)	15
Water	117

Convective Transport—Near Field Fluid Velocity Profile

The experimental set-up is influenced by two energy inputs (pressure driven flow and quartz crystal resonator activation).

$$v_x(z,t) = v_{pressure} + v_{resonator} \quad \textbf{(14)}$$

Both inputs transport the fluid, the first symmetrically, the second asymmetrically (with respect to coordinate *z*, which defines the channel height), with energy localized to the first few microns above the solid-support. More explicitly,

$$v_{resonator} = \frac{6U}{H^2}[Hz - z^2] + v_{resonator}^{\max} \exp[(i-1)\sqrt{\frac{\omega}{2\eta}}z]\exp(-i\omega t) \quad \textbf{(15)}$$

Table 3.7. Experimentally Measured Input Power Levels and calculated applied voltages, deformation amplitudes, peak instantaneous velocities at the resonator surface, and peak loading rates on surface immobilized protein molecules *[38,39]*.

Input Power (mW)	Voltage	Deformation Amp	Peak Fluid Velocity	Peak Protein Loading Rate
25 mW	18 mV	1 Å	500 μm/sec	5.5×10^4 pN/sec
50 mW	30 mV	2 Å	1000 μm/sec	9.5×10^4 pN/sec
100 mW	41 mV	3 Å	1300 μm/sec	1.3×10^5 pN/sec
400 mW	85 mV	5 Å	2800 μm/sec	2.3×10^5 pN/sec
850 mW	123 mV	8 Å	4000 μm/sec	3.8×10^5 pN/sec

REFERENCES

[1] Price, C.P. *Clinical Chemistry,* **1998**, vol. 44(10), 2071-2074.

[2] Ekins, R.P. *Clinical Chemistry*, **1998**, vol. 44(9), 2015-2030.

[3] May, M. *Genomics & Proteomics*, March **2004**.

[4] Hitt, E. *Genomics & Proteomics*, October **2003**.

[5] Kricka, L.J. & Wild, D. *The Immunoassay Handbook*, Third Edition, David Wild Ed., ELSEVIER Ltd.: Oxford, **2005,** 298-299.

[6] Roberts, C. *et al*., *JACS*, **1998**, 120, 6548-6555.

[7] Ruiz-Taylor, L.A *et al. PNAS*, January 30, **2001**, vol. 98, no. 3, 852-857.

[8] Fang, F., Satulovsky, J., & Szleifer I., *Biophysical Journal*, vol. 89, September **2005,** 1516-1533.

[9] Wazawa, T et al. Analytical Chemistry, 2006, 78, 2549-2556.

[10] Shengfu, C., Lingyun, L., & Shaoyi J. Langmuir, 2006, 22, 2418-2421.

[11] Steukers, M. et al., J. Immunological Methods, 20 March 2006, vol. 310, iss. 1-2, 126-135.

[12] Rathanaswami, P. et al., Biochemical & Biophysical Research Communications, 334, 2005, 1004-1013.

[13] Gribbon, P. & Sewing, A. *Drug Discovery Today*, **8**(22): 1035-1043.

[14] Huber, W. *J Molecular Recognition*, **2005**, 18: 273-281.

[15] Sinha, N., Mohan, S., Lipschultz, C., & Smith-Gill, S.J. *Biophysical Journal*, vol. 83, Dec. **2002**, 2946-2968.

[16] Blank, K. *et al.*, *PNAS*, 30 September **2003**, vol. 100, no. 120, 11356-11360.

[17] Evans, E. *Faraday Discuss*., **1998**, 111, 1-16.

[18] Leckband, D. *Annu. Rev. Biophys. Biomol. Struct.*, **2000**, 29:1-26.

[19] Myska, D.G. *Curr. Opin. Biotechnol.*, **1997**, 8, 50-57.

[20] Myska, D.G. *J. Molecular. Recogntion*, **1999** 12, 279-284.

[21] Meyer, G.D., Morán-Mirabal, J.M., Branch, D.W., and Craighead, H.G., *IEEE Sensors Journal*, vol. 6, no. 2, April 2006.

[22] Kessler, L.W. & Dunn, F., *J. Phys. Chem*, December **1969**, 73(12), 4256-4263.

[23] Grimshaw, D., Heywood, P.J., & Wyn-Jones, E. *J. Chem. Soc. Faraday Trans. II*, **1973**, 69, 756-762.

[24] Kremkau, F.W. & Cowgill, R.W. *J. Acoust. Soc. Am.*, November **1984**, 76(5), 1330-1335.

[25] Kremkau, F.W. & Cowgill, R.W. *J. Acoust. Soc. Am.*, March **1985**, 77(3), 1217-1221.

[26] Kremkau, F.W. *J. Acoust. Soc. Am.*, June **1988**, 83(6), 2410-2415.

[27] Choi, P.K., Bae, J.R., & Takagi, K. *J. Acoust. Soc. Am.*, February **1990**, 87(2), 874-881.

[28] Evans, E. *Faraday Discuss.*, **1998**, 111, 1-16.

[29] Merkel, R. *et al*. *Nature*, 7 January **1999**, vol. 397, 50-53.

[30] Evans, E. *Annu. Rev. Biophys. Biomol. Struct.*, **2001**, 30:105-128.

[31] Evans, E. & Calderwood, D.A., *Science*, 25 May **2007**, vol 316, 1148-1152.

[32] Fersht, A. *Structure & Mechanism in Protein Science: A Guide to Enzyme Catalysis & Protein Profiling*, **1998**, W. H. Freeman & Company: New York.

[33] Edwards, D. A. *IMA Journal of Applied Mathematics*, August **1999**, 63(1), 89-112.

[34] Yoon, S.K. , Fichtl, G. W. & Kenis, P.J.A., *Lab Chip*, **6**, 1516-1524, 2006.

[35] Jossang, T., Feder, J., & Rosenqvist, E., *J. of Protein Chem*, vol 7, no. 2, 1988.

[36] Mills, R., *J. Phys. Chem.*, vol 77, no. 5, 1973.

[37] Pathria, R.K., *Statistical Mechanics*, Second Edition, **1996**, Butterworth-Heinemann, Woburn, Ma.

[38] Kanazawa, K., *Faraday Discuss*. **107**, 77 (1997).

[39] Borovsky, B., Mason, B.L., & Krim, J., *J. Applied Physics*, vol. 88, no. 7, 1 October 2000, 4017-4021.

CHAPTER FOUR

Nonspecifically Bound Protein Removal from a Microfluidic Channel with an Integrated Surface Acoustic Wave Device

Don M. Aubrecht, Grant Meyer, & Harold G. Craighead

Cornell University, School of Applied Physics, Clark Hall, Ithaca, New York 14853

ABSTRACT

Protein adsorption to micro/nanoscale devices, commonly termed nonspecific binding or fouling, can block fluid channels, inhibit sensor function, and decrease signal-to-background ratios in analytical systems. We detail nonspecifically bound protein removal from a microchannel integrated with a surface acoustic wave device. Fluorescently tagged bovine serum albumin was used as a model protein given its high concentration in blood and propensity to bind nonspecifically. The average albumin release constant was increased by one order of magnitude with 250 microwatts delivered to the fluid volume and yielding a 97% reduction in fluorescent intensity in strongly excited microchannel regions. Accelerated desorption results from the localized generation of acoustic waves. Averaged over 1 min with a 3 μL/min flow rate, the temperature change in the fluid volume did not exceed 1.2 +/- 1°C. Calculations indicate 5 cm/sec peak fluid velocities are achievable at the solid—liquid interface, indicating advective fluid velocities near the interface exceed average diffusive values. High fluid velocities are achieved without additional reagent

introduction or buffer pH alteration. Achieving comparable microchannel velocities nanometers from the device surface with pressure driven flow requires a 3.3 mL/min volumetric flow rate—a large volumetric flow-rate requiring significant pressure generation. Achieving comparable electroosmotic flow velocities requires 2,500-15,000 V—a difficult potential to generate or switch quickly. Controlled cell, particle, and molecule release are routine analytical demands which prove challenging on-chip. Surface acoustic wave device integration is a potential solution.

I. INTRODUCTION

Surface acoustic wave (SAW) device development has focused on chemical sensing applications [1, 2]. Recently, SAW devices have been modified for fluid sensing and transport applications including microfluidic mixing [3, 4]. DNA and protein microarray integration with ultrasonic devices improves signal-to-background ratios, pattern uniformity, reduces hybridization times, and removes nonspecific binding [5-7]. Recent works details nonspecifically bound protein removal from implantable biosensors to reduce fouling [8].

The literature details laminar flow-based methods successful in removing microparticles from surfaces [9, 10]. This method, alternatively, generates high fluid velocities in small fluid volumes by converting an electrical signal into resonant mechanical motion. Resonant motion advects fluid near the device surface and generates acoustic streaming (i.e. steady streaming) in the fluid volume resting upon the SAW device beyond the Stokes' layer [11]. As stated by Mulvaney *et al*., laminar flow-based force discrimination with nanoscale particles is impractical at any practical microfluidic flow rate [10]. In this work, bovine serum albumin (BSA), with a hydrodynamic radius of ~5nm, is rapidly released with surface acoustic waves.

This work adds to previous literature by demonstrating and measuring accelerated protein desorption kinetics as a function of input power. Protein release events are

stochastic (i.e. the result of random fluctuations). As a result we measure the average release rate characterized by the release rate constant k_{off}.

Figure 1(a) depicts a device layout viewed from the top. Microfluidic channels provide well-defined fluid volumes localizing analyte near the transducer where acoustic wave energy dissipates into the fluid. Surface acoustic wave energy dissipates into the microchannel volume as drawn in *Figure 1(b)*. The frames in *Figure 1(c,d)* detail channel wall materials, protein adsorption, acoustic wave energy input from right and left, and average release rates which depend upon channel material.

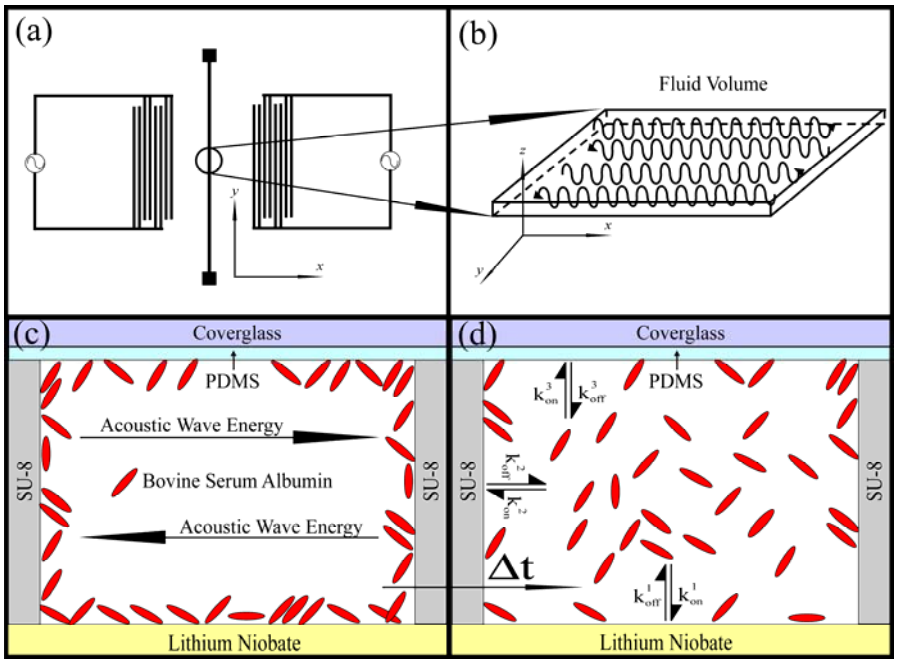

Figure 4.1. **(a)** Device layout and microchannel orientation. **(b)** Wave propagation through the fluid volume encapsulated by the microchannel. Phonons generated in the piezoelectric crystal dissipate kinetic energy into the viscous fluid volume. The energy distribution can be controlled in all three spatial coordinates and time. **(c)** Microchannel cross-section delineating channel materials, protein adsorption to each material, and acoustic wave energy impinging from left and right surface acoustic wave transducers **(d)** Microchannel cross-section detailing multiple kinetic release constants. Each material binds and releases protein with average binding and release values. Protein release rates are modulated with surface acoustic wave input power.

With appropriate photolithographic patterning, transducer design, and electronic equipment, the velocity and energy distributions in the fluidic channel can be controlled in each spatial dimension and in time.

$$v = v(x, y, z, t) \quad \textbf{(1)}$$

$$\Rightarrow E = \frac{1}{2}\int \rho v^2 dV = E(x, y, z, t) \quad \textbf{(2)}$$

The peak velocity generated at the fluid-SAW device boundary (ωA) with a deformation amplitude of 0.5 nm and frequency of 100 MHz is 5 cm/sec [12]. The three dimensional flow profile resulting from resonator activation is complex [13].

A fundamental problem often ignored in the microfluidics and sensing literature is nonspecific binding. It is either addressed as a systematic error or ignored with the assumption of disposability. Sensor designs introduce nanoparticles, polymer monoliths, and complex three-dimensional structures with large surface areas binding proteins nonspecifically. Such material heterogeneities complicate chemical passivation. Further, it is assumed, incorrectly, chemical passivation will eliminate nonspecific binding. Rather, a correct understanding includes protein concentrations and adsorption/desorption kinetics. The question, couched appropriately, becomes, "On what timescale and to what degree is nonspecific binding problematic for this assay?"

Many assays are conveniently performed at room temperature (~25 °C), while most human biochemistry occurs at ~37 °C. The Boltzmann constant-temperature product ($k_B T$) is the energetic input driving biological reactions. Many short-lived bound states become thermodynamically favorable, and relatively long-lived, at lower temperature. Efficiently eluting weakly bound material blocking channels, fouling

sensor surfaces, and increasing background levels, is often experimentally challenging.

Numerous publications detail chemical remedies reducing nonspecific binding. Common methods include channel passivation with poly(ethyleneglycol) (PEG) and newer, reportedly more stable, phosphorylcholine chemistries [14-17]. While chemical methodologies can modify nonspecific binding kinetics favorably, we stress the time and concentration dependencies. Time critical experiments require additional remediation methods combining chemical improvement with active, accelerated removal when high sample background levels exist. An extensive study by Fang *et al.* details protein chemical kinetic dependencies upon surface-grafted polymer chain-length, protein molecular weight, temperature, and graft density [17]. The authors state nonspecific binding will occur under any passivation conditions. It is just a matter of time.

Kessler & Dunn discuss acoustic wave propagation in a fluid causing time-varying, localized changes in pressure, density, and temperature. Acoustic wave energy absorption alters molecular energy level distributions. Wave motion perturbs molecular equilibria at rates which depend on the sound frequency [18, 19]. We hypothesized surface acoustic waves generated by a piezoelectric transducer could increase the bound-to-free transition probability for protein adsorbed to inorganic surfaces without markedly increasing temperature or shifting pH.

This on-chip fluid transport method is notable because: **(1)** It is simple, and may eliminate reagents, which expire and introduce variation with storage time, lot number, UV exposure, and environmental exposure. **(2)** SAW devices have been developed extensively for sensing applications. It is reasonable to consider microsystems providing sensing capability at low-power and improved transport and surface regeneration function at higher-power. **(3)** Fabrication is simple, requiring

basic photolithography and metal deposition. **(4)** Lithium niobate ($LiNbO_3$) chemistry is similar to traditional SiO_2 chemistries introducing affinity separation and release capability with affinity probe immobilization. **(5)** Procedures in microfluidic systems can be performed under no-flow conditions (volumetric flow rate $\boldsymbol{Q} = 0$). This eliminates analyte dilution and reagent volume consumption. **(6)** Devices are easily scaled in dimension/number, individually excitable, and electrical pulse characteristics can be controlled to minimize heating. **(7)** The acoustic penetration depth into the fluid is controlled *via* frequency—controlling the energy density spatially within the microchannel. **(8)** Integration with existing semiconductor processes may be possible using piezo-active aluminum nitride films, though a reduced mechanical coupling coefficient may limit utility if low power consumption is important. **(9)** Active device applications will be required in situations where disposable devices are impractical and surface regeneration required (e.g. remote environment placement where maintenance or replacement is inconvenient). **(10)** Achieving high fluid velocities on-chip is realizable under real-world constraints. Pressure driven flow requires a high volumetric flow rate (~3.3 mL/min). Electroosmotic flow requires high voltage (2,500-15,000 V) (*See Appendix for detail*).

An area where devices may find particular utility is protein preconcentration. Preconcentration is a common step performed when dealing with dilute analytes [20]. Protein capture may be specific, requiring affinity probes, or nonspecific, employing hydrophobic surface chemistries. Acoustic activation may prove useful in capturing and rapidly eluting protein strongly bound to a surface without pH change or marked temperature increase.

II. METHODS & MATERIALS

To test our hypothesis and demonstrate integration with traditional photolithographic processes and materials, we fabricated SAW devices on 128° YX lithium niobate ($LiNbO_3$) wafers obtained from Crystal Technology, Inc. Standard photolithography followed by 10 nm chromium and 90 nm gold evaporation steps was used to produce interdigital transducers. Devices were diced and individually photopatterned with SU-8 2010. *Figure 2(a)* is a device photograph showing an isolated number of interdigital electrodes (IDTs), and *Figure 2(b)* a device photograph with an integrated microchannel viewed from the top. A photodefined 100 micron channel (drawn as a black dotted line) [21] was capped using a coverslip spin coated with poly(dimethysiloxane) (PDMS) at 4000 rpm. The coverglass/PDMS cap was then pressed against the SU-8 channel to form a sealed channel. PDMS was exposed to an oxygen plasma at the high power setting for 1 minute with air as the process gas (Harrick Plasma).

The dimension *d* defines the SAW device center frequency. With a dual split-finger geometry, the center frequency (ν_{center}) = 8d. Devices were designed to operate at ~100 MHz. For nonspecific binding removal experiments using fully packaged devices, 95 MHz was found to be the frequency with lowest insertion loss, as measured with a spectrum analyzer. Devices were driven at 95 MHz, a span 10 kHz, and a 5 second sweep time.

Figure 2(c) is a photograph detailing the board layout and SAW device placement in the fixture. *Figure 2(d)* is an edge-on view with the device sealed and fixture pressure applied *via* screws.

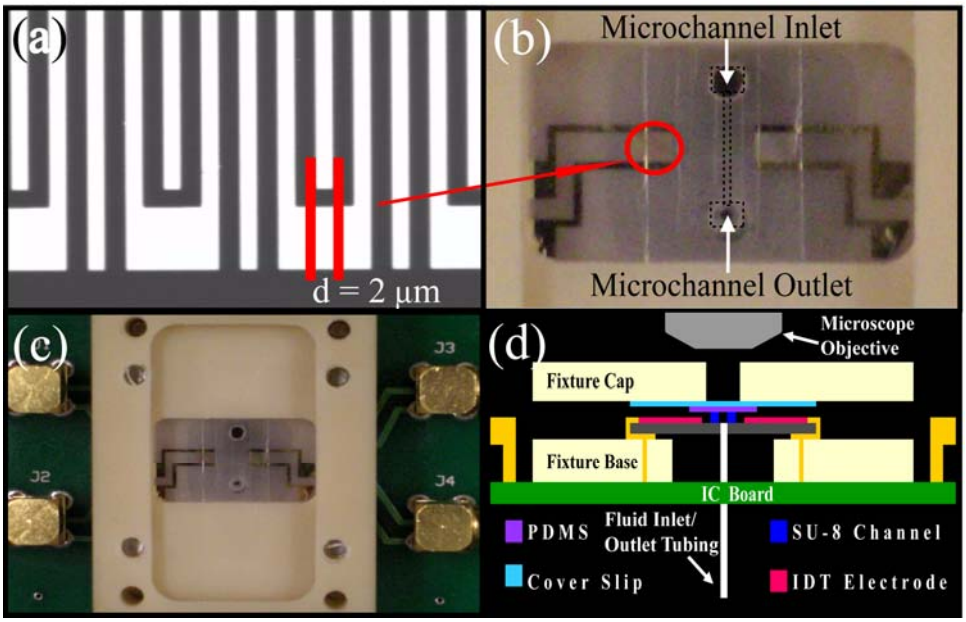

Figure 4.2. SAW device interdigital transducer geometry, packaging, and experimental set-up schematic. (a) Dual split-finger interdigital electrode geometry. Finger width defines center frequency. **(b)** Diced lithium niobate device measuring 21 x 14 mm. Microchannel placement outlined as black dotted-line to indicate position and shape. **(c)** Top-view photograph detailing IC board and device placement. **(d)** Packaged device illustration (View: edge-on) depicts electrical and fluidic connections from nonpatterned wafer side and optical microchannel imaging access from top.

Fluid channels were coupled through the chip by gluing silicone tubing to holes sandblasted through the lithium niobate after dicing and SU-8 photopatterning. The fluidically and electronically integrated chip was packaged by machining an insulating plastic (Delrin) fixture to accept pogo pins. Wrap-around electrodes were added with silver paint to connect bond pads to pogo-pins. A power-splitter was used to apply a voltage to both transducers.

Microchannels fabricated with PDMS and SU-8 were tested to determine power dissipation into microchannel materials. Frequency sweeps with and without channel materials are plotted in *Figure 3*.

The difference in attenuation is clearly demonstrated by insertion loss values of 35 dBm for an SU-8 microchannel and >60 dB for a PDMS microchannel at 95 MHz. The insertion loss for a device with no channel was 25 dBm at 95 MHz. Further

optimization with unidirectional transducers would improve channel excitation efficiency.

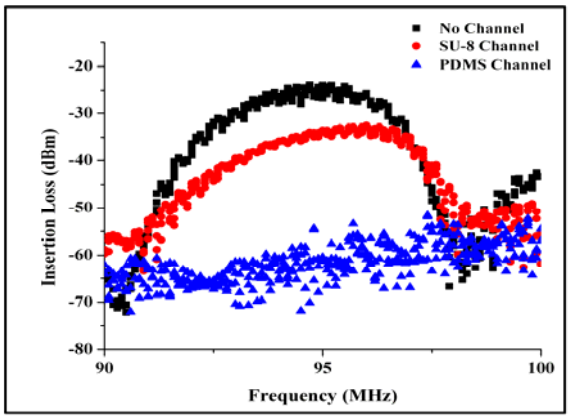

Figure 4.3. SAW device insertion loss without a channel (squares), with a sealed SU-8 channel (circles), and with a PDMS microchannel (triangles).

Insertion loss measurements for SU-8 and PDMS demonstrate the large disparity in wave velocity. The wave velocity in PDMS is significantly lower than in SU-8, causing a > 60 dBm insertion loss. Hence, SU-8 channels were used for experiments.

III. RESULTS

A 10X PBS buffer solution containing 55 μg/mL BSA fluorescently tagged with AlexaFluor 594 was passed through packaged microchannels for 1 min at 3 μL/min. This concentration is approximately three orders of magnitude *lower* than plasma concentrations, which has albumin concentrations ranging from 30-54 mg/mL. Pure buffer was driven through the channel until unadsorbed BSA was purged. After purge, the fluorescent intensity decay was quantified over 10 minutes. A shutter was used to block excitation between image capture frames.

Each frame was cropped and averaged over 500 ± 100 pixels to isolate the channel pixels and quantify fluorescent intensity *vs.* time. In *Figure 4(a)* the microchannel was imaged after BSA incubation and buffer purge. *Figure 4(b)* is an image captured

at experiment end. Fluorescent intensity images were incrementally captured at 30 second intervals. Significant removal occurred in ~2 minutes with 97 +/- 3% removal in highly excited microchannel regions for a device driven at 95 MHz with 250 μW reaching the fluid volume and a 3 μL/min buffer flow rate. Power dependent elution results are quantified in *Figure 4(c)*.

Removal had a periodic spatial dependence pictured in Figure *4(b)*. A standing wave is generated in the channel resulting from complex diffraction patterns generated by microchannel incorporation. Protein removal at anti-nodes, caused by a standing-wave in the microchannel, is reduced. This indicates a non-uniform fluid velocity in the microchannel. Importantly, this result indicates the removal mechanism is hydrodynamically influenced.

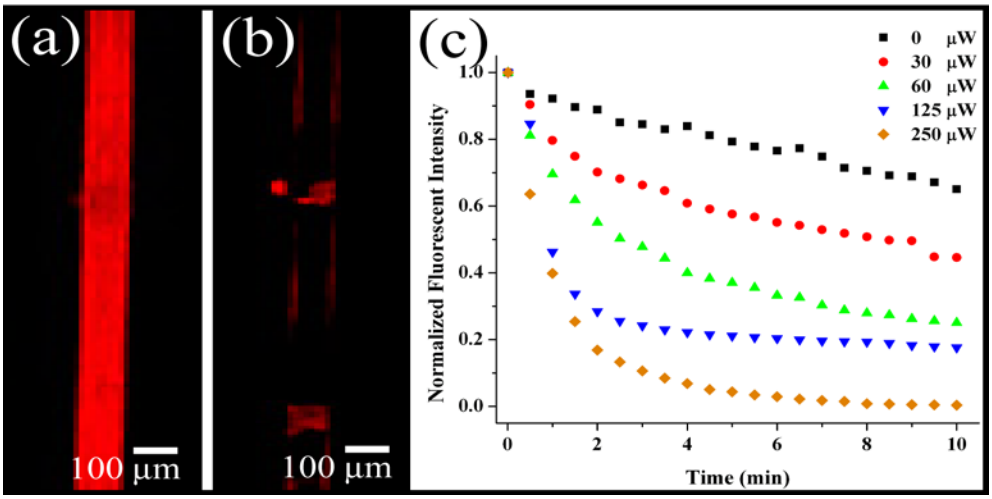

Figure 4.4. SAW Activation Fluorescence Microscopy Results (a) AlexaFluor 594 labeled BSA bound to an SU-8 microchannel after buffer wash step. **(b)** Fluorescent image after surface acoustic wave excitation for 10 minutes. Intensity is highest at standing wave anti-nodes, where the surface acoustic wave streaming velocity is lowest, indicating release is hydrodynamically influenced. **(c)** Fluorescent intensity *vs.* time for BSA release with incrementally increasing power delivered to the fluid volume. Protein elution rate increases with increasing input power.

Although complex chemical kinetics and flow patterns occur in the microchannel, we can measure release kinetics. Written chemically, protein adsorption/desorption reactions can be written as,

$$A + B \underset{k_{off}}{\overset{k_{on}}{\rightleftharpoons}} C \quad \textbf{(3)}$$

Protein (B) binds to surface atoms (A) with characteristic rate constants k_{on} and k_{off} characterizing protein adsorption and desorption. The time-dependent quantity of interest is the number of proteins interacting with the substrate to form a protein—substrate complex *C*. Bound protein quantities will depend upon the number of available surface binding sites and protein concentration. Kinetic models are detailed by Lauffenberger & Linderman [22]. Written in differential form, *Equation 3* becomes,

$$\frac{dC}{dt} = k_{on} AB - k_{off} C \quad \textbf{(4)}$$

In this work we characterize,

$$C \xrightarrow{k_{off}} A + B \quad \textbf{(5)}$$

This equation holds if $k_{on}AB = 0$. This assumption is valid if rapid transport away from the surface upon release makes B, the free protein concentration, zero. Given the high fluid velocities generated by SAW devices and constant pure buffer infusion, this assumption is reasonable. *Equation 5* reduces to a simple differential equation given in *Equation 6*.

$$\frac{dC}{dt} = -k_{off} C \quad \textbf{(6)}$$

We quantify the power-dependent change in $k_{off} = k_{off}(P)$, where P is the power input by the SAW transducers. Acoustic oscillations alter system equilibrium (i.e. SAW introduced oscillations shift k_{on} and k_{off}) [18, 19]. Increasing input power increases oscillation amplitude.

Systems with advective and diffusive mass transport decoupled from surface reaction kinetics are commonly modeled with the following differential equation, which assumes multiple release rate constants,

$$\frac{dC}{dt} = -k_0 C_0 - k_1 C_1 - k_2 C_2 - \ldots \quad \textbf{(7)}$$

$$C(t=0) = C_0 + C_1 + C_2 + \ldots \quad \textbf{(8)}$$

In *Equations 7*, *C*, the total protein—substrate complex number, is fragmented to explicitly account for multiple binding affinities (i.e. multiple k_{off} release rates). Solving this differential equation, where $k_{0,1,2\ldots}$ are the release rate constants with the initial condition given in *Equation 8* gives,

$$C(t) = C_0 \exp(-k_0 t) + C_1 \exp(-k_1 t) + C_2 \exp(-k_2 t) + \ldots \quad \textbf{(9)}$$

In our experiments, *C* is proportional to the fluorescent signal intensity, and, therefore, we write,

$$I(t) = I_0 \exp(-t/\tau_0) + I_1 \exp(-t/\tau_1) + I_2 \exp(-t/\tau_2) + \ldots \quad \textbf{(10)}$$

Where

$$k_{0,1,2,\ldots} = \frac{1}{\tau_{0,1,2,\ldots}} \quad \textbf{(11)}$$

In instances where a protein sub-population has a slow kinetic release constant (relative to the experimental time-scale) we can treat the system as an exponential

decay with an additional constant quantifying the strongly bound sub-population. In the respective limits,

$$\tau_{1,2,\ldots} \rightarrow \infty \quad \textbf{(12)}$$

$$I(t) = I_0 \exp(-t/\tau_0) + I_1 \quad \textbf{(13)}$$

$$I(t) = I_0 \exp(-t/\tau_0) + I_1 \exp(-t/\tau_1) + I_2 \quad \textbf{(14)}$$

Equations 13 and 14 were used to fit intensity data in *Figure 4*. Decay time and rate constant ($\tau_{0,1}$ and $k_{1,2}$) values are listed in *Tables 2 and 3*. Fitting data to *Equations 13 and 14* provides information about protein—substrate release time constants and bound population proportions. By increasing the input power reaching the SAW device, we can quantify the influence device input power has on protein desorption.

First Order Exponential Fit Data – $I(t) = I_0 \exp(-t/\tau_0) + I_1$

Equation 13 gives the exponential fit used to reduce the intensity decay results obtained in the experiment to three fit parameters.

Table 4.1. First Order Exponential Decay Fit Data – $I(t) = I_0 \exp(-t/\tau_0) + I_1$

	I_0	τ_0 (min)	I_1	R^2	k_{off} (sec^{-1})
0 μW	0.67 +/- 0.20	16.53 +/- 6.67	0.29 +/- 0.20	0.981	1.0×10^{-3}
30 μW	0.51 +/- 0.02	3.15 +/- 0.31	0.46 +/- 0.02	0.980	5.3×10^{-3}
60 μW	0.70 +/- 0.02	2.44 +/- 0.14	0.25 +/- 0.01	0.992	6.8×10^{-3}
125 μW	0.86 +/- 0.04	1.01 +/- 0.09	0.19 +/- 0.01	0.972	1.7×10^{-2}
250 μW	0.97 +/- 0.01	1.10 +/- 0.03	0.02 +/- 0.01	0.997	1.5×10^{-2}

Second Order Exponential Decay Fit Data – $I(t) = I_0 \exp(-t/\tau_0) + I_1 \exp(-t/\tau_1) + I_2$

A simple exponential decay fits the first four intensity curves well (i.e. fitting with a second order decay yields redundant or experimentally unreasonable values). However, the last curve-fit improves with a second order decay. The value for τ_1 indicates some BSA is strongly bound and elutes slowly compared to protein releasing with the decay constant τ_0. The slowly eluting protein is thought to elute from highly hydrophobic SU-8 walls, the PDMS cap and anti-nodes where the fluid velocity is low. *Equation 14* was used to fit the 250 μW curve.

Table 4.2. Second Order Exponential Decay Fit Data – $I(t) = I_0 \exp(-t/\tau_0) + \ldots$ $\ldots I_1 \exp(-t/\tau_1) + I_2$

	I_0	τ_0 (min)	I_1	τ_1 (min)	I_2	R^2	$k^{1,2}_{off}$ (sec^{-1})
250 μW	0.87 +/- 0.04	0.92 +/- 0.04	0.15 +/- 0.02	6.86 +/- 0.53	-0.03 +/-0.04	0.9995	1.8×10^{-2} 2.4×10^{-3}

IV. DISCUSSION

Protein release from a bound state depends upon temperature, energy-well properties, and mass transport at the interface. The temperature change can be calculated from *Equation 15*,

$$\Delta T = \Delta E / mC \qquad \textbf{(15)}$$

Where ΔT is the temperature change, ΔE is the energy input, m is the fluid volume mass and C is the heat capacity of the fluid. A figure of merit routinely used in chemical kinetics is a doubling in rate constant value with a 10°C increase in temperature [23]. Assuming full dissipation of attenuated power into heat, the temperature was calculated to rise no more than 1.2 +/- 1 °C if averaged over 1 minute with 250 μW delivered to the fluid volume of 3 μL. This temperature change

increases the thermal energy in the system, ultimately increasing the protein desorption rate. While clearly influencing the protein release rate, this temperature does not account for the order of magnitude increase. Accelerated release arises from both a temperature change and hydrodynamic induced bound-to-free transitions. Extensive work by many theoreticians has detailed complex nonequilibrium statistical mechanics and protein subdiffusion which contribute to protein binding and release [24-32].

V. CONCLUSION

Rapid protein elution and mixing without pressure driven or electrokinetic flow is achievable only with an active device. This method has utility in preconcentration and controlled release applications (e.g. affinity probe screening, mass spectrometry, and biosensors). Results demonstrate power-dependent nonspecific binding removal. Broader applicability to systems where ultrasonic manipulation can disrupt particle—substrate interactions may exist (e.g. cell manipulation, bead-based sorting, and sensing). Numerous literature articles site the integration of superparamagnetic beads, nanoparticles, quantum dots, and cells with micro/nanofluidic systems where capture and release capabilities are critical.

APPENDIX

Fluid Transport Mechanisms

Fluids can be transported thermally and with pressure, electric fields, or acoustic waves [33, 36, 37, 38]. The respective equations for thermally generated RMS displacement per second, pressure driven flow, electroosmotic flow, and acoustically generated flow are given by *Equations 16-19.*

$$\sqrt{< r^2 >} = \sqrt{6Dt} \quad \textbf{(16)}$$

Understanding fluid transport in the microchannel requires knowledge of the fluid velocity. When considering fluid velocities in a microfluidic channel, diffusive values provide an average velocity metric. *Table 1* lists the average root-mean-square (RMS) protein displacement per second for protein (IgG – MW = 155,000) in water and water's self-diffusion constant.

Table 4.3. RMS diffusive displacement values for protein & water molecules at 25°C. (*References 34 & 35 respectively*). Root-mean-square velocities computed using solution in *Reference 33.*

	RMS Displacement per second (microns)
Protein (IgG – MW = 155,000)	15
Water	117

$$v_{pressure} = \frac{6U}{H^2}[Hz - z^2] \quad \textbf{(17)}$$

$$v_{electroosmotic} = \frac{-\varepsilon\zeta}{\eta}E = \frac{-\varepsilon\zeta}{\eta L}V \quad \textbf{(18)}$$

$$v_{resonator} = v_{resonator}^{\max} \exp[(i-1)\sqrt{\frac{\omega}{2\eta}}z]\exp(-i\omega t) \quad \textbf{(19)}$$

Experimental Fluid Velocity Profile

Fluid is transported in our system by pressure driven and SAW generated components.

$$v_x(z,t) = v_{pressure} + v_{resonator} \quad \textbf{(20)}$$

Pressure driven flow transports the fluid symmetrically about the channel cross-section, while SAW generated flow is asymmetric with respect to the *z*-coordinate defining the channel height. The SAW generated shear velocity fluid transport contribution in the near field limit (within the Stokes's layer) is given by *Equation 21*,

$$v_{resonator} = \frac{6U}{H^2}[Hz - z^2] + v_{resonator}^{\max} \exp[(i-1)\sqrt{\frac{\omega}{2\eta}}z]\exp(-i\omega t) \quad \textbf{(21)}$$

The coordinates are as depicted in *Figure 1*. *Table 4* lists symbols, symbol names, units, and values used in calculations where applicable.

Table 4.4. Symbols, symbol names, units, and relevant values.

Symbol	Symbol Name	Value	SI Units
r	Displacement	-	m
D	Diffusion Constant	Refs. 34,35	m^2/s
t	Time	-	s
U	Mean Flow Velocity	5000 μm/sec	m/s
H	Channel Height	100 μm	m
ε	Buffer Permittivity	4.4 x 10^{-10} $C^2/(N \cdot m^2)$	$C^2/(N \cdot m^2)$
ζ	Zeta Potential	-5 to -30 mV	V

Table 4.4 (continued)

η	Kinematic Viscosity (Water 25°C)	1×10^{-6} m^2/s	m^2/s
E	Electric Field	-	V/m
L	Channel Length	1 cm	m
V	Voltage	-	V
$v_{resonator}^{max} = \omega A$	Peak Velocity	5 cm/sec	m/s
ω	Frequency	100 MHz	1/s
A	Amplitude	0.5 nm	m

ACKNOWLEDGMENT

Work was supported by the Cornell LIFE Program. The authors wish to thank Rob Ilic for extensive and timely fabrication support performed in the Cornell Nanoscale Facility and John Mannion, Stephen Levy, and Prof. Watt W. Webb for useful electrokinetic and fluid mechanics discussions. We have also benefited from chemical kinetics discussions with Prof. David Manke.

REFERENCES

[1] J. Smith & V. Hinson-Smith, "The New Era of SAW Devices", *Analytical Chemistry*, 3505-3507, 1 June 2006.

[2] C.M. Harris, "Seeing SAW Potential", *Analytical Chemistry*, 355-358A, 1 August 2003.

[3] W.K. Tseng et al., "Active micro-mixers using surface acoustic waves on Y-cut 128° $LiNbO_3$", *J. Micromech. Microeng.*, 16(2006) 539-548.

[4] G.G. Yaralioglu, "Ultrasonic Mixing in Microfluidic Channels Using Integrated Transducers", *Anal. Chem.* 2004, 76, 3694-3698.

[5] A. Toegl, R. Kirchner, C. Gauer, & A. Wixforth, "Enhancing Results of Microarray Hybridizations Through Microagitation", *J. Biomolecular Techniques*, vol. 14, iss. 3, Sept 2003.

[6] M. Hartmann, A. Toegl, R. Kirchner, & M.F. Templin, "Increasing robustness and sensitivity of protein microarrays through microagitation and automation", *Analytica Chemica Acta*, 564 (2006), 66-73.

[7] Meyer, G.D., Morán-Mirabal, J.M., Branch, D.W., and Craighead, H.G., "Nonspecific Binding Removal From Protein Microarrays Using Thickness Shear Mode Resonators", *IEEE Sensors Journal*, vol. 6, no. 2, April 2006.

[8] PYJ. Yeh, "Electric field and vibration-assisted nanomolecule desorption and anti-biofouling for biosensor applications", *Colloids & Surfaces B-Biointerfaces*, 59(1): 67-73, 1 Sept. 2007.

[9] Y. Zhang, V.T. Milam, D.J. Graves, & D.A. Hammer, "Differential Adhesion of Microspheres Mediated by DNA Hybridization I: Experiment", *Biophysical Journal*, vol. 90, June 2006, 4128-4136.

[10] S.P. Mulvaney *et al.*, "Rapid, femtomolar bioassays in complex matrices combining microfluidics and magnetoelectronics", *Biosensors & Bioelectronics*, 23(2007) 191-200.

[11] L.D. Landau & E.M. Lifshitz, Fluid Mechanics, Second Edition, 1987, Butterworth-Heinemann, Linacre House, Jordan Hill, Oxford OX2 8DP.

[12] T. Uchida, T. Suzuki, & S. Shiokawa, "Investigation of Acoustic Streaming Excited by Surface Acoustic Waves", IEEE Ultrasonics Symposium, 1995, 1081-1084.

[13] Z. Guttenberg et al. "Flow profiling of a surface-acoustic-wave nanopump", Physical Review E, 70 (2004), 056311.

[14] D. Wu, B. Zhao, Z. Dai, J. Qin and B. Lin, "Grafting epoxy-modified hydrophilic polymers onto poly(dimethylsiloxane) microfluidic chip to resist nonspecific protein adsorption", Lab-on-a-Chip, 2006, 6, 942.

[15] C. Roberts, C.S. Chen, M. Mrksich, V. Martichonok, D. E. Ingber, & G.M. Whitesides, "Using Mixed Self-Assembled Monolayers Presenting RGD and $(EG)_3OH$ Groups To Characterize Long-Term Attachment of Bovine Capillary Endothelial Cells to Surfaces"**,** *J. Am. Chem. Soc.* 1998**,** *120,* 6548-6555.

[16] Y. Wang, M. Bachman, C. E. Sims, G. P. Li, & N. L. Allbritton, "Simple Photografting Method to Chemically Modify and Micropattern the Surface of SU-8 Photoresist", *Langmuir* 2006**,** *22*, 2719-2725.

[17] F. Fang, J. Satulovsky, & I. Szleifer, "Kinetics of Protein Adsorption and Desorption on Surfaces with Grafted Polymers", *Biophysical Journal*, vol. 89 Sept. 2005 1516–1533.

[18] L.W. Kessler & F. Dunn, "Ultrasonic Investigation of the Conformal Changes of Bovine Serum Albumin in Aqueous Solution", *J. Phys. Chem.*, vol. 73(12), Dec. 1969**,** 4256-4263.

[19] D. Grimshaw, P.J. Heywood, E. Wyn-Jones, "Proton Transfer in some Amino-acids Studied by the Ultrasonic Method", *Faraday II*, 1972, 756-762.

[20] D.L. Huber, R. P. Manginell, M. A. Samara, B.-Il Kim, B. Bunker, "Programmed Adsorption and Release of Proteins in a Microfluidic Device", *Science*, vol 301, 18 July 2003, 352-354.

[21] Francs, L.A., Friedt, J.-M., Bartic, C., Campitelli, A., "A SU-8 liquid cell for surface acoustic wave biosensors", 2004 Proc. SPIE 5455:353-363.

[22] Lauffenburger, D.A. and Linderman, J., *Receptors: Models for Binding, Trafficking, and Signaling*, 1993, Oxford University Press, Inc., New York.

[23] Personal communication with Dr. David Manke, May 2007.

[24] E. Evans , "Probing the Relation Between Force-Lifetime and Chemistry in Single Molecular Bonds". *Annu. Rev. Biophys. Biomol. Struct.* 30:105-128, 2001.

[25] R. Zwanzig, *Nonequilibrium Statistical Mechanics*, Oxford University Press, 2001.

[26] P. Hanggi, "Escape from a Metastable State", *Journal of Statistical Physics*, vol. 42, Nos. 1/2, 1986, 105-148.

[27] D. Chandler, "Roles of Classical Dynamics and Quantum Dynamics on Activated Processes Occurring in Liquids", *Journal of Statistical Physics*, vol. 42, Nos. 1/2, 1986, 49-67.

[28] W. Min & S. Xie, "Kramers model with a power-law friction kernel: Dispersed kinetics and dynamic disorder of biochemical reactions", *Phys. Rev. E* 73, 010902(R), 2006.

[29] N. Agmon & J.J. Hopfield, "Transient Kinetics of Chemical Reactions with Bounded Diffusion Perpendicular to the Reaction Coordinate: Intramolecular Processes with Slow Conformational Changes", *J. Chem. Phys.*, 78(11), 1 June 1983**,** 6947-6959.

[30] E. Z. Eisenmesser, D. A. Bosco, M. Akke, D. Kern, "Enzyme Dynamics During Catalysis", *Science*, vol 295, 22 February 2002, 1520-1523.

[31] G. Zaccai, "How soft is a protein? A Protein Dynamics Force Constant Measured by Neutron Scattering", *Science*, vol. 288, 2 June 2000, 1604-1607.

[32] S. Benkovic and S. Hammes-Schiffer, "A perspective on Enzyme Catalysis", *Science*, vol 301, 29 August 2003, 1196-1202.

[33] Pathria, R.K., Statistical Mechanics, Second Edition, 1996, Butterworth-Heinemann, Woburn, Ma.

[34] Jossang, T., Feder, J., & Rosenqvist, E., "Photon Correlation Spectroscopy of Human IgG", *J. of Protein Chem*, vol 7, no. 2, 1988.

[35] Mills, R., "Self-Diffusion in Normal and Heavy Water in the Range 1-45°", *J. Phys. Chem.*, **77,** 685 (1973).

[36] W. M. Deen, Analysis of Transport Phenomena, 1998, Oxford University Press.

[37] B. J. Kirby & E. F. Hasselbrink Jr., "Zeta potential of microfluidic substrates: 1. Theory, experimental techniques, and effects on separations", Electrophoresis, 2004, 25, 187-202.

[38] D. P. Telionis, Unsteady Viscous Flows, 1981, Springer –Verlag New York Inc.

CHAPTER FIVE

Nonspecific Cell Removal & Controlled Membrane Permeation with Surface Acoustic Wave Devices

Grant Meyer, José M. Morán-Mirabal, & Harold G. Craighead

Cornell University, School of Applied Physics, USA

ABSTRACT

In small fluid volumes mixing is difficult, diffusion is slow, and nonspecific adsorption is problematic. Surface acoustic wave devices generate high fluid velocities in small volumes. Noting diffusive limitations and nonspecific adhesion problems and a potential acoustic wave solution, we performed affinity-based cell separation and time-dependent membrane permeation experiments on surface acoustic wave devices. Flow velocity measurements were used to calculate the force applied to bound cells and demonstrate spatial mass transport control in microfluidic channels. Separation and permeation results obtained with fluorescence and scanning electron microscopy are presented. Affinity-based capture and nonspecifically bound cell removal results were obtained with green fluorescent E. *coli* binding to covalently immobilized antibodies. Red fluorescent S. *aureus* was used as nonspecific bacteria to demonstrate E. *coli* specificity. Devices incubated with red and green bacteria were imaged before and after surface acoustic wave device excitation. Fluorescent image analysis yielded 88% removal of nonspecifically bound E. *coli* bound to non-protein patterned areas, a 12% loss of E. *coli* bound to protein patterned areas, and 99% removal of

nonspecifically bound S. *aureus*. To measure membrane permeation as a function of time, adhered and suspended cells were exposed to acoustic waves incrementally from 0 to 240 seconds. Membrane permeation *vs.* time, assayed with lipid-insoluble fluorescent dye, demonstrated spatial and temporal membrane permeation dependencies. Maximal adhered cell membrane disruption occurred in 30 seconds, while suspended cell membrane permeation required 240 seconds. Solution exposure durations of 60 and 120 seconds permeated cell membranes allowing lipid-insoluble dye into the cytoplasm, yet cells remained viable post-permeation, as indicated by cell adhesion and spreading post-acoustic wave exposure. Results indicate devices may prove useful in gene transfection. DNA, RNA, protein, and cellular analyses routinely employ a membrane disruption step performed *via* chemical or mechanical means. Surface acoustic wave devices provide electrically controlled fluid manipulation, simple planar device geometry, and sensing capability, which may prove useful in bioassay automation applications.

I. INTRODUCTION

Heterogeneous biological samples contain numerous cell types, proteins, and environmental contaminants. As a result, complex biological fluid analyses require four key steps: (1) separation, (2) sample preparation/amplification (potentially involving thermal cycling or reagent introduction), (3) sample analysis (sensing/detection), and (4) data analysis. This work presents results addressing steps 1 and 2.

Cells in solution sediment without mixing (Sedimentation velocities as a function of particle diameter and density are plotted in the Appendix). After sedimentation, cells can attach strongly to substrates. Adhesion is sometimes desirable (i.e. culturing adherent cells), but, in diagnostic applications, nonspecific cell adhesion blocks fluidic

channels and sensor elements. Removal routinely requires significant force. Assuming the force applied to bound nano/microparticles is applied hydrodynamically, the force scales linearly with fluid velocity. Integrated transducers which improve fluid transport, expedite sample preparation steps, and provide sensing capability are important for bioassay automation and rapid analysis.

Affinity probe-based separations provide high affinity/specificity and rapid results (routinely tens of minutes) [1, 2]. Nanogram/mL analyte concentrations are routinely achievable in practice, however, theoretically, attomolar/zeptomolar sensitivities are achievable. Kinetic and mass transport limitations creating sub-optimal, real-world, limitations are discussed by Kuznezow [3-5]. Importantly, immunoassays are routinely used to detect proteins, hormones, or cytokines—all molecules with low molecular weight and high average diffusive velocities relative to cells.

Circulating tumor cell detection requires rare cell separation after cells shed into blood. A volume metric for high background biological sample analysis is circulating tumor cell isolation. Circulating tumor cells are shed by all major carcinomas into peripheral blood [6]. The volume used, 7.5 mL, represents a large volume to be sampled. Volumes used in Allard's experiments were spiked with an average of 319 endothelial cells to generate positive controls. Such values are important to consider for lab-on-a-chip device design. A 7.5 mL blood volume contains ~30-50 billion red blood cells. Simple math gives an optimistic signal-to-background ratio of $\sim 1 \times 10^{-8}$. Clearly, if intracellular analyses are required, separation prior to lysis is required. Improving mass transport in complex biological fluids, where diffusion is slow and sedimentation proves problematic, is critical. Cellular and macromolecular mass transport from solution to surfaces, including rapid protein adsorption relative to cell capture is discussed in *Reference 7.*

Nonspecific binding, sedimentation, contamination, and poor mass transport make fluid analysis steps 1 and 2 difficult. Difficulties can be mitigated by advection, which accelerates mixing. Achieving high fluid velocities in small volumes without analyte dilution is difficult. Our previous work discusses fabrication protocols, bioassay mass transport improvement, and nonspecific binding removal with ultrasonic devices [8-10]. In this work, nonspecific cell release and controlled membrane permeation results obtained with surface acoustic waves are detailed.

Surface acoustic wave devices are produced with standard semiconductor tools and routinely used in telecommunications and chemical/biological sensing [11, 12]. Because acoustic wave devices generate significant fluid velocities, localize energy injection to the solid-liquid interface, and are controlled electrically, we hypothesized SAW devices could separate cells based on affinity (separation) and controllably disrupt captured cell membranes based on acoustic wave exposure duration and proximity to the transducer (sample preparation). Numerous manuscripts detail ultrasound-based fluid mixing results [13-16]. We sought to build upon this literature to demonstrate biological separation and membrane permeation utility.

Device Layout

Experiments required convenient packaging for electrical connection, fluid localization, and optical interrogation. *Figure 1* presents the device electrode detail, fluid reservoir location relative to electrodes, supporting circuit board integration with a machined Lexan fixture, and device placement after assembly in the fixture

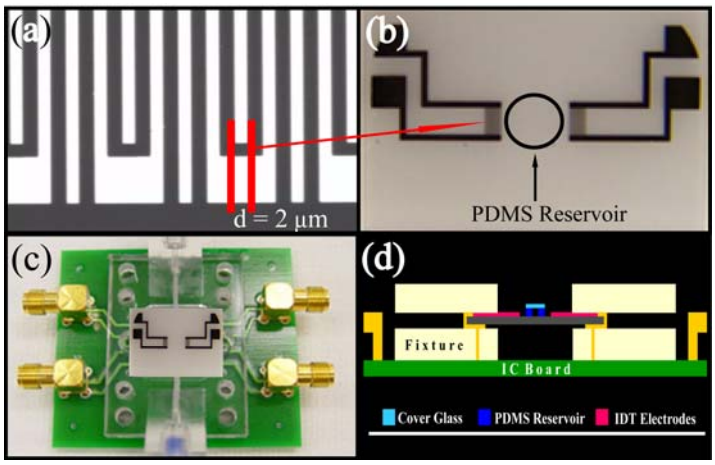

Figure 5.1. **(a)** Dual split-finger interdigital electrode geometry. Finger width defines center frequency (~100 MHz). **(b)** Diced lithium niobate device measuring 21 x 14 mm with PDMS reservoir placement marked in black. **(c)** Top view photograph detailing supporting circuit board and SAW device placement **(d)** Packaged device illustration (edge-on view) depicts electrical connections and fluid reservoir detail.

Protein patterning was used to demonstrate affinity-based cell capture and nonspecifically bound cell removal from unmodified substrate. Patterning on SAW substrates with a parylene-based masking process was used to define protein microspots and non protein patterned regions. With well-developed silane chemistry it is possible to covalently attach specific receptors on SAW substrates [17]. Pattern placement, a bright-field pattern image, and schematic (edge-on view) are shown in *Figure 2.*

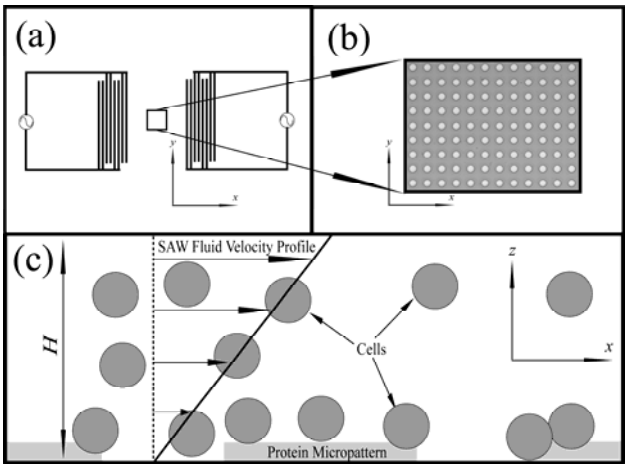

Figure 5.2. **(a)** SAW electrode diagram and micropattern image detailing SAW device layout with surface micropattern. **(b)** Bright-field micropattern image. **(c)** Fluid volume diagram (edge-on view) depicting cells binding to protein microspots and sedimentation (nonspecific adsorption). Cells sediment and physically block transducer/sensor surface.

II. RESULTS & DISCUSSION

A. Fluid Velocity Measurements & Particle Manipulation in Microfluidic Channels

Measuring the fluid velocity with microparticle velocimetry allows force calculation. At microwatt power levels delivered to the fluid it is possible to achieve velocities exceeding 2 cm/sec. Transducer design and fluid viscosity determine the velocity distribution within the channel. Activating an individual transducer can shift particle distributions from 3D to 2D or *vice versa*. Bead distributions before and after SAW excitation are shown in *Figure 3(a, c)*. A 2D velocity map co-planar to the SAW substrate is depicted in *Figure 3(b)* (Traveling waves impinge from a transducer patterned to the left of the microchannel).

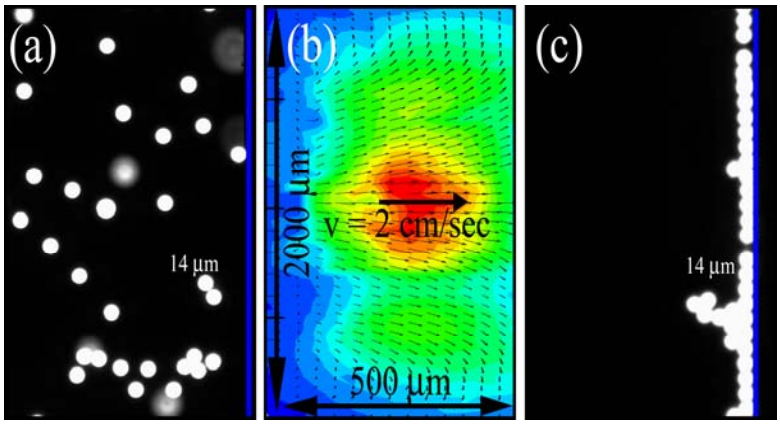

Figure 5.3. (a) Microchannel with 14 micron beads diffusing in buffer (blue line overlay marks microchannel wall location). (b) Microparticle velocimetry profile inside a microfluidic channel. Heat map indicates areas of highest velocity. Velocities measured in excess of 2 cm/sec in the red region. **(c)** Advection pushes beads to the channel wall.

B. Forces Acting on an Immobilized Sphere in Solution

In addition to adhesive forces, particles and cells adhering to a solid-support are acted upon by two forces—stochastic thermal fluctuations and hydrodynamic drag. The average force applied by thermally induced buffer collisions with cells exerts negligible force (pN) relative to hydrodynamic drag (nN). A physical force schematic (*Figure 4(a)*), force *vs.* cell diameter (*Figure 4(b)*), and an SEM image detailing an RBL mast cell cytoskeletal response to the applied hydrodynamic force are shown in *Figure 4(c).* *Figure 4(c)* images an RBL mast cell responding (binding) to a bovine serum albumin—dinitrophenyl (BSA-DNP) microspot. The cell creates a podosome in response to the stimulus (BSA-DNP). The hydrodynamic drag force pulls the cell away from the attachment area causing cytoskeletal rearrangement.

The hydrodynamic drag force calculated for a sphere immobilized upon a solid support [18] is,

$$F = 1.7(3\pi\mu Dv) \quad \textbf{(1)}$$

Where μ is the dynamic viscosity, D is the particle diameter, and **v** is the fluid velocity.

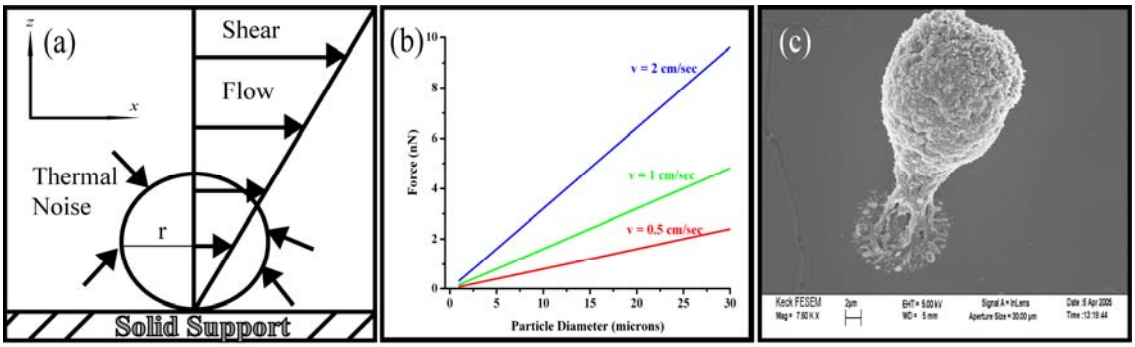

Figure 5.4. (a) Thermal fluctuations and shear flow exert forces on an immobilized sphere at an interface. (b) Calculated force on a spherical particle *vs.* particle diameter with v = 0.5, 1, and 2 cm/sec. (c) RBL Mast cell binding to a protein patterned microspot. Shear flow generated by surface acoustic wave dissipation into fluid resting upon the solid support applies a hydrodynamic force to cells. SEM image demonstrates cytoskeletal/membrane deformation resulting from the applied hydrodynamic force.

C. Selective Cell Capture & Membrane Permeation

Complex biological samples contain many cell types. Often information about the entire cell population is unnecessary. Rather, isolation and detailed analysis of one or a few cell types is desired. Splitting the cell population into two sets (signal and background), we can define a separation ratio. N_S represents signal at experiment start, N'_S represents signal at experiment end, and N_B defines background.

$$R = \frac{N_B + N_S}{N'_S} \quad \textbf{(2)}$$

We seek to drive N_B to zero while maximizing N'_S. Ideal separation would yield $N_S/N'_S = 1$, assuming no signal cells bound nonspecifically to the background region bind to protein microspots. This ratio was chosen to provide a metric accounting for background and signal cells removal with shear flow generated by SAW device activation. Schematic experiment representations, fluorescent images, and quantitative values derived from fluorescent images before and after SAW activation for 60 seconds at 250 microwatts are presented in *Figure 5* (Image analysis methods

are discussed in the Appendix). The values for ***R*** before and after SAW activation are 1.87 and 1.14 respectively.

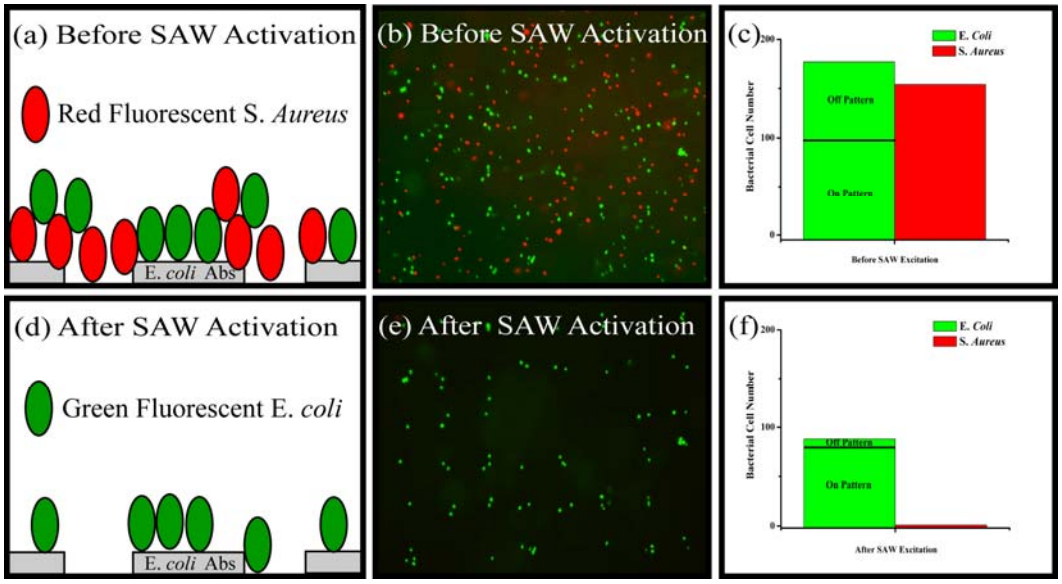

Figure 5.5. (a,b,c) Diagram, fluorescent image, and red/green bacteria counts for fluorescent image in *(b)* before SAW device activation. (d,e,f) Diagram, fluorescent image, and red/green bacteria counts for fluorescent image in *(e)* after SAW device activation. Device activated for 60 seconds with 250 microwatts delivered to the fluid.

Although fluorescence data indicating preferential binding to protein microspots are promising, SEM images provide a clear verification cells bind to protein patterned spots. *Figure 6* demonstrates RBL Mast cell localization on BSA-DNP patterned microspots. IgE receptors present on RBL Mast cells bind to BSA-DNP specifically causing cell adhesion to protein spots.

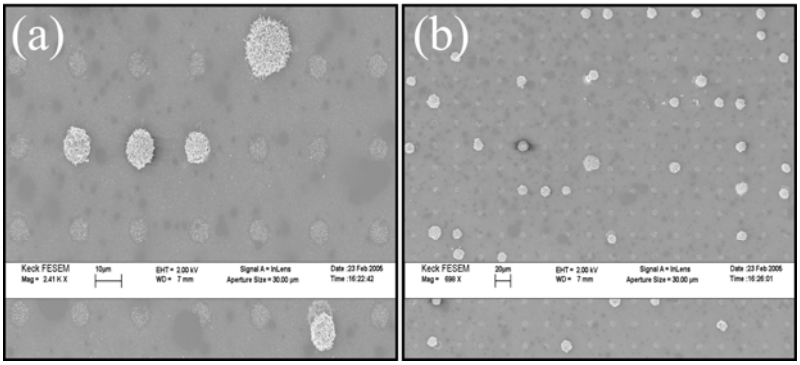

Figure 5.6. (a,b) SEM images with RBL Mast cells bound specifically to BSA-DNP protein microspots.

D. Membrane Permeation

High fluid velocities near the SAW device surface and SEM images in *Figures 4 & 6* suggested devices could potentially permeate cell membranes. RBL Mast cells were incubated on substrates for 60 minutes. After incubation, devices were driven at 250 microwatts for 300 seconds. Cells were fixed and sputtered with gold/palladium. *Figure 7(a)* presents a control SEM image with immobilized cells adhering *via* integrins and transmembrane proteins to a SAW device surface. *Figure 7(b)* presents an SEM image taken between the SAW transducers after activation demonstrating significant membrane disruption.

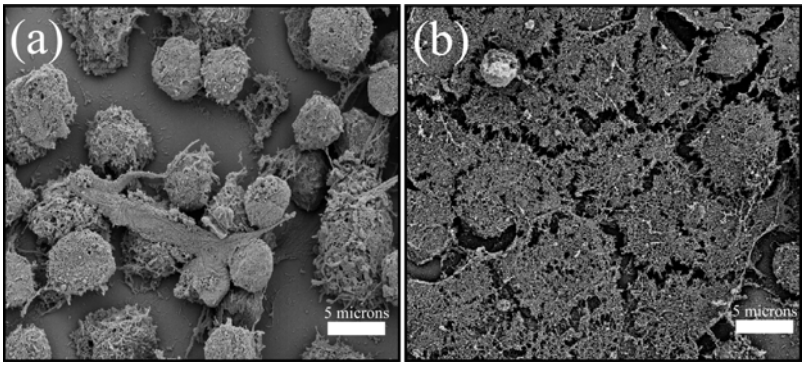

Figure 5.7. (a,b) SEM images displaying RBL Mast cells adhered to SAW surfaces without acoustic exposure (a) and with exposure at 250 microwatts for 300 seconds (b).

SEM images provide clear membrane disruption evidence, yet prove time consuming and difficult to quantify. Fluorescence provides a convenient and immediate method for quantifying membrane permeation *vs.* SAW exposure time. Fluorescence microscopy quantifying lipid-soluble and lipid- insoluble dye intensity is a convenient method used to quantify cell membrane permeation.

Transformed ovarian surface epithelial cells were incubated in PDMS reservoirs placed between SAW transducers (reference *Figure 1*) for 60 minutes to allow sedimentation and adhesion. Devices were driven with 250 microwatts delivered to the fluid volume for 0, 5, 30, and 240 seconds. After SAW exposure, reservoir fluid volumes were exchanged for HBSS buffer followed by a 15 minute fluorescent nucleic acid dye incubation (a one-to-one mixture containing green (lipid-soluble) and red (lipid-insoluble), HBSS wash step, and one hour 4% glutaraldehyde fixation step. *Figure 8(a, b, c)* shows red, green, and combined fluorescent images after SAW exposure for 0 sec *(a1, b1, c1)*, 5 sec *(a2, b2, c2)*, 30 sec *(a3, b3, c3)*, and 240 sec *(a4, b4, c4)*. *Figure 8(d)* plots red intensity *vs.* time.

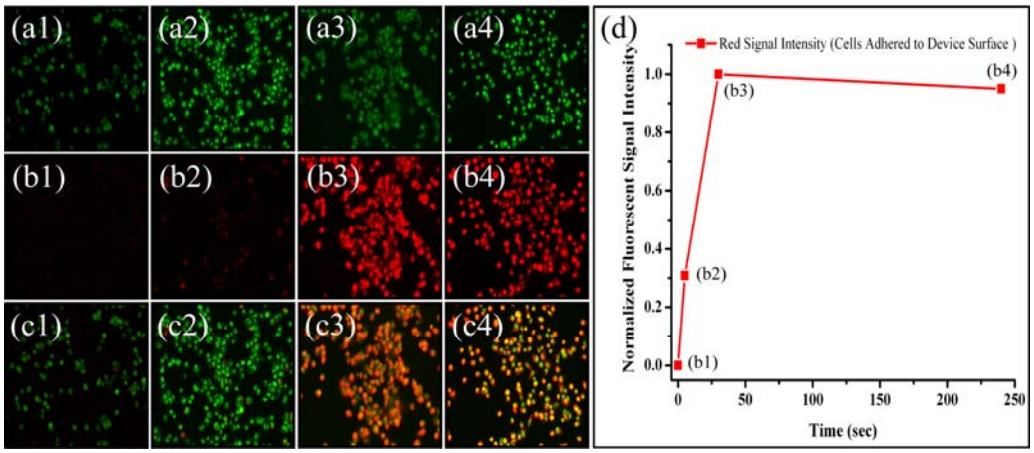

Figure 5.8. Transformed ovarian surface epithelial cells excited after nonspecific adhesion. (a1–green, b1–red , c1–combined) Control and **(a2,b2,c2; a3,b3,c3; a4,b4,c4)** three separate devices excited at 250 microwatts for increasing exposure times (5, 30, 240 seconds). Green dye is lipid-soluble. Red dye is lipid-insoluble (membrane impermeant), and, therefore, cannot diffuse through lipid bilayers unless disrupted. **(d)** Red fluorescence *vs.* SAW exposure time plot.

In addition to adherent cell membrane permeation, we performed a similar experiment on cells in solution. Transformed ovarian surface epithelial cells in suspension were added to PDMS reservoirs and immediately driven for 15, 30, 60, 120, and 240 seconds. After exposure, solution volumes contained in the PDMS reservoirs were mixed with one-to-one red/green nucleic acid dye solution for 15 minutes and fixed with 4% glutaraldehyde for 1 hour. The fluid volume was then exchanged with fresh HBSS buffer. Cells sedimented during dye and fixation incubation steps. Remaining cells were imaged to obtain red and green fluorescent intensity values *vs.* time. In performing this assay many cells were lost with buffer exchange. Hence, cell population numbers imaged were lower than adherent cell populations.

Figure 9(a,b,c) shows red, green, and combined fluorescent images after SAW exposure for 0 sec *(a1, b1, c1)*, 15 sec *(a2, b2, c2)*, 30 sec *(a3, b3, c3)*, 60 sec *(a4, b4, c4)*, 120 sec *(a5, b5, c5)*, and 240 sec *(a6, b6, c6)*. *Figure 9(d)* plots red intensity *vs.* time.

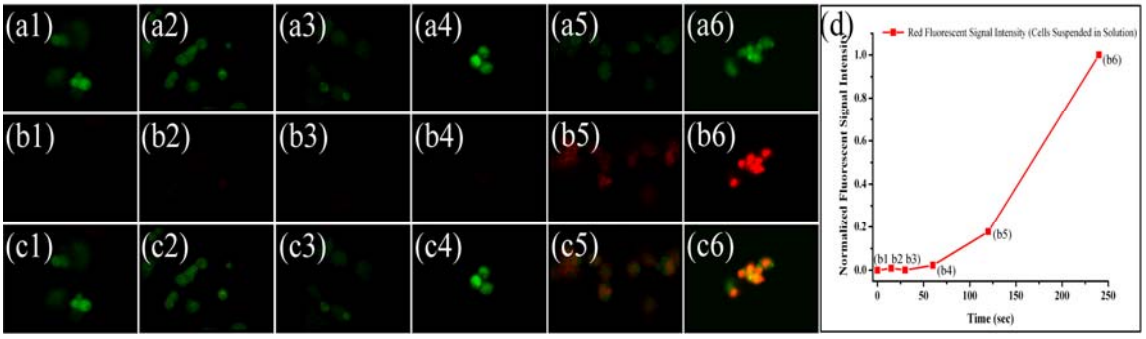

Figure 5.9. Transformed ovarian surface epithelial cells excited in solution. (a1, b1, c1) Control and **(a2, b2, c2; a3, b3, c3; a4, b4, c4; a5, b5, c5; a6, b6, c6)** five separate devices imaged after 250 microwatt exposure for 15, 30, 60, 120, and 240 seconds. Green dye is lipid soluble. Red dye is membrane impermeant, and, therefore, cannot diffuse through lipid bilayers into cells unless permeated. Red fluorescence demonstrates membrane disruption. **(d)** Red fluorescence *vs.* SAW exposure time plot.

Interestingly, cells in solution exposed to acoustic waves for 60 and 120 seconds adhered and extended lamellipodia (*Figure 10*) indicating exposure permeates cell membranes without disrupting cytoskeletal remodeling function. Results suggest devices may prove useful in gene transfection automation.

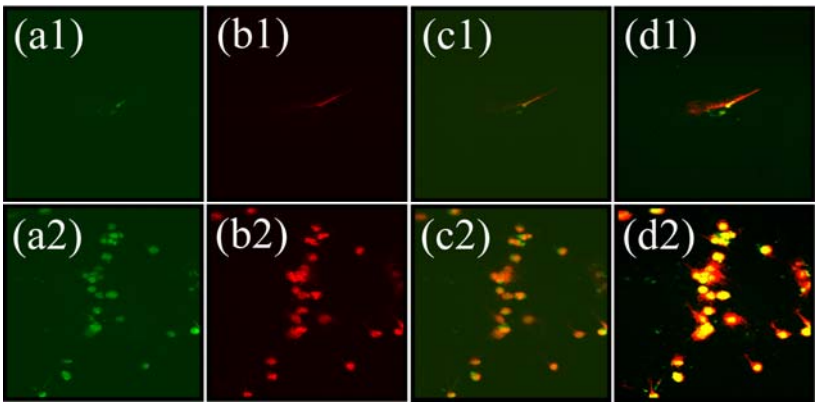

Figure 5.10. **Transformed ovarian surface epithelial cell fluorescent images demonstrating cell viability post-SAW excitation. (a1-green, b1-red, c1-combined, d1-contrast/brightness adjusted)** Epithelial cell extending lamellipodia after acoustic wave exposure for 60 seconds. **(a2, b2, c2, d2)** Epithelial cells extending lamellipodia after acoustic wave exposure for 120 seconds. Cells exposed for 240 seconds did not extend lamellipodia.

III. CONCLUSION & FUTURE WORK

Results demonstrate nonspecific bacterial cell removal, RBL Mast cell capture, and time-dependent transformed ovarian surface epithelial cell membrane permeation. A practical automation application where devices may find utility exists in releasing adherent cells cultured on-chip. Cell culture requires significant costs, both human and material, which may be reduced with automation. As cells proliferate, release requires careful laboratory cleanliness, skilled cell culture technologists, and significant time. Automating steps and eliminating environmental contamination risks is clearly desirable. Mechanical release required when passing cells after proliferation and spreading is routinely achieved by sharply knocking ("rapping") flasks, after trypsin addition. This is a combined chemical/mechanical release process. When

flasks are rapped, the removal mechanism is an impulsive mechanical shock to the flask wall. Automating this process would reduce variation in experiments rich in biological variability alone.

Obtaining release kinetics for nonspecific and specifically bound cells would prove useful. Further work is required to determine the lysis mechanism.

Red fluorescent signal intensity *vs.* time plots indicate cells captured at the device surface are quickly permeated while cells in solution require extended exposure. Future work will seek to leverage energy localization at the transducer surface to improve cell capture from large volumes and selectively permeate bound cells post-separation for intracellular molecular diagnostic applications.

We have treated the mammalian and bacterial cell types in this study superficially, neglecting significant differences which exist between cell types. Bacterial cells are typically resilient and smaller in dimension when compared to mammalian cells. Further work is required to determine whether SAW devices lyse bacterial cells.

IV. METHODS & MATERIALS

A. Microfabricated Chips

SAW device fabrication is detailed in *Reference 8*. The parylene patterning process is detailed in *References 19 and 20.*

B. Device Packaging – Macro/Microscale

Printed circuit boards were obtained from ExpressPCB. Fixtures were machined from Lexan using standard machine shop equipment. Press-to-seal silicone isolator wells (PDMS reservoirs) were obtained from Grace Bio-Labs, Inc.

C. Protein Patterning

Protein patterned SAW devices were prepared by the following steps. Devices were cleaned with acetone and isopropanol. 3-Aminopropyltrimethoxysilane (APTES) solution was prepared with 100% ethanol in 18 MΩ water 90:10 volume/volume (v/v). To this solution was added 1% glacial acetic acid and 1% APTES with glass pipettors. Devices were immersed in APTES solution for 2 hours and immediately rinsed in 18 MΩ water three 3 times and dried with nitrogen upon removal. Silanized substrates were incubated for 30 minutes with 2.5% glutardialdehyde in PBS buffer and washed three times with 5 minute incubations between buffer wash steps. Protein (BSA-DNP was generously provided by the Baird group and antibody against E. *coli* 0157:H7 obtained from Kirkegaard & Perry Laboratories Inc.) was incubated for 2 hours and washed three times. RBL Mast cells and bacterial cells were incubated upon this surface chemistry with appropriate receptors molecules attached.

D. Fluorescence Measurements

The LIVE/DEAD® Reduced Biohazard Viability/Cytotoxicity Kit #1 (L-7013) was purchased from Invitrogen. Buffers and dye solution mixture protocols are listed in product literature.

E. Cell Line Information

Mast Cells: RBL-2H3 Mast cells were maintained as monolayers in culture and harvested with Trypsin-EDTA (Life Technologies, Rockville, MD, USA) 3–5 days after passage. Cells were suspended at 2×10^6 cells/mL in a buffered saline solution (BSS: 135 mM NaCl, 5.0 mM KCl, 1.8 mM CaCl2, 1.0 mM $MgCl_2$, 5.6 mM glucose and 20 mM HEPES, pH 7.4) and incubated on SAW devices coated with BSA-DNP (protein-hapten conjugate). Mast cells were sensitized with anti-DNP IgE.

Epithelial Cells: Transformed ovarian surface epithelial cells OSN1 were used for membrane permeation analysis. Cells were suspended at 1×10^6 cells/mL in a buffered saline solution. Cell line details reside in *Reference 21*.

Bacterial Cells: Heat killed formalin fixed PANSORBIN® Staphylococcus *aureus* cells were obtained from Calbiochem. Heat killed, fixed H7:O157 Escherichia *coli* cells were purchased from Sigma-Aldrich. Cells were suspended in PBS buffer at a cell concentration of 1 x 10^8 cells/mL and mixed one-to-one for specific/nonspecific release experiments.

F. SEM Parameters & Sample Preparation Protocol

To fix cells and prevent cell morphology changes after SAW excitation the following steps were performed. Buffer was exchanged in PDMS reservoirs three times with 10X PBS buffer. Fixation with a 2.5% glutaraldehyde solution in phosphate buffer for 15 minutes was used to crosslink proteins. The fixation was quenched with PBS solution exchange and incubation in a solution containing 25 mM glycine in PBS for 10 minutes. Samples were incubated in a 0.2% BSA and 0.2% fish gelatin in PBS for 15 minutes. The samples were then washed three times with PBS. The following buffer mixture was substituted for PBS at pH 7.4 (3:1 0.2M NaH2PO4:0.2 M Na2HPO4) with three successive washes and 5 minute incubation times. Buffer was then exchanged with 18 MΩ water three times with 5 minute incubations.

To prepare samples for SEM imaging samples were dehydrated incrementally with 10%, 30%, 50%, 70% and 90% ethanol in 18 MΩ water (v/v) and incubated for 5 minutes. Samples were washed three times in 100% ethanol and dried in a Bal-Tec CPD 030 critical point dryer followed by gold/palladium sputtering. Scanning electron microscopy (SEM) was performed using a LEO 1550 FE-SEM, with an in-lens secondary electron detector.

APPENDIX

A. Acoustic Wavelength and Cell Diameter

Fluorescence results demonstrate cell membrane permeation. Transformed ovarian surface epithelial cells exposed to surface acoustic waves have a diameter of 10 microns. Exposing cells to pressure wave peaks and troughs exerts a stress across the cell membrane and applies hydrodynamic drag to immobilized cells. The 5 second SAW exposure image of adhered cells has isolated bright red regions which indicate significant membrane rupture (*Figure 8(b2)*). It is likely this occurs because unattached membrane separates from the area adhered to the solid-support creating a large tear permeable to red dye.

Cells excited in free solution are transiently exposed to amplitude peaks and troughs. Free solution fluorescent images appear more uniform, potentially indicating multiple permeation points on the cell membrane.

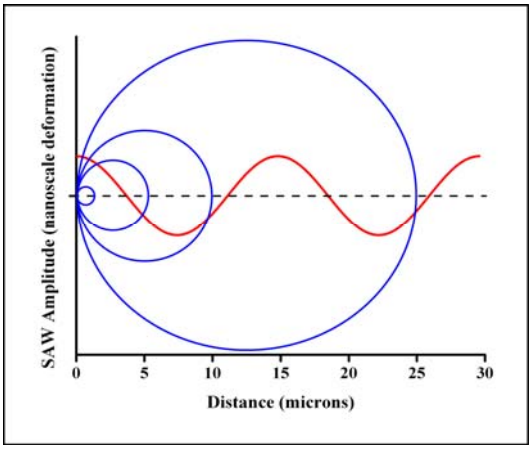

Figure 5.11. SAW Amplitude as a function of distance for a 95 MHz SAW device. Depending upon cell diameter, cells may be exposed to multiple pressure wave peaks and troughs.

B. Mean Capture Time & Sedimentation Calculations (One Dimensional Diffusion)

Applications such as circulating tumor cell capture require probing fluid volumes measured in *milliliters*. Probing large volumes requires convective transport for rapid analysis. To determine timescales for diffusion and sedimentation relevant to our system we followed the simple constructs outlined by Berg [22]. Ignoring gravity, a valid assumption for proteins and nanoscale objects, a random walk model with an absorbing and reflecting interface was used to determine the mean time to capture. Even proteins, which diffuse rapidly, when compared to cells, may take many minutes to be captured by diffusive transport. *Figure 12* depicts the model schematic. *Equation 3* was used to plot the mean time to capture *vs.* protein radius and microchannel height.

$$t_{avg} = \frac{2\pi\mu r b^2}{k_B T} \quad \textbf{(3)}$$

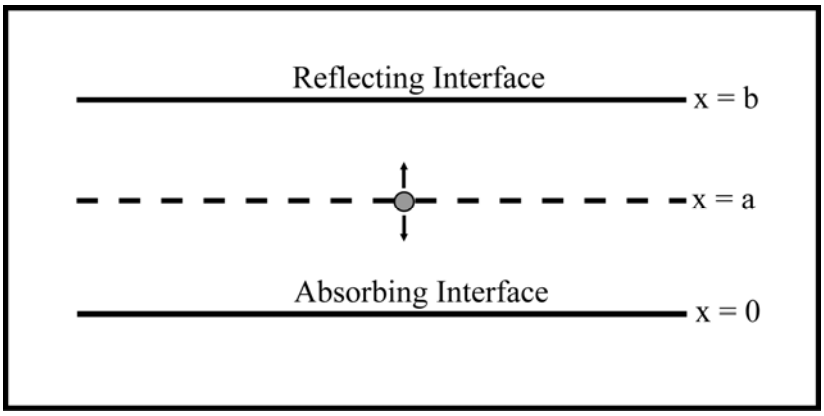

Figure 5.12. Diffusion with a reflecting and absorbing surface. Thermal excitation causes Brownian motion. The particle is perturbed randomly until capture.

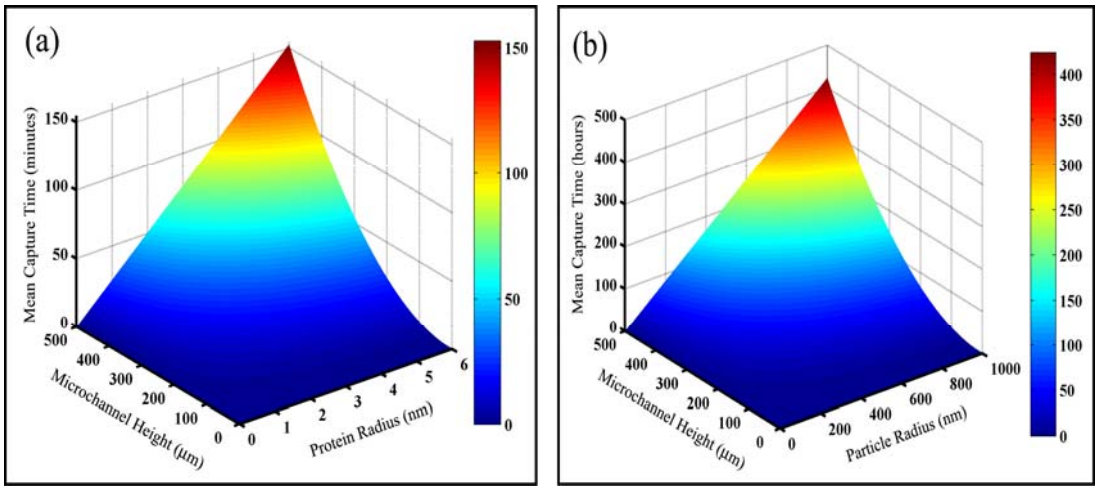

Figure 5.13. Theoretical mean time to capture for diffusion limited nano/microscale particle transport in whole blood. Plots assume a 25 °C temperature.

C. Sedimentation Velocities

Cells and microparticles settle with time. Mixing adds energy to the system. This energetic input can be used to overcome gravitational and adhesive forces. *Equation 4* was used to determine settling velocity *vs.* density and cell/particle radius (*Equation 4* does not include Brownian motion).

$$v_{sed} = \frac{2r^2(\rho_s - \rho_g)}{9\mu} \quad \textbf{(4)}$$

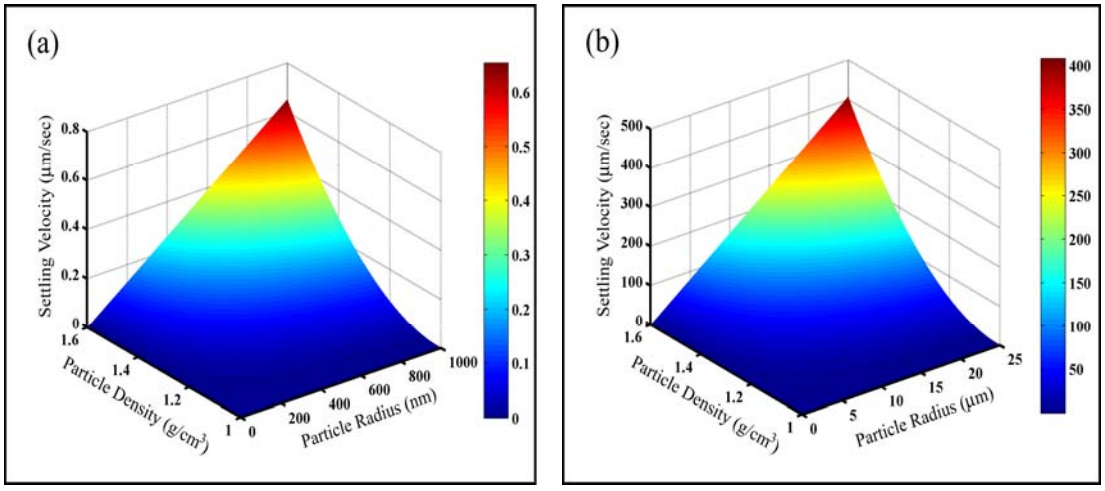

Figure 5.14. Theoretical sedimentation velocities for spherical nano/microscale particles residing in serum *vs.* particle density and radius.

D. Image Analysis

Fluorescent image analyses used to quantify membrane permeation experiments required image intensity thresholding and mean pixel population intensity calculation. Thresholding was required to define signal and background pixels (MATLAB was used for image analyses). Computing nonspecific/specific cell release from fluorescence data required image processing to define patterned and nonpatterned pixel areas. Image intensity thresholding, Fourier analysis used to generate regions-of-interest, and overlay with brightfield images are depicted in *Figure 15.*

Raw membrane permeation fluorescent images were analyzed to determine relative intensity shifts in red (lipid-insoluble) dye intensity. Intensity thresholding was used to isolate pixel populations.

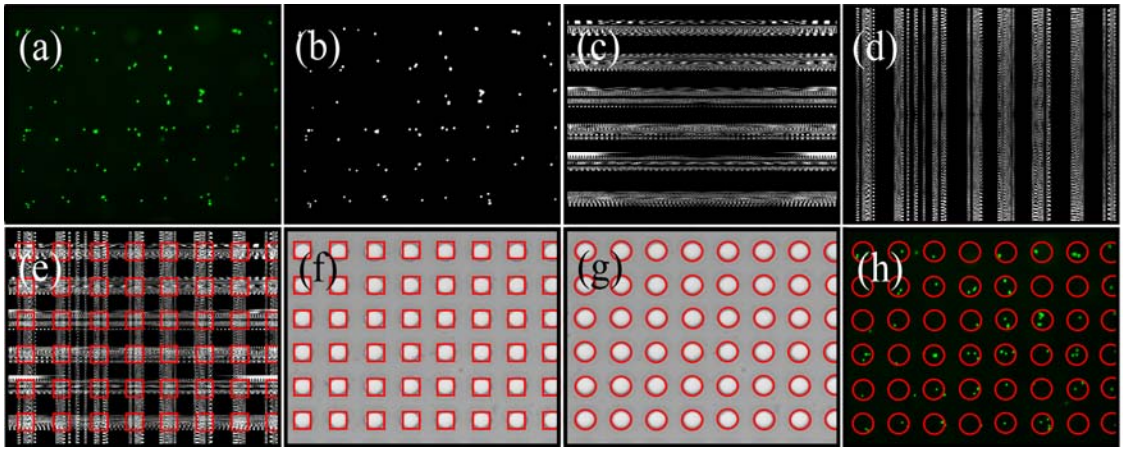

Figure 15. **(a)** Bacterial adhesion to protein micropatterns demonstrated with fluorescence microscopy. **(b)** Image intensity threshold applied to fluorescent image (a). **(c)** Fast Fourier Transform applied to image as depicted in (b) with 90 degree clockwise rotation. **(d)** Fast Fourier Transform applied to image as depicted in (b) **(e)** Images (c) and (d) added. **(f)** Bounding protein micropattern boxes generated from FFT overlay bright-field open areas. **(g)** Bright-field image demonstrating micropattern open areas accessible to protein immobilization chemistry. Red circles define regions of interest from brightfield image. **(h)** Fluorescent image with red overlay pattern generated from (g).

ACKNOWLEDGMENT

We thank the Baird lab for generous Mast cell and BSA-DNP donations. The transformed ovarian surface epithelial cell line OSN1 was developed and kindly provided by Andrea Flesken-Nikitin Alexander Nikitin, and Becky Williams. Flow velocity data and microsphere images were generously provided by Darren Branch.

REFERENCES

[1] Kricka, L.J. & Wild, D. *The Immunoassay Handbook*, Third Edition, David Wild Ed., ELSEVIER Ltd.: Oxford, **2005,** 298-299.

[2] Ekins, R.P. *Clinical Chemistry*, **1998**, vol. 44(9), 2015-2030.

[3] Klenin, K., Kusnezow, W., Langowski, J., *The Journal of Chemical Physics*, **2005**, 122, 214715.

[4] Kusnezow, W. *et al. Proteomics*, **2006**, 6, 794-803.

[5] Kusnezow, W. *et al. Molecular & Cellular Proteomics*, 5, **2006**, 1681-1696.

[6] Allard, W. J. *et al.*, "Tumor Cells Circulate in the Peripheral Blood of All Major Carcinomas but not in Healthy Subjects or Patients With Nonmalignant Diseases", *Clinical Cancer Research***,** Vol. 10, 6897–6904, October 15, **2004**.

[7] D. Kim, W. Cha, & R.L. Beissinger, "Mass Transport of Macromolecules in Solution to Surfaces", *J. Colloid & Interface Science*, vol. 159, 1-8, **1993**.

[8] Meyer, G.D., Morán-Mirabal, J.M., Branch, D.W., and Craighead, H.G., *IEEE Sensors Journal*, vol. 6, no. 2, April **2006**.

[9] Aubrecht, D.M., Meyer, G., & Craighead, H. G., Sensors & Actuators B.

[10] Meyer, G., & Craighead, H. G., *Analytical Chem.*,

[11] J. Smith & V. Hinson-Smith, "The New Era of SAW Devices", *Analytical Chemistry*, 3505-3507, 1 June **2006**.

[12] C.M. Harris, "Seeing SAW Potential", *Analytical Chemistry*, 355-358A, 1 August **2003**.

[13] G.G. Yaralioglu, "Ultrasonic Mixing in Microfluidic Channels Using Integrated Transducers", *Anal. Chem.* **2004**, 76, 3694-3698.

[14] A. Toegl, R. Kirchner, C. Gauer, & A. Wixforth, "Enhancing Results of Microarray Hybridizations Through Microagitation", *J. Biomolecular Techniques*, vol. 14, iss. 3, Sept **2003**.

[15] M. Hartmann, A. Toegl, R. Kirchner, & M.F. Templin, "Increasing robustness and sensitivity of protein microarrays through microagitation and automation", *Analytica Chemica Acta*, 564 (**2006**), 66-73.

[16] Kuznetsova, L. A. & Coakley, W.T., *Biosensors & Bioelectronics*, **2007**, 22, 1567-1577.

[17] S. Seeger *et al*. "Preparation & Characterization of Antibody Films on Litthium Niobate Surfaces", *Synthetic Microstructures in Biological Research*, Plenum Press, New York, Eds. J.M. Schnur & M. Peckerar, **1992**.

[18] M. A. Hubbe, "Theory of Detachment of Colloidal Particles from Flat Surfaces Exposed to Flow", *Colloids & Surfaces*, 12 (**1984**) 151-178.

[19] B. Ilic and H. G. Craighead, Biomed. Microdevices, vol. 2, no. 4, pp. 317–322, **2000**.

[20] J. M. Moran-Mirabal, J. B. Edel, G. D. Meyer, D. Throckmorton, A.
K. Singh, & Harold G. Craighead, "Micrometer-Sized Supported Lipid Bilayer Arrays for Bacterial Toxin Binding Studies through TIRFM", *Biophysical Journal*, v.89, July **2005**, 296-305.

[21] Corney, D. C., Flesken-Nikitin, A., Godwin, A. K., Wang, W. and Nikitin, A.Yu. "MicroRNA-34b and -34c are targets of p53 and cooperate in control of cell proliferation and adhesion-independent growth", **2007**, *Cancer Res* . In revision.

[22] H. C. Berg, *Random Walks in Biology*, Princeton University Press, **1983**, 37-64.

CHAPTER SIX

Design, Fabrication, & Characterization of a Fiber Optic Endoscope Scanner for Clinical *In Vivo* Multiphoton Tissue Imaging

Grant Meyer, Hyungsik Lim, Chris Xu, Harold G. Craighead, & Watt W. Webb

Cornell University, School of Applied Physics, USA

ABSTRACT

While multiphoton microscopy is extensively chronicled in the biomedical tissue imaging literature, a clinically optimized multiphoton endoscope yielding real-time, *in vivo* tissue images is absent. We produce a two-dimensional piezoelectric raster scanner design, fabrication, and electrical/mechanical characterization methods necessary to integrate a single mode fiber into a multiphoton endoscope geometry meeting clinical and surgical demands. A two-dimensional scanner prototype made with PZT piezoelectric sheet is detailed and characterized. The key characterization values include photon emission angles *vs.* input voltage, fiber deflection amplitudes *vs.* input voltage, and higher order frequency contributions to single mode fiber motion. Scanner design improvements and mechanical mode profiles arising from an established model and experiment are also discussed.

I. INTRODUCTION

Medical endoscopes are used in clinical and surgical procedures to yield qualitative *in vivo* tissue images. While numerous research and clinical endoscope designs exist, most video endoscopes image large tissue areas (i.e. cm^2) and rarely produce quantitative results. Surgeons require a square centimeter field-of-view to find diseased tissue on large organs (e.g. bladders, intestines, lungs, and colons). After a surgeon isolates regions of interest and biopsies the questionable tissue, the sample is transferred to pathology for hematoxylin and eosin (H&E) staining, pathologist analysis, and tumor grading (if cancerous). Following tissue analysis, pathologists may suggest additional diseased tissue excision, requiring further surgical and analytical work cycles. This division of labor introduces significant discomfort, inconvenience, and time delay into risky surgical procedures. Introducing high-resolution multiphoton imaging into medical endoscopes would extend nonlinear biomedical imaging techniques into clinical and surgical procedures to reduce patient burden and surgeon risk.

Tissue biopsy procedures are time and resource intensive, not to mention painful. Tissue biopsy routinely requires general anesthesia, precipitating inpatient costs, which far exceed outpatient costs. Developing real-time, minimally invasive clinical instruments shifting inpatient procedures to outpatient procedures has clear patient and societal benefit. Unlocking patient and societal benefits requires a transition from traditional histopathology techniques (i.e. H&E staining) to advanced microscopy and digital image processing tools currently residing in basic research institutions. A high-resolution biomedical tissue imaging technology, detailed by Zipfel, Williams, & Webb, is multiphoton microscopy [1]. Microscopy embodiments and *in vivo* imaging utility are given in *References 2-5*.

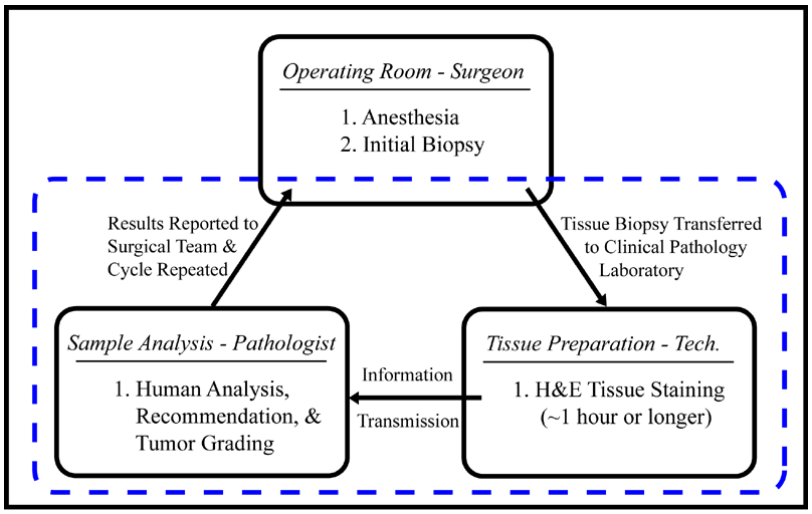

Figure 6.1. Current clinical tissue harvesting, staining, and analysis practices. A real-time medical endoscope could, potentially, simplify the steps outlined by the dotted line and reduce cycle times.

Multiphoton microscopy typically requires 100 femtosecond laser pulses to excite tissue. Pulses are transmitted *via* single-mode fiber optic cable optimally designed to transmit femtosecond pulses. Single-mode fiber optic cable has a 6 micron air core to guide photons. Because the core is only 6 microns, and the beam is demagnified before reaching the tissue, only a small tissue area is excited by photons. Hence, the single mode fiber optic cable must be translated in two dimensions to obtain a larger field of view (FOV). Piezoelectric devices convert a voltage into a mechanical deformation, meeting fiber actuation requirements.

Numerous two and three dimensional optical scanning designs exist. Scanners yielding Lissajous fiber motion are discussed in *References 4 and 6.* Alternatively, Myiang *et al.* detail a spiral scanning endoscope [7]. A system using dual-wedge rotating optics is detailed in *Reference 8.* Recently, Jurgen and Denk detailed a "trimorph" piezo system designed to produce large fiber tip deflections *via* a lever principle [9]. Denk's design provides random access imaging capability necessary for

imaging a large area to find a region of interest followed by magnification (i.e. zoom) to image a local area with higher resolution.

In this work we produce a raster scanner design and characterization methods. A raster scanning method was chosen because the fiber tip motion is simple relative to Lissajous and spiral scanning motions. The chosen design is compact, blocking little tissue emitted light. The two-dimensional PZT actuator prototype produces a slow (1 Hz—*x*-axis) oscillatory and resonant (790 Hz—*y*-axis) fiber tip deflection.

II. TWO-DIMENSIONAL PIEZO SCANNER DESIGN

A. Endoscope Design—Distal End

The piezo scanner is integrated at the distal end near the tissue to be imaged. A diagram detailing scanner placement inside the endoscope housing and the optical

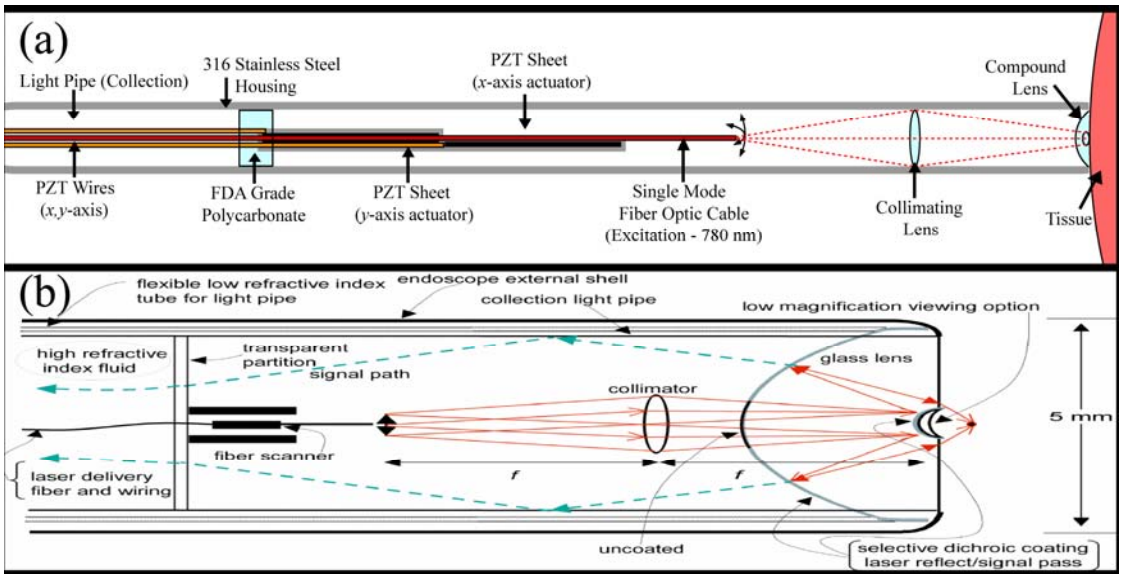

Figure 6.2. Endoscope Side View Schematic – Distal End. (a) Diagram depicts coaxial cables, scanner elements, and optics abutting tissue. **(b)** Optical component side-view. Fiber optic cable must be scanned in two-dimensions to excite a tissue area.

components necessary to create low and high magnification images is drawn in *Figure 2.* The laser system, detectors, and electronic equipment necessary to drive and

monitor the piezo scanner inputs and outputs as well as photon counting equipment reside at the proximal end.

B. Piezoelectric Fiber Scanner Design

Two piezo elements are required to create two-dimensional raster scanning fiber motion. Each electrically isolated piezoceramic bender is cut from a larger sheet and integrated into optically transparent FDA grade polycarbonate for placement inside the stainless steel housing. A schematic depicting each piezoceramic bender, the fiber tip overhang, prototype design dimensions, and ideal deformation distances is depicted in *Figure 3*. Motion generated by the *x*-axis piezo is expected to scan at 1 Hz over a 0.5 mm distance. Motion generated by the *y*-axis piezo excites the fiber tip near resonance at ~1 kHz creating a 1 mm fiber deflection. Prototype characterization will experimentally determine deflection amplitudes, frequencies, and mode shape.

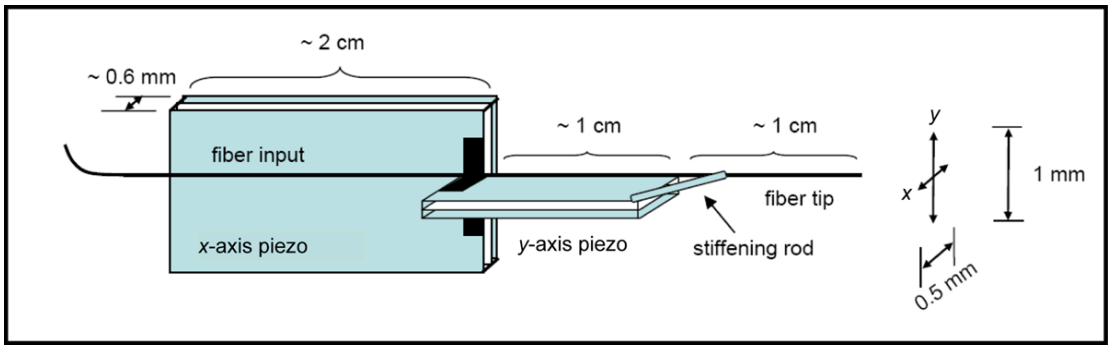

Figure 6.3. Initial Two-Dimensional Piezo Scanner Design. A 1.0 mm resonant *y*-axis deflection and non-resonant 0.5 mm *x*-axis deflection are depicted (far right). Calculations indicate a ~1 kHz resonant oscillation is expected with a 10 mm fiber overhang length (*See Figure 4 for detail*).

C. Fiber Overhang Distance—Resonant Frequency Calculations

The fiber tip overhang is an important parameter in the prototype design. This distance controls the *y-axis* resonant fiber frequency. A 1 kHz *y*-axis frequency is required for rapid image acquisition.

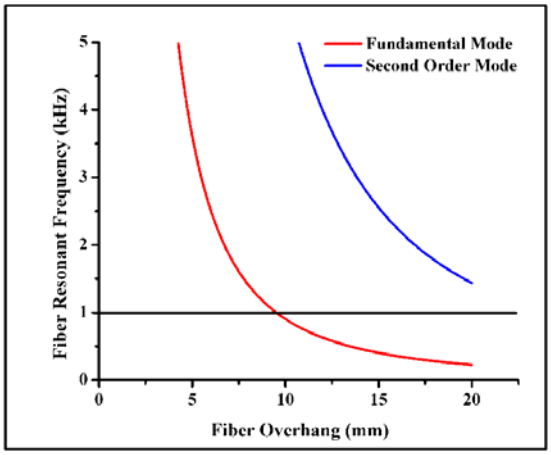

Figure 6.4. Fiber resonant frequency *vs.* fiber tip overhang (distance from *y*-axis piezo element).

$$\nu = \frac{\beta}{2\pi L^2}\sqrt{\frac{EI}{\rho A}} \quad \textbf{(1)}$$

Table 6.1. Resonant Frequency Calculation Parameters

Parameter	Symbol	Value
Shape/Mode Parameter	β	3.52, 22.4
Fiber Overhang Length	L	5-20 mm
Young's Modulus (Silica)	E	7.17 x 10^{10} Nm^{-2}
Density (Silica)	ρ	2.7 x 10^{3} kg/m^{3}
Fiber Radius	R	62.5 microns
Fiber Cross-Sectional Area	A	πR^2
Second Moment of Area	I	$\pi R^4/4$

D. Piezo Bender Current Consumption Calculation

Given the clinical application, it is important to consider the peak current supplied to the piezoelectric sheet. *Equation 2*, where I is current, f is frequency, C is capacitance and V is voltage, produces this quantity.

$$I_{Peak} = 2\pi f C V_{Peak} \quad \textbf{(2)}$$

E. Optical Design Constraints

Clinical tissue imaging requires macro and microscale fields-of-view. Joint discussions with surgeons and pathologists isolated three fields-of-view meeting clinical and surgical needs. Details are listed in *Table 2*.

Table 6.2. Imaging Modes & Corresponding Fields-of-View

	Video	MPM (Low Mag)	MPM (High Mag)
FOV	1 cm x 1 cm	200 μm x 200 μm	50 μm x 50 μm

III. MATERIALS & COMPONENTS

A. Small & Large Endoscope Cross-Sections, PZT Material Cross-Section, & Prototype Images

Designing an endoscope for clinical use places material restrictions on our design. *Figure 5(a)* details the prototype two-dimensional bender and PZT piezoceramic cross-sections. Initially, a design with a 2 mm radius was pursued. In future, a larger endoscope with a 4 mm radius may be pursued to improve tissue-emitted photon collection. *Figure 5(b)* images PZT sheet supplied by Piezo Systems Inc (T234-H4CL-303X). PZT(5H) was cut to meet prototype dimensional requirements with a diamond saw. The piezoceramic sheet cross-section include two nickel electrodes, which contact electrical wires, a proprietary bonding material, and the center piezoceramic PZT(5H). *Figure 5(c)* shows polycarbonate plugs machined from optically clear sheet (Makrolon—Bayer Medical Grade Polymers) inserted into medical grade 316 stainless steel. The assembled bender was epoxied into a polycarbonate plug (Miller-Stephenson 907). *Figures 5(d,e)* prototype images capture top and side views.

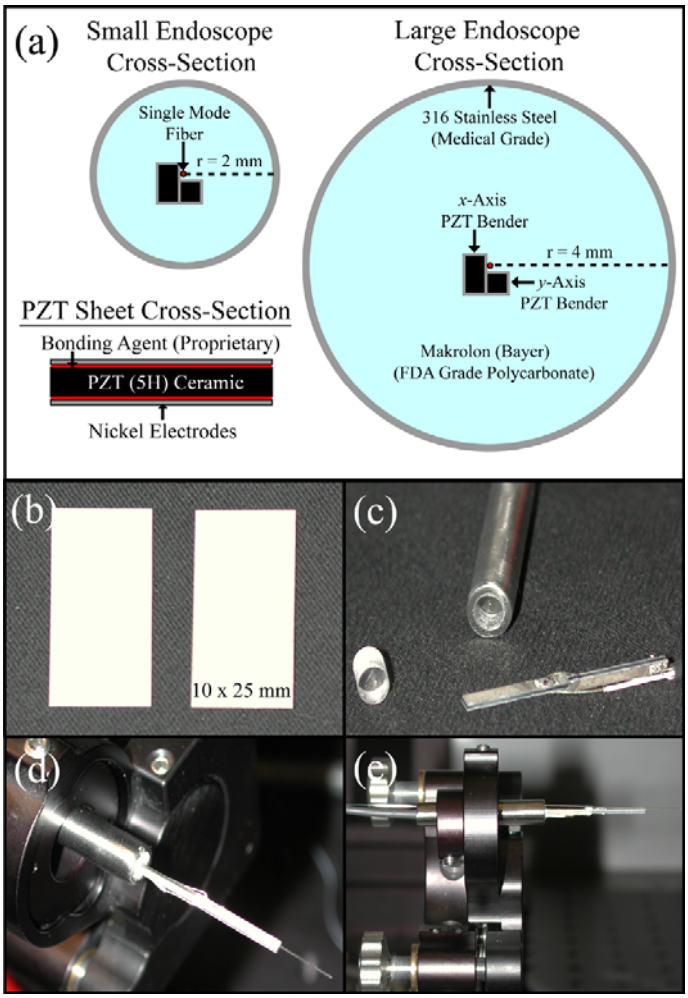

Figure 6.5. Prototype Cross-Section Diagram and Fabrication Detail. (a) Small and large diameter endoscope cross-sections. **(b)** Supplied PZT(5H) piezoceramic sheet. **(c)** Optically transparent FDA grade polycarbonate machined to fit stainless steel housing and *x*,*y*-axis piezo bender elements. **(d)** Prototype with fiber attached to *y*-axis bender. **(e)** Prototype integrated with standard optical alignment fixture side-view.

B. Single Mode Optical Fiber Detail

The single mode fiber optic cable visible in *Figure 5(d)* has a complex geometry (Supplier—Crystal Fibre). *Figure 6(a)* is a SMF cross-section schematic with dimensions. *Figure 6(b)* is a SMF air cladding and air core scanning electron microscope image detailing the SMF air core cross-section with dimensions (Crystal Fibre). *Figure 6(c)* depicts a 100X magnified microscope image of a SMF showing

acrylate coating and silica cladding (side-view). *Figure 6(d)* depicts a 100X magnified microscope image of a cleaved silica fiber tip (side-view).

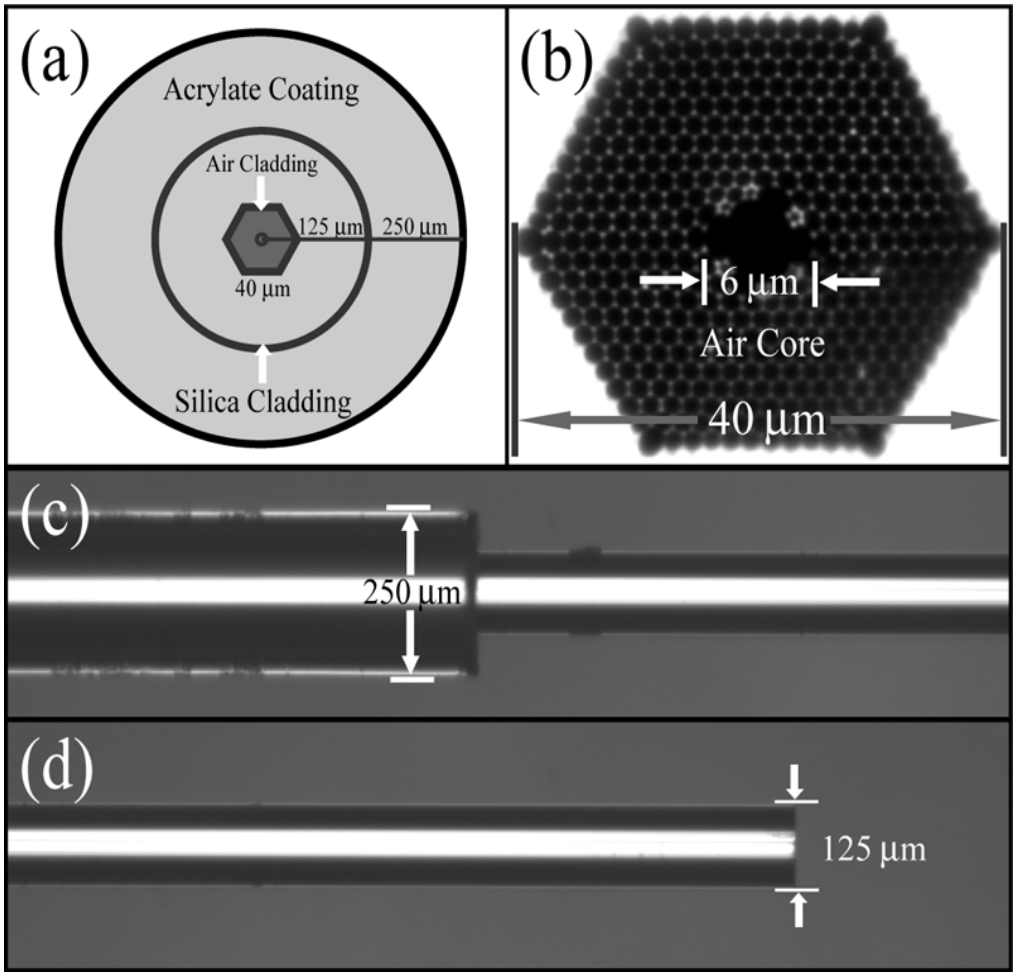

Figure 6.6. Single Mode Fiber (SMF) Detail – Optimized for 780 nm, 100 femtosecond laser pulses. (a) SMF cross-section and dimensions. **(b)** Air cladding and air core cross-sections with dimensions. **(c)** Fiber side-view depicting acrylate coating and silica cladding **(d)** Cleaved silica fiber tip.

C. Electronic Equipment

Piezoceramic devices were driven sinusoidally (AC) and incrementally (DC) with an Agilent waveform generator and broadband power amplifier obtained from Piezo Systems Inc (EPA-104-115).

IV. FABRICATION

A. Initial Two-dimensional Bender

Assembling the components outlined in *Figure 5* yields the prototype detailed in *Figure 7*. *Figure 7* shows the experimental orientation and dimensions.

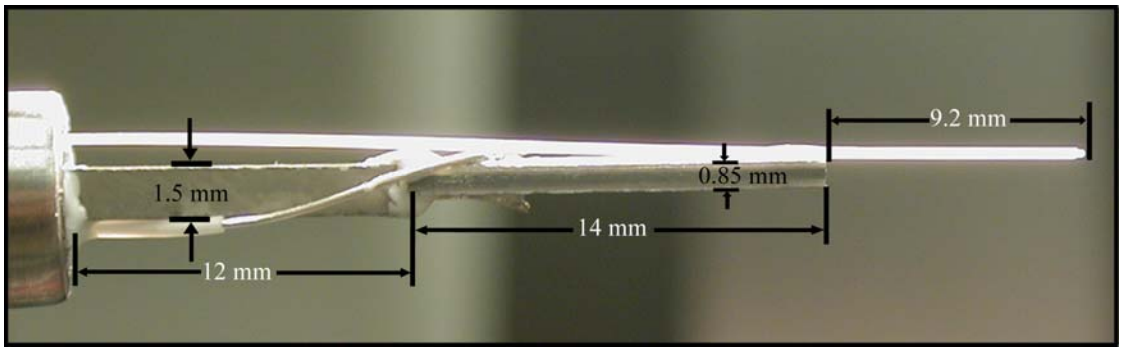

Figure 6.7. Two-Dimensional Piezoelectric Scanner Prototype.

B. Position Sensitive Detector (PSD) and Signal Conditioning Circuit

Measuring fiber tip position *vs.* time is an important prototype measurement. A device optimized for two-dimensional position measurement is the position sensitive detector (PSD—OSI Optoelectronics—DL-20). The DL-20 duo-lateral PSD has two photosensitive thin-film resistive layers. The photocurrent measured can resolve 0.5 micron light spot movements according to company documentation. The 20 x 20 mm active area has a 1.00 microsecond rise time, which is sufficient for prototype drive frequencies. *Figure 8(a)* is a PSD active area and packaging image. *Figure 8(b)* images a signal conditioning board integrated with PSD outputs. The entire unit is housed in a metal box machined to accept an optical post for proper axial alignment (*See Figure 19*).

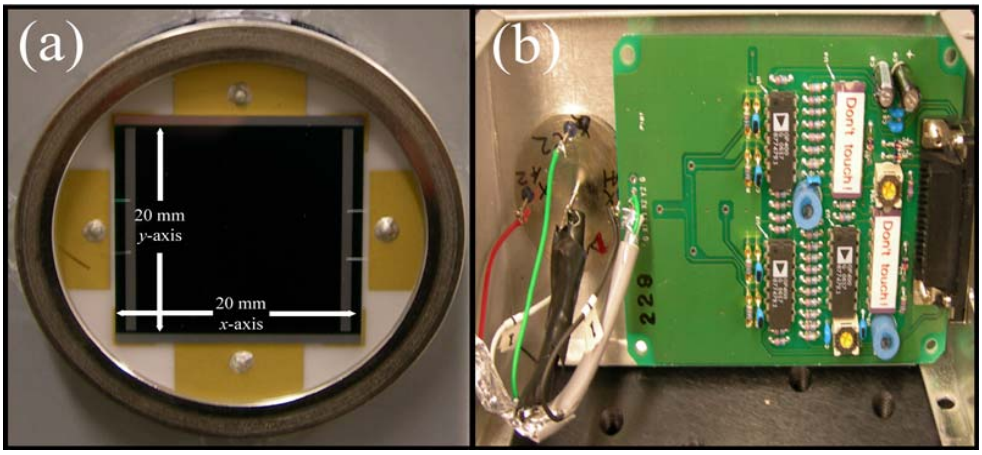

Figure 6.8. Position Sensitive Detector and Signal Conditioning Circuit (a) Packaged Position Sensitive Detector (PSD) (b) Signal Conditioning Circuit.

The signal conditioning board in *Figure 8(b)* was purchased from Hamamatsu (C4757) and is designed to work with Hamamatsu detectors. The circuit was retrofit to work with the DL-20 PSD. The circuit block diagram is reproduced in *Figure 9*. The detector was used to measure spot position by measuring outputs V5,V6,V7, & V8.

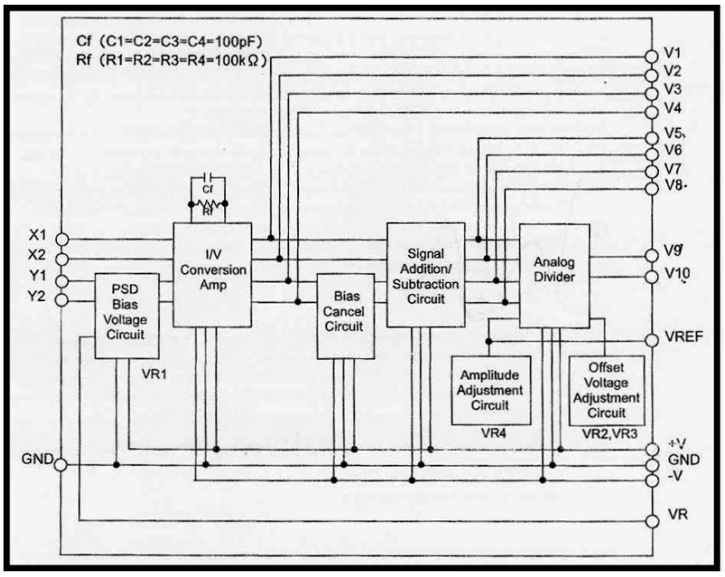

Figure 6.9. Signal Conditioning Circuit Block Diagram.

Laser spot position *vs.* time was measured using a National Instruments 6024E DAQ card with a 200 kS/s maximum sampling rate. The board outputs were processed with the *Equations 3 & 4 (L-left, T-top)*.

$$X = \frac{V5}{V6} = \frac{X_L - X_R}{X_L + X_R} \quad \textbf{(3)}$$

$$Y = \frac{V7}{V8} = \frac{Y_T - Y_B}{Y_T + Y_B} \quad \textbf{(4)}$$

The PSD output voltage *vs.* calibrated *x-axis* displacements is plotted and linearly fit in *Figure 10*. Note fit (detector) linearity. The supplier stated error in position detection across a 16 mm linear distance is 0.2 mm.

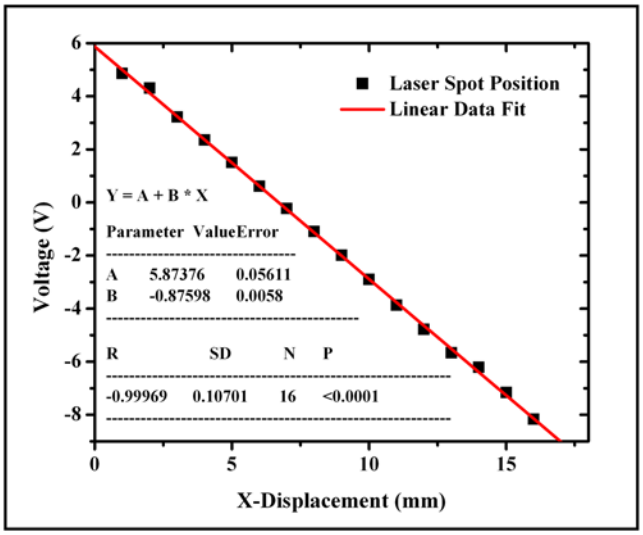

Figure 6.10. Two-dimensional Piezoelectric Scanner Prototype.

V. SINGLE MODE FIBER CHARACTERIZATION

A. Resonant Fiber Mode Characterization—Digital Image Processing

Characterizing the fiber deflection *vs.* length is critical for lens design and mechanical mode characterization. A digital image taken with a Nikon CoolPix

camera is pictured in *Figure 11(a)*. The image was processed to define fiber pixels and further processed to define the fiber deflection curve extrema (*See Figure 11(b,c)*). The curves from *Figure 11(c)* are plotted in *Figure 11(d)*. The fiber image is reproduced in *Figure 15(b)*.

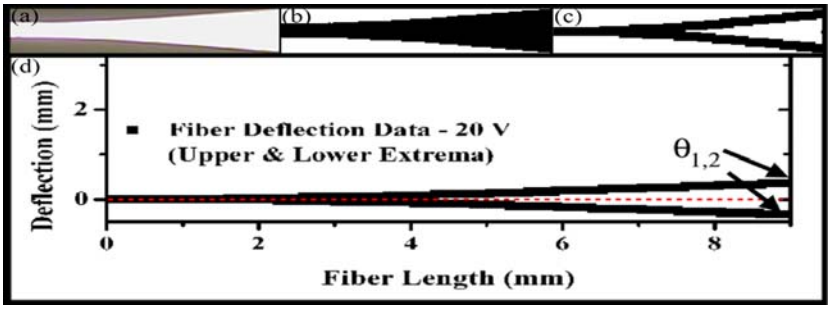

Figure 6.11. Fiber Deflection Characterization with Digital Images (side-view). **(a)** Cropped fiber photograph. **(b)** Cropped fiber with fiber sweep area defined in black. **(c)** Upper and lower extrema defined to generate curve fit data. **(d)** Fiber extrema defined and plotted. Upper and lower curves were fit to obtain photon emission angles $\theta_{1,2}$.

Images were processed in this way to define the photon emission angles *vs.* supplied voltage reaching piezo devices.

B. Photon Emission Angle Measurement—A Key Parameter for Lens Design

Photon emission angles at the fiber tip are important for lens design (*Refer to Figure 2 for lens placement relative to two dimensional raster scanner*). Hence, the tangent line at the fiber tip must be determined. Defining the tangent line requires curve fitting. The resulting curves and parameters allow photon emission angle calculation. *Figure 12* draws typical fiber profiles with increasing deflection amplitudes representing increased force applied *via* the supplied piezo voltage.

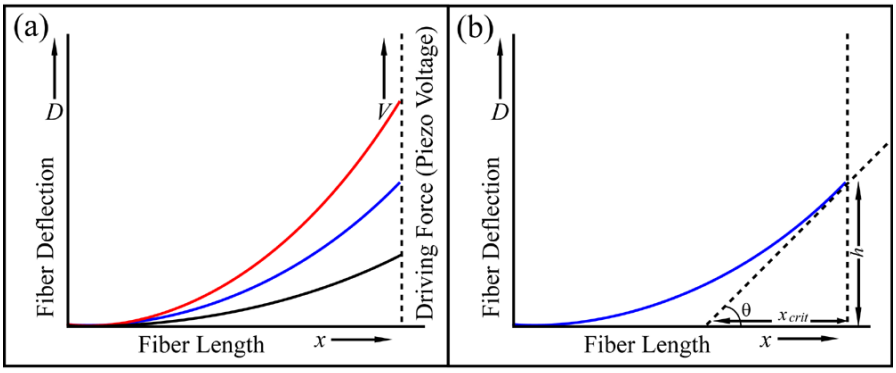

Figure 6.12. Fiber Deflection Diagram. (a) Fiber defection *vs.* length. Increasing force imparted by piezo increases deflection distance (*D*). **(b)** Fiber tip tangent line and photon emission angle parameter definitions.

Figure 13(b) defines the axes and parameters necessary for photon emission calculation. The tangent as a function of angle and deflection parameters is given in *Equation 5*.

$$\tan\theta = \frac{h}{x_{crit}} = \frac{dD}{dx} \quad \textbf{(5)}$$

The photon emission angle is computed as,

$$\theta = \tan^{-1}\left(\frac{dD}{dx}\right) \quad \textbf{(6)}$$

Fiber deflection images must be fit to a model to generate expressions for *D(x,t)*. Theoretically, beam deflection as a function of distance from a fixed point is given in *Equation 7 (See Reference 10)*.

$$\upsilon(x,t) = \frac{F_0 l^3}{EI}\sum_{i=1}^{\infty}\frac{X_i X_{i1}}{(k_i l)^4}\cos\omega_i t \quad \textbf{(7)}$$

Equation 7 is an analytical expression for the beam deflection *vs.* length, however, the free end boundary conditions yield transcendental equations. Hence, the general

mode shape is known, but not the analytical expression. The expression for a mode *i* has the general form given in *Equation 8*.

$$D_i = \left(F_{1i}(\cos k_i x - \cosh k_i x) + F_{2i}(\sin k_i x - \sinh k_i x)\right)\cos \omega_i t \quad \textbf{(8)}$$

The derivative of *Equation 8* is necessary to compute the photon emission angle**.**

$$\frac{dD_i}{dx} = \left(-F_{1i}k_i(\sin k_i x + \sinh k_i x) + F_{2i}k_i(\cos k_i x - \cosh k_i x)\right)\cos \omega_i t \quad \textbf{(9)}$$

The terms $k_i l$ are computed in *Reference 10* and reproduced in *Table 3*.

Table 6.3. Consecutive roots for a beam with one end fixed and one end free [10]

$k_1 l$	$k_2 l$	$k_3 l$	$k_4 l$	$k_5 l$	$k_6 l$
1.875	4.694	7.855	10.996	14.137	17.279

Table 6.4. Experimental Fiber Overhang Lengths—(*l*)

	Broadband Piezo	**Prototype Piezo**
l	11.5 mm	9.0 mm

Data were also fit to an allometric (increasing monotonically with fiber length) deflection equation and compared to beam theory data fits.

$$D = a + bx^c \quad \textbf{(10)}$$

$$\frac{dD}{dx} = cbx^{c-1} \quad \textbf{(11)}$$

C. Initial Fiber Deflection Mode Shape Analysis with a Broadband Piezo Device.

While we wish to characterize the prototype, each prototype requires time to fabricate. Initially, broadband piezoelectric devices, which are commercially available and simple to integrate with optical fibers, were used for SMF characterization. The SMF used optimally propagates light at 1300 nm. The fiber placement on the

broadband piezo and digital images used to analyze fiber deflection are compiled in *Figure 13(a-f).*

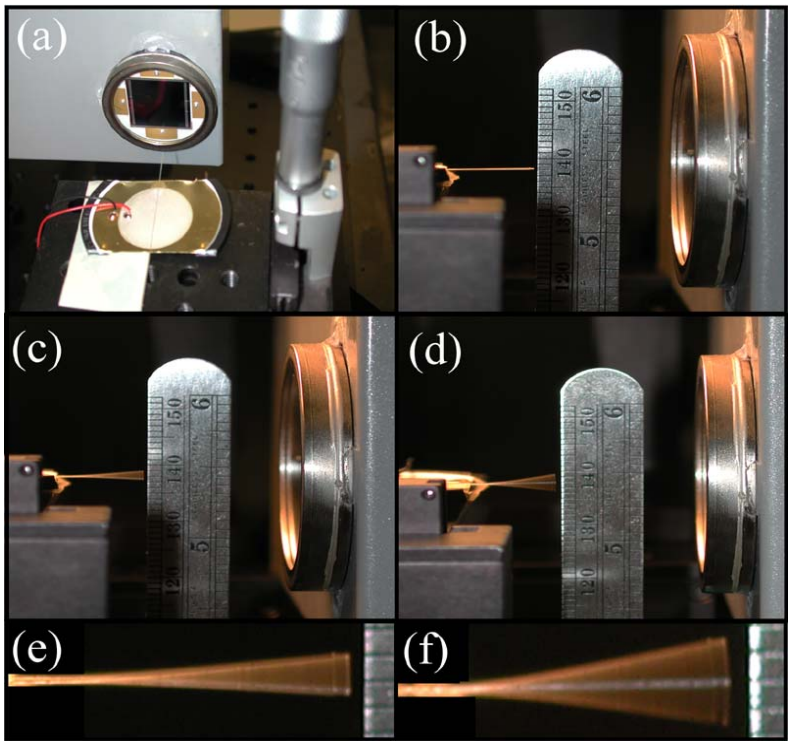

Figure 6.13. Broadband Piezo Fiber Characterization Images. (a) Fiber orientation on broadband piezo element. **(b)** Fiber with 0V supplied. **(c)** Fiber deflection with 20 V_{PP} supplied to piezo at 900 Hz. **(d)** Fiber deflection with 40 V_{PP} supplied to piezo at 900 Hz. **(e)** Fiber image cropped from (c) **(f)** Fiber image cropped from (d).

Images presented in *Figure 13(e,f)* were digitally process to define upper and lower deflection extrema. Edges and data fits are plotted in *Figure 14(a-d).* Observe the ~ 1mm deflection at 20 V and ~2 mm deflection at 40 V supplied to the broadband piezo.

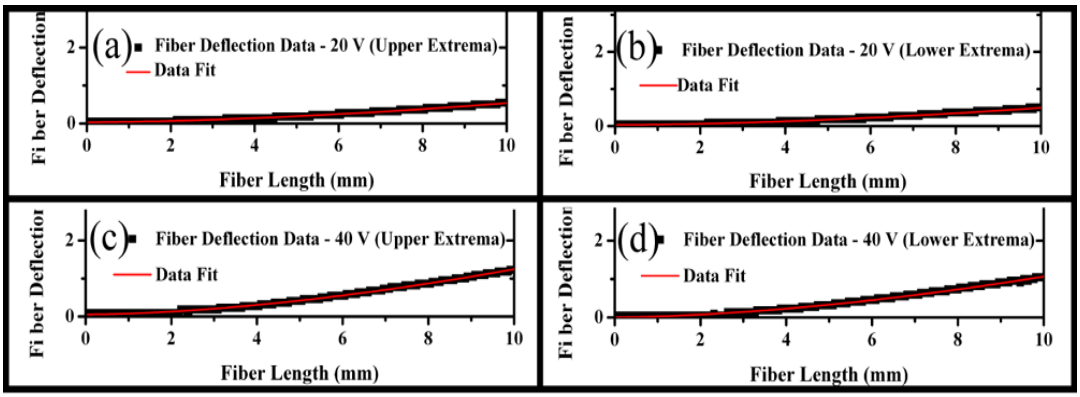

Figure 6.14. Fiber Edge Data and Data Fits (*See Figure 13(e,f)*).

The allometric curve fit data plotted in *Figure 14* are presented in *Table 5*.

Table 6.5. Allometric Data Fit Parameters & Fitting Quality Metrics Extracted from Data in *Figure 14*. $D = a + bx^c$

Curve Fit	Offset (*a*)	Coefficient (*b*)	Power (*c*)
20 V_{pp} Upper Ext.	0.037 ± 0.002	0.010 ± 0.001	1.69 ± 0.02
20 V_{pp} Lower Ext.	0.033 ± 0.002	0.009 ± 0.001	1.71 ± 0.02
40 V_{pp} Upper Ext.	0.054 ± 0.003	0.024 ± 0.001	1.70 ± 0.02
40 V_{pp} Lower Ext.	0.008 ± 0.004	0.021 ± 0.001	1.70 ± 0.02

Curve Fit	R^2	χ^2/DOF
20 V_{pp} Upper Ext.	0.99546	0.00018
20 V_{pp} Lower Ext.	0.99429	0.00020
40 V_{pp} Upper Ext.	0.99713	0.00043
40 V_{pp} Lower Ext.	0.99553	0.00053

The beam theory curve fit data plotted in *Figure 14* are presented in *Table 6*.

Table 6.6. Beam Theory Data Fit Parameters & Fitting Quality Metrics Extracted from Data in *Figure 14*. $D_1 = F_1(\cos k_1 x - \cosh k_1 x) + F_2(\sin k_1 x - \sinh k_1 x)$

Curve Fit	k_1 (fixed)	F_1	F_2
20 V_{pp} Upper Ext.	0.1630	-0.349 ± 0.006	0.276 ± 0.011
20 V_{pp} Lower Ext.	0.1630	-0.316 ± 0.005	0.246 ± 0.010
40 V_{pp} Upper Ext.	0.1630	-0.811 ± 0.011	0.671 ± 0.023
40 V_{pp} Lower Ext.	0.1630	-0.621 ± 0.006	0.433 ± 0.014

Curve Fit	R^2	χ^2/DOF
20 V_{pp} Upper Ext.	0.98461	0.00062
20 V_{pp} Lower Ext.	0.98487	0.00052
40 V_{pp} Upper Ext.	0.99631	0.00043
40 V_{pp} Lower Ext.	0.99142	0.00128

Allometric and beam theory photon emission angles arising from values in *Tables 5 & 6* are presented in *Table 7*.

Table 6.7. Broadband Piezo Photon Emission Angles (*y*-axis).

	$\theta_{Emission}$ **(Allometric)**	$\theta_{Emission}$ **(Beam Theory)**
20 V_{pp} Upper Ext.	5.21° ± 0.87°	4.75° ± 0.58°
20 V_{pp} Lower Ext.	4.98° ± 0.89°	4.42° ± 0.51°
40 V_{pp} Upper Ext.	12.71° ± 1.31°	10.02° ± 1.12°
40 V_{pp} Lower Ext.	11.16° ± 1.22°	10.19° ± 0.65°

D. Fiber Deflection Mode Shape Analysis with Prototype Deflection Data

Confident in the fabrication, digital edge extraction algorithm, and mode shape analysis, the prototype was driven at 790 Hz with voltages supplied at 20 V and 40 V. The images compiled in *Figure 15* demonstrate resonant fiber motion when actuated with *x and y axis* PZT bending elements. *Figure 15(b,c)* images capture the fiber motion with the *y-axis* piezo excited at 790 Hz. *Figure 15(e,f)* images capture the fiber motion with the *x-axis* piezo excited at 790 Hz.

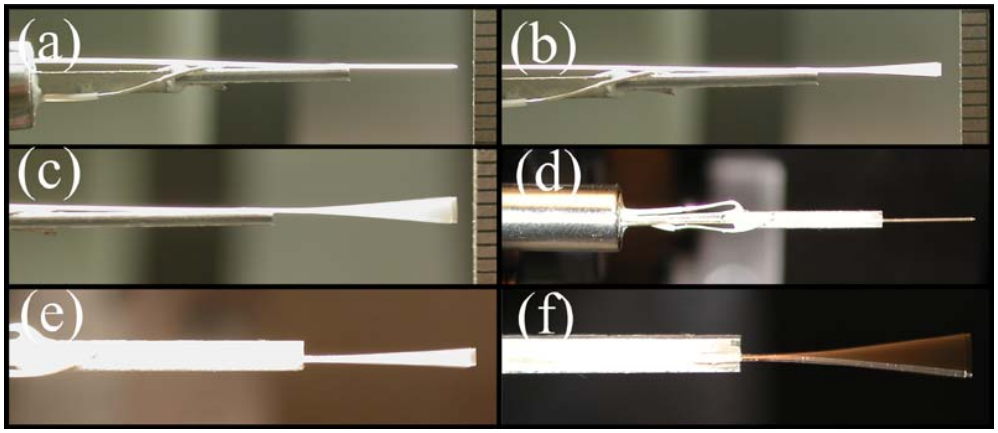

Figure 6.15. Prototype Fiber Characterization (Side-View Pictures). (a) Fiber with 0V supplied to piezo element. **(b)** Fiber with 20 V_{PP} supplied to piezo at 790 Hz (*y*-axis deflection). **(c)** Fiber deflection with 40 V_{PP} supplied to piezo at 790 Hz (*y*-axis deflection). **(d)** Fiber top view with 0V supplied to piezo element. **(e)** Fiber with 20 V_{PP} supplied to piezo at 790 Hz (*x*-axis deflection). **(f)** Fiber deflection with 40 V_{PP} supplied to piezo at 790 Hz (*x*-axis deflection).

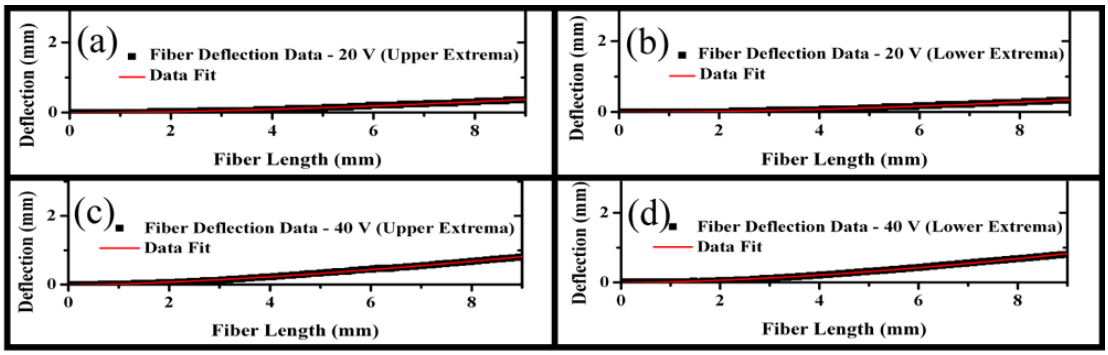

Figure 6.16. Fiber Edge Data and Data Fits (*y-axis deflection data*).

The allometric curve fit data plotted in *Figure 16* are presented in *Table 8*.

Table 6.8. Data Fit Parameters Extracted from Data in *Figure 16*. $D = a + bx^c$

Curve Fit	Offset (*a*)	Coefficient (*b*)	Power (*c*)
20 V_{pp} Upper Ext.	-0.008 ± 0.001	0.011 ± 0.001	1.64 ± 0.02
20 V_{pp} Lower Ext.	-0.010 ± 0.001	0.008 ± 0.001	1.74 ± 0.02
40 V_{pp} Upper Ext.	-0.015 ± 0.001	0.030 ± 0.001	1.51 ± 0.008
40 V_{pp} Lower Ext.	-0.008 ± 0.001	0.023 ± 0.001	1.64 ± 0.010

Curve Fit	R^2	χ^2/DOF
20 V_{pp} Upper Ext.	0.99324	0.00009
20 V_{pp} Lower Ext.	0.99219	0.00009
40 V_{pp} Upper Ext.	0.99829	0.00011
40 V_{pp} Lower Ext.	0.99778	0.00014

The beam theory curve fit data plotted in *Figure 16* are presented in *Table 9*.

Table 6.9. Data Fit Parameters & Fitting Quality Metrics Extracted from Data in *Figure 16*. $D_1 = F_1(\cos k_1 x - \cosh k_1 x) + F_2(\sin k_1 x - \sinh k_1 x)$

Curve Fit	k_1 (fixed)	F_1	F_2
20 V_{pp} Upper Ext.	0.2083	-0.161 ± 0.002	0.095 ± 0.004
20 V_{pp} Lower Ext.	0.2083	-0.125 ± 0.002	0.048 ± 0.004
40 V_{pp} Upper Ext.	0.2083	-0.410 ± 0.002	0.312 ± 0.003
40 V_{pp} Lower Ext.	0.2083	-0.374 ± 0.002	0.242 ± 0.003

Curve Fit	R^2	χ^2/DOF
20 V_{pp} Upper Ext.	0.99343	0.00009
20 V_{pp} Lower Ext.	0.99099	0.00010
40 V_{pp} Upper Ext.	0.99887	0.00007
40 V_{pp} Lower Ext.	0.99882	0.00008

Allometric and beam theory photon emission angles arising from values in *Tables 8 & 9* are presented in *Table 10*.

Table 6.10. Prototype Photon Emission Angles (*y*-axis).

	$\theta_{Emission}$ **(Allometric)**	$\theta_{Emission}$ **(Beam Theory)**
20 V_{pp} Upper Ext.	4.00° ± 0.86°	4.09° ± 0.26°
20 V_{pp} Lower Ext.	3.95° ± 0.86°	4.22° ± 0.26°
40 V_{pp} Upper Ext.	7.87° ± 0.48°	7.55° ± 0.22°
40 V_{pp} Lower Ext.	8.70° ± 0.67°	8.59° ± 0.22°

E. DC Fiber Deflection Results—Digital Image Processing

While resonant motion in the *y-direction* is desired, the slow raster scanning motion in the *x-direction* is non-resonant (1 Hz). To test the *x-direction* piezo bender deflection, the fiber tip in *Figure 17* was imaged at 20 V increments with 4X magnification. Forward and reverse actuation image sets are compiled in *Figure 17*. *Figure 17(a,c)* images the fiber at positive and negative extremes (+80 to -80 V, and -80 to +80 respectively). *Figures 17(b,d)* overlays all incremented images in forward and reverse directions.

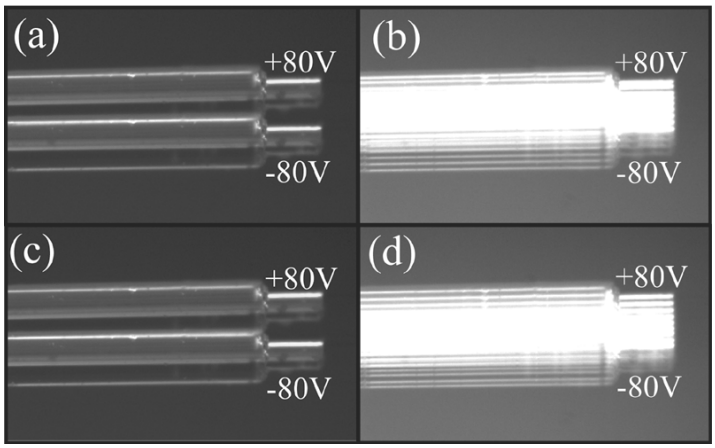

Figure 6.17. DC Fiber Deflection Pictures. Single mode fibers were imaged at 20 V increments from +80V to -80V and -80V to +80V. **(a)** Fiber images at +80 V incremented at 20 V intervals to -80 V. **(b)** Fiber images between +/-80 V added to (a) **(c)** Fiber images at -80 V incremented at 20 V intervals to +80 V. **(d)** Fiber images between -/+80 V added to (c).

The mean fiber tip deflection per 20 V increment (forward and reverse increment progression) and measurement uncertainty are listed in *Table 11*.

Table 6.11. DC Fiber Deflection Data Obtained from Images in *Figure 17.*

	Mean Deflection per 20 Volts	**Measurement Uncertainty**
Forward (+4V to -4V)	28 microns	4 microns
Reverse (-4V to + 4V)	29 microns	4 microns

The pixel size at 4X magnification for the Photometrics Cascade 512b camera used was 4 microns. This value is slightly larger than the statistical standard deviation value computed from the digitally analyzed image set (3.5-3.7 microns). Hence, the measurement uncertainty value reported is 4 microns, as it is reasonable to assume a 1 pixel error in defining the fiber tip.

F. AC Fiber Deflection Results—Digital Image Processing

Driving the prototype *x-axis* PZT bender at 20 V, 100 V, & 200 V at 1 Hz generated the data points plotted in *Figure 18*. The blue lines result from data fit to a sine wave.

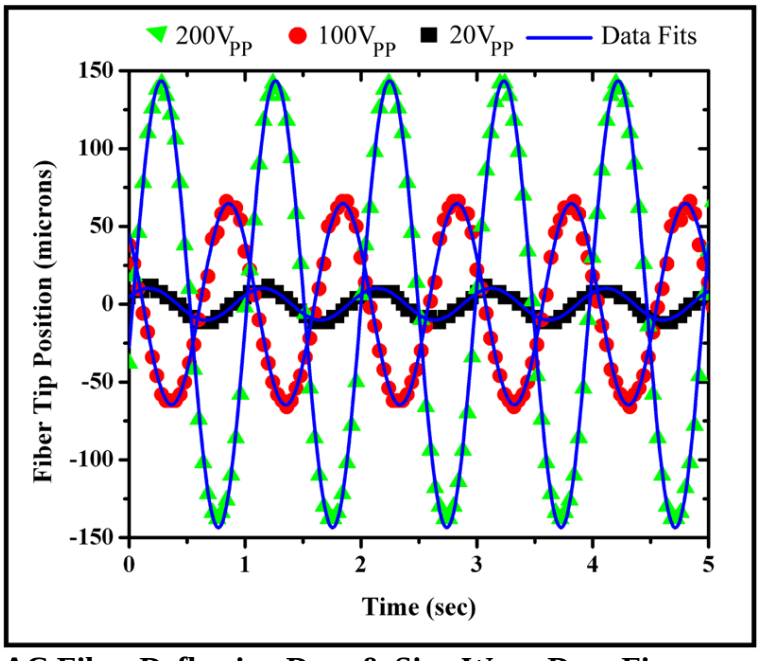

Figure 6.18. AC Fiber Deflection Data & Sine Wave Data Fits.

Table 12 lists the amplitude, period, and measurement uncertainties obtained from data fits.

Table 6.12. AC Fiber Deflection Data Fit Parameters – $D = A\sin(2\pi t / \tau)$

Applied Voltage	Amplitude (A)	Period (τ)
20 V_{PP}	10 ± 4 microns	0.98538 ± 0.00104 s^{-1}
100 V_{PP}	65 ± 4 microns	0.98572 ± 0.00010 s^{-1}
200 V_{PP}	144 ± 4 microns	0.98564 ± 0.00004 s^{-1}

The amplitude data listed in *Table 12* were used to compute the deflection angle and measurement uncertainty for a 35 +/ 0.1 mm prototype length with linear fiber deflection assumed.

Table 6.13. Prototype Photon Emission Angle *vs.* V_{PP} (x-axis).

Applied Voltage	$\theta_{Emission}$
20 V_{PP}	0.032° ± 0.007°
100 V_{PP}	0.212° ± 0.007°
200 V_{PP}	0.472° ± 0.007°

Data from *Table 13* indicate the prototype must be extended from the current length of 35.2 mm to 60.7 mm to achieve a 500 micron deflection at the fiber tip or supplied a higher voltage.

G. Resonant Fiber Frequency Measurement with Position Sensitive Detector (PSD)

Measuring small SMF oscillations requires an optical table and optical positioning/alignment components. The PSD fiber measurement layout is pictured in *Figure 19.*

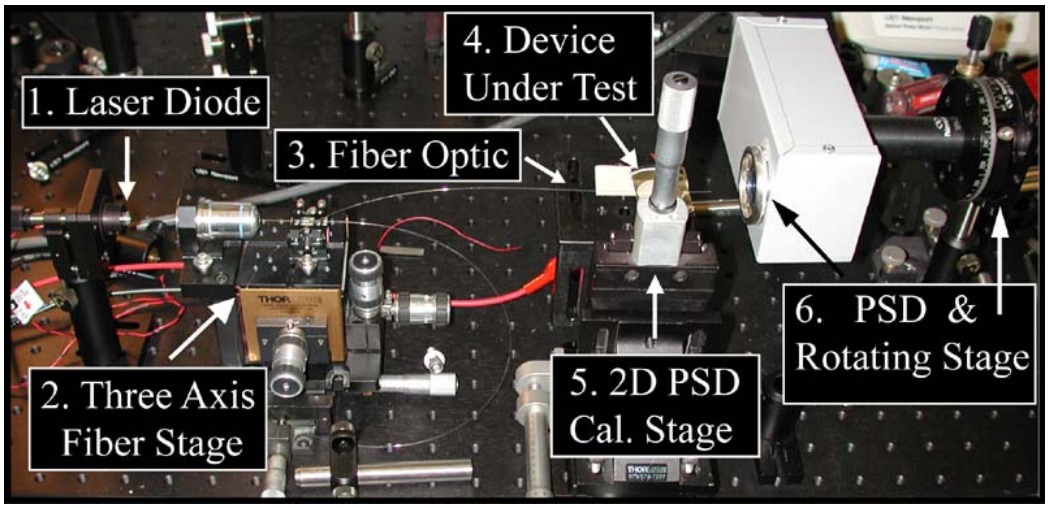

Figure 6.19. Fiber Characterization Layout for Analysis with PSD.

With the optical system pictured in *Figure 19*, magnitude *vs.* frequency data were captured. Data obtained with the PSD are compiled in *Figures 20 & 21*. The broadband piezo actuated fiber closely follows the input drive frequency at 900 Hz. As the input power is increased, the magnitude at 900 Hz (and higher harmonics) increases. The fiber was driven predominately in the *y-direction* as demonstrated when comparing *Figure 20(a,c,e)* to *Figure 20(b,d,f)*. The *y-axis* deflection magnitude was found to be ~25 fold higher in the *y-direction* when compared to the *x-direction* data. *Figures 20(a,b,c,d)* are plotted on a logarithmic scale, while *Figures 20(e,f)* are plotted on a linear scale.

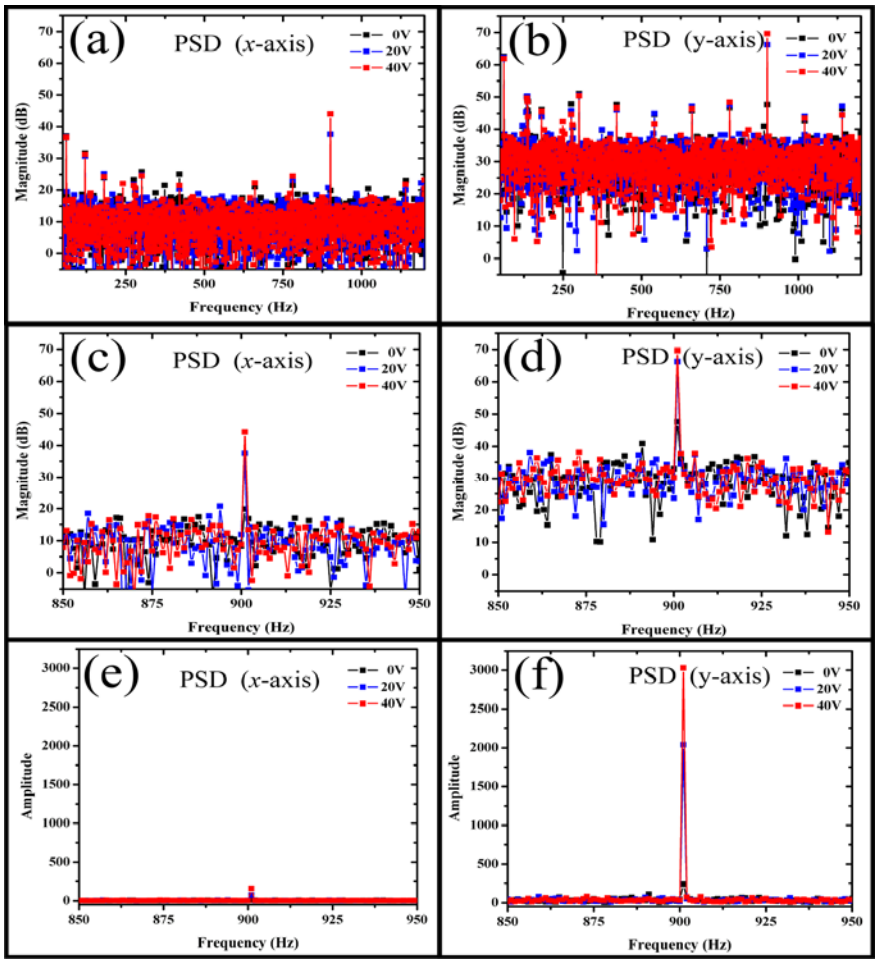

Figure 6.20. AC Fiber Deflection FFT Data. (a) PSD *x-axis* frequency response (dB *vs.* frequency). **(b)** PSD *y-axis* frequency response (dB *vs.* frequency). **(c)** PSD *x-axis* frequency response near 900 Hz input signal (dB *vs.* frequency). **(d)** PSD *y-axis* frequency response near 900 Hz input signal (dB *vs.* frequency). **(e)** PSD *x-axis* frequency response near 900 Hz input signal (amplitude *vs.* frequency). **(f)** PSD *y-axis* frequency response near 900 Hz input signal (amplitude *vs.* frequency).

The magnitude *vs.* frequency data also quantify the contributions from higher order modes. *Figure 21* plots frequency response data from 900 Hz to 5500 Hz. Peaks at 1800, 2700, & 3600 Hz resulting from the piezo drive and a second order fiber mode contribution at 4500 Hz are notable. Data suggest such contributions are small, though non-negligible.

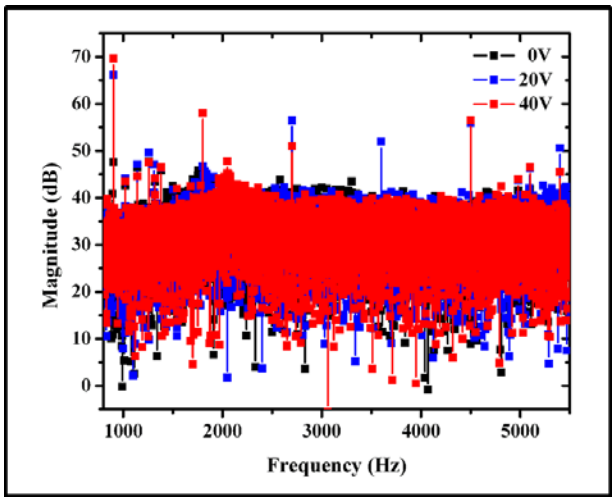

Figure 6.21. AC Fiber Deflection FFT Data (Frequency range from fundamental to second order resonant mode at ~4500Hz). Note piezo and fiber tip overhang harmonics at ~1800, 2700, 3600, & 4500 Hz.

VI. CONCLUSIONS

This work outlines the design, fabrication, characterization, and analysis necessary to operate and understand a two-dimensional raster scanning system. Data obtained must be internalized and integrated into the broader system understanding to assess clinical feasibility. The fast scanning prototype deflection values are acceptable, while the slow scan deflection amplitude must be increased. Alternative device geometries will be pursued in future iterations.

VII. NOTES REGARDING FUTURE DIRECTION

A. Prototype Fabrication Improvements

Prototype packaging can be improved. Conveniently, flexible electrodes patterned on robust Kapton material have been developed for complex packaging applications. The material and electrodes are pictured in *Figure 22*. Incorporating such high aspect ratio materials into the current prototype would reduce emitted photon absorption by wiring material.

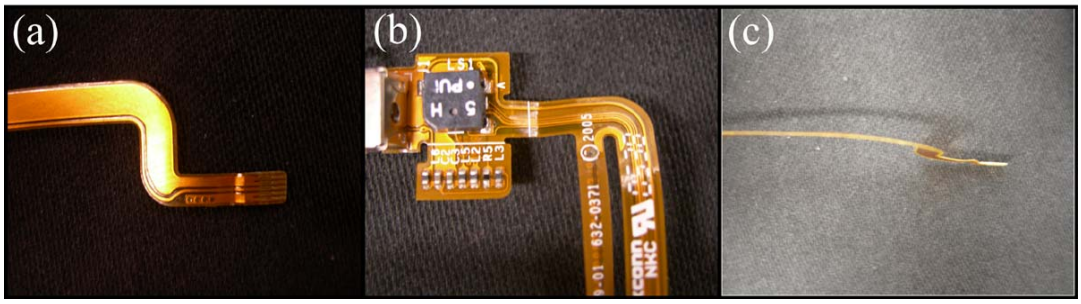

Figure 6.22. Flexible Electronics. Future designs will integrate Kapton patterned with electrodes to reduce scanner cross-sectional area.

Similarly, PZT sheet dicing can be automated with existing semi-conductor processing technology. *Figure 23* shows a state-of-the-art dicing saw used by chip manufacturers to carefully and repeatably dice high value silicon devices.

Figure 6.23. Semiconductor Wafer Dicing Saw (Kulicke & Soffa).

B. Hydraulic Zoom

The design discussed and characterized neglects fiber motion in the *z-direction* (coaxial to the steel housing). Future designs will potentially incorporate a hydraulic zoom capability. Alternative methods include a servo motor, which may act directly on the fiber optic system.

VIII. POTENTIAL OPPORTUNITIES FOR DESIGN DIFFERENTIATION

A. Integrated Strain Gauges for Closed Loop Operation

Future designs may include integrated strain gauges to monitor piezo deflection carefully and operate electromechanical components in a closed-loop control system.

B. Sol Gel Derived PZT Film Fiber Coating

Reducing the bender cross-sectional area is an area targeted for improvement, as this would increase photon collection (i.e. reduce photon absorption by scanner materials). A micron scale sol-gel derived PZT fiber coating is detailed in *Reference 11*.

C. Kapton—PZT Laminates

NASA has developed Kapton encapsulated PZT fibers for actuation purposes. Producing fully encapsulated fibers in Kapton (a *space polymer suitable for autoclave cycling*) would yield a robust, fully packaged actuator with a small cross-sectional area.

ACKNOWLEDGMENT

This work has been supported with funding from the National Institutes of Health.

REFERENCES

[1] W.R. Zipfel, R.M. Williams, & W.W. Webb, "Nonlinear Magic: multiphoton microscopy in the biosciences", *Nature Biotechnology*, vol. 21, no. 11, November 2003, 1369-1377.

[2] F. Helmchen, M.S. Fee, D.W. Tank, & W. Denk, "A Miniature Head-Mounted Two-Photon Microcsope: High-Resolution Brain Imaging in Freely Moving Animals", *Neuron*, vol. 31, September 27, 2001, 903-912.

[3] B.A. Flusberg *et al.*, "Fiber Optic Two-Photon Fluorescence Microendoscopy: Towards Brain Imaging in Freely Moving Mice", *Conference on Lasers & Electro-Optics 2005*, 2233-2235.

[4] B.A. Flusberg *et al.*, "*In vivo* imaging using a portable 3.9 gram two-photon fluorescence microendoscope", *Optics Letters*, vol. 30, no. 17, September 1, 2005, 2272-2274.

[5] B.A. Flusberg *et al.*, "Fiber-optic fluorescence imaging", *Nature Methods*, vol. 2, no. 12, December 2005, 941-950.

[6] D.A. Roberts & R.A. Syms, "1D and 2D laser line scan generation using a fibre optic resonant scanner", *Micro-Opto-Electro-Mechanical Systems—Proc. SPIE*, vol. 4075 (2000), 62-73.

[7] M.T. Myaing, D.J. MacDonald, & X. Li, "Fiber-optic scanning two-photon fluorescence endoscope", *Optics Letters*, vol. 31, no. 8, April 15, 2006, 1076-1078.

[8] W.C. Warger II & C.A. DiMarzio, "Dual-Wedge Scanning Confocal Reflectance Microscope", *Optics Letters*, vol. 32, no. 15, August 2007, 2140-2142.

[9] J. Sawinski & W. Denk, "Miniature random-access fiber scanner for *in vivo* multiphoton imaging", *J. Applied Physics*, 102, 034701, 2007.

[10] W. Weaver, Jr., S.P. Timoshenko, & D.H. Young, *Vibration Problems in Engineering*, Fifth Ed., John Wiley & Sons, Inc., 1990.

[11] D.A. Barrow, R. Noteboom, & M. Sayer, “Design & Fabrication of Macroscopic Piezoelectric Actuators Based on Thick PZT Films”, *Integrated Ferroelectrics*, vol. 8, 1995, 1-11.

CHAPTER SEVEN

Conclusions & Future Device Utility (Speculative)

Piezoelectric devices are used in applications ranging from satellites to nanoscale positioners. In this work we sought to extend utility to biological sample preparation, microscale mixing, and immunoassays.

Microfluidic mixing is an area where devices have clear utility. Numerous authors have discussed this application. We can envision improved mass transport and electrically controlled fluid flow requiring no additional reagent addition proving useful in biological screening and immunoassays. Assays would screen for proteins, affinity probes, nano/microparticles, or cells, based on affinity. Performing such operations with pressure driven flow or electrokinetic flow is impractical in our view.

Devices are clearly useful in rapidly removing weakly bound material. Results demonstrating rapid nonspecific binding removal are encouraging. By combining good chemistry, biochemical probe engineering, and effective washing, assays can be optimized to yield higher signal-to-background ratios. Higher signal-to-background ratios can be obtained in a shorter time with ultrasonic device incorporation.

When considering protein desorption from an interface, we sought to measure the relative contributions from mass transport alteration, thermal fluctuations, and acoustically induced conformational changes accelerating protein desorption. Not for lack of effort, we found this challenge difficult in the presented optical interrogation set-up. Single molecule studies will prove far superior in extracting binding and release information. Perhaps our notes will streamline this process, or be integrated with single molecule devices to rapidly transport antigen to sparsely populated

receptor surfaces in diffusion limited situations. Because binding events would be rare in low-concentrations sample solutions devices may have utility.

We suspect device utility may not arise from a single capability (e.g. mixing or accelerated protein desorption). Rather utility may exist where a single device can rapidly mix, separate, and sense in a single fluid volume. Combining fast sample preparation, separation, and analysis without complex, high surface area, microstructures, is desirable in my view. We anticipate and respect the significant engineering and manufacturing energy necessary to bring this technology into competitive markets.

The dimensional scanner produced meets size constraints, however, the length must be extended or voltage increased to achieve the desired 0.5 mm scan range. We are currently fabricating a longer slow access piezo and shortening the fast scan piezo to improve slow scan deformation amplitude. The suggested improvements listed within chapter six will further reduce the prototype cross-sectional area and improve packaging. The actuator and lens design demands are significant, requiring careful consideration to package properly.

Given the limited slow-scan fiber motion distance, exploring alternative geometries is noted. Aligning multiple fibers separated by cladding and either simultaneously, or incrementally exciting multiple single mode fibers may present a viable alternative meeting instrument design demands.